

# Carbon content and transport investigations on Wendelstein 7-X with Charge Exchange Recombination Spectroscopy

vorgelegt von

M.Sc.

Lilla Vanó

ORCID: 0000-0001-7883-6471

von der Fakultät II - Mathematik und Naturwissenschaften  
der Technischen Universität Berlin  
zur Erlangung des akademischen Grades

Doktor der Naturwissenschaften

-Dr. rer. nat.-

genehmigte Dissertation

Promotionsausschuss:

Vorsitzender: Prof. Dr. Holger Stark

Gutachter: Prof. Dr. Robert Wolf

Gutachter: Prof. Dr. Dieter Breitschwerdt

Gutachter: Dr. Sándor Zoletnik

Tag der wissenschaftlichen Aussprache: 17. Juni 2022

Berlin, 2022



You are not alone.

---

Raana Raas (Etelka G6rgey),  
Csodaid6k



# Abstract

In experimental fusion devices, such as the optimised stellarator Wendelstein 7-X (W7-X), the main plasma ions are isotopes of hydrogen, besides which several impurity species are present. Too high levels of impurities are unfavourable in the plasma core, as they dilute the plasma or cause radiation energy losses, which negatively affect plasma performance. In the plasma edge, in front of the plasma facing elements, impurity radiation is favourable due to the fact that it increases wall protection by distributing the heat load from the plasma more evenly over the plasma facing elements. Impurity control is therefore essential for long steady-state high performance plasmas on the way towards a future fusion reactor.

To be able to control impurities and find ways to keep them out of the plasma core, impurity transport and the effect of different plasma parameters on it needs to be understood. Collisional transport in toroidal magnetic devices like W7-X is referred to as neoclassical transport. Additional effects can contribute to the particle transport, such as turbulence, which are collectively referred to as anomalous transport.

In this work, the impurity transport is studied using the transport modeling code pySTRAHL to derive transport coefficients from the experimental profiles of the impurity density. These profiles are absolute density profiles of fully ionised carbon that are obtained from Charge Exchange Recombination Spectroscopy measurements at W7-X. As many wall elements of the device are made of carbon, from which particles can enter the plasma due to erosion, carbon is the main impurity in W7-X. The carbon density is derived using the intensity of the carbon charge exchange signal and the intensity of the neutral beam emission signal.

The transport analysis is done for two types of plasmas: ones heated by Electron Cyclotron Resonance Heating (ECRH) and plasmas heated by Neutral Beam Injection (NBI). In ECRH dominated discharges, turbulence dominated transport is observed, evidenced by high anomalous diffusion, which results in flat carbon density profiles. In pure NBI heated plasma

phases, carbon accumulates in the plasma core, corresponding to strongly reduced diffusion inside half radius of the plasma cross section. The transport modelling shows profiles of accumulating carbon density, which match the experimental profiles only if the core diffusion is reduced to the order of neoclassical levels. Hence, the turbulence is observed to be reduced in the core of purely NBI heated plasmas. Outside half radius, anomalous diffusion is needed to match the experimental carbon density in this plasma region. With the addition of a small level of ECRH power, the carbon density profile in the core becomes flat, indicating a return to turbulence dominated conditions. However, at half radius the strong gradient and neoclassical dominated region remains.

Additionally, the absolute carbon density profiles are used to estimate the achieved triple product in high performance plasma phases. The triple product is suitable to compare the performance of different fusion devices. The highest triple product observed in a stellarator was achieved at W7-X, and the carbon density profiles are used to verify this reported value by taking into account the effect of impurity content on the triple product.

To support the transport analysis of absolute density profiles of fully ionised carbon, the line integrated emission of hydrogen-like carbon in the plasma is also examined. This gives further insight about the underlying processes between the carbon ions and the plasma particles.

# Zusammenfassung

In experimentellen Fusionsanlagen wie dem optimierten Stellarator Wendelstein 7-X (W7-X) sind die wichtigsten Plasma-Ionen Wasserstoff-Isotope, daneben gibt es mehrere Verunreinigungsarten. Ein zu hoher Gehalt an Verunreinigungen ist im Plasmakern ungünstig, da sie das Plasma verdünnen oder Strahlungsenergieverluste verursachen, die sich negativ auf die Plasmaleistung auswirken. Am Plasmarand, vor den plasmazugewandten Elementen, ist die Abstrahlung von Verunreinigungen günstig, da sie den Wandschutz erhöht, indem sie die Wärmebelastung durch das Plasma gleichmäßiger auf die plasmazugewandten Elemente verteilt. Die Kontrolle von Verunreinigungen ist daher für lange stationäre Hochleistungsplasmen auf dem Weg zu einem künftigen Fusionsreaktor unerlässlich.

Um Verunreinigungen kontrollieren zu können und Wege zu finden, sie aus dem Plasmakern herauszuhalten, müssen der Transport von Verunreinigungen und die Auswirkungen verschiedener Plasmaparameter auf diesen Transport verstanden werden. Der Kollisionstransport in toroidalen magnetischen Anlagen wie dem W7-X wird als neoklassischer Transport bezeichnet. Zusätzliche Effekte, wie z. B. Turbulenzen können zum Teilchentransport beitragen, ihr Beitrag wird in der Regel als anomaler Transport bezeichnet.

In dieser Arbeit wird der Verunreinigungstransport mit Hilfe des Transportmodellierungscodes pySTRAHL untersucht, um Transportkoeffizienten aus den experimentellen Profilen der Verunreinigungsdichte abzuleiten. Bei diesen Profilen handelt es sich um absolute Dichteprofile von vollständig ionisiertem Kohlenstoff, die aus Messungen der Ladungsaustausch-Rekombinations-Spektroskopie bei W7-X gewonnen wurden. Da viele Wandelemente der Anlage aus Kohlenstoff bestehen, aus dem durch Erosion Partikel in das Plasma gelangen können, ist Kohlenstoff die Hauptverunreinigung. Die Kohlenstoffdichte wird anhand der Intensität des Kohlenstoff-Ladungsaustauschsignals und der Intensität des Neutralstrahl-Emissionssignals ermittelt.

Die Transportanalyse wird für zwei Arten von Plasmen durchgeführt: Plas-

men, die durch Elektronen-Zyklotron-Resonanzheizung (ECRH) geheizt werden, und Plasmen, die durch Neutralstrahl-Injektion (NBI) geheizt werden. In ECRH-beheizten Entladungen wird ein turbulenzdominierter Transport beobachtet, der sich durch eine hohe anomale Diffusion auszeichnet, was zu flachen Kohlenstoffdichteprofilen führt. In reinen NBI-beheizten Plasmafasen sammelt sich der Kohlenstoff im Plasmakern an, was einer stark reduzierten Diffusion innerhalb des halben Radius des Plasmaquerschnitts entspricht. Die Transportmodellierung zeigt Profile der akkumulierenden Kohlenstoffdichte, die nur dann mit den experimentellen Profilen übereinstimmen, wenn die Kerndiffusion auf die Größenordnung der neoklassischen Werte reduziert wird. Folglich wird beobachtet, dass die Turbulenz im Kern von rein NBI-beheizten Plasmen reduziert ist. Außerhalb des halben Radius ist anomale Diffusion erforderlich, um die experimentelle Kohlenstoffdichte in dieser Plasmaregion zu erreichen. Es wird also beobachtet, dass die Turbulenz im Kern von rein NBI-beheizten Plasmen reduziert ist. Um mit den experimentellen Kohlenstoffdichteprofilen übereinzustimmen, ist eine endliche anomale Diffusion außerhalb des halben Radius erforderlich. Durch solche Damit die experimentellen Kohlenstoffdichteprofile übereinstimmen, ist eine anomale Diffusion außerhalb des halben Radius erforderlich. Bei Hinzufügung einer geringen ECRH-Leistung wird das Kohlenstoffdichteprofil im Kern flach, was auf eine Rückkehr zu turbulenzdominierten Bedingungen hinweist. Bei halbem Radius bleibt jedoch der starke Gradient und die neoklassisch dominierte Region bestehen. Bei halbem Radius bleibt jedoch der starke Gradient und die neoklassisch dominierte Region bestehen.

Darüber hinaus werden die absoluten Kohlenstoffdichteprofile verwendet, um das erzielte Dreifachprodukt in Hochleistungsplasmaphasen zu schätzen. Das Dreifachprodukt eignet sich zum Vergleich der Leistung verschiedener Fusionsanlagen. Das höchste Dreifachprodukt, das in einem Stellarator beobachtet wurde, wurde bei W7-X erreicht, und die Kohlenstoffdichteprofile werden verwendet, um diesen gemeldeten Wert zu überprüfen, indem die Auswirkungen des Verunreinigungsgehalts auf das Dreifachprodukt berücksichtigt werden.

Zur Unterstützung der Transportanalyse der absoluten Dichteprofile von vollständig ionisiertem Kohlenstoff wird auch die linienintegrierte Emission von wasserstoffähnlichem Kohlenstoff im Plasma untersucht. Dies gibt weitere Einblicke in die zugrundeliegenden Prozesse zwischen den Kohlenstoff-Ionen und den Plasmateilchen.

# Contents

<b>Abstract</b>	<b>5</b>
<b>Zusammenfassung</b>	<b>7</b>
<b>1. Introduction</b>	<b>11</b>
1.1. Basics of fusion research . . . . .	11
1.2. Wendelstein 7-X . . . . .	12
1.2.1. General structure and properties . . . . .	12
1.2.2. Magnetic structure . . . . .	16
1.2.3. Heating methods . . . . .	17
1.2.4. Additional components and diagnostic systems . . .	21
1.3. Transport in plasmas . . . . .	23
1.4. Impurities in fusion plasmas . . . . .	27
1.5. Impurity transport modelling . . . . .	29
<b>2. Passive Spectroscopy</b>	<b>33</b>
2.1. Methods . . . . .	33
2.1.1. Observation system at W7-X . . . . .	33
2.1.2. Processing the measured spectra . . . . .	35
2.1.3. Forward modelling to obtain carbon emission intensity	40
2.2. Investigation of carbon content in the outer plasma . . . . .	46
2.3. Estimation of the neutral density inside the separatrix . . .	54
<b>3. Active Spectroscopy</b>	<b>59</b>
3.1. Methods . . . . .	60
3.1.1. Observation system at W7-X . . . . .	60
3.1.2. Processing the measured spectra . . . . .	66
3.1.3. Calculating carbon density profiles with cross calibration . . . . .	71

3.1.4.	Comparison with carbon density profiles with a different approach . . . . .	81
3.1.5.	Contribution of the neutral beam halo to the measured carbon intensity . . . . .	83
3.2.	Investigation of carbon transport in the plasma core . . . . .	84
3.2.1.	Carbon transport in ECRH dominated plasma scenarios	85
3.2.2.	Dependencies of carbon density in ECRH dominated plasma scenarios . . . . .	88
3.2.3.	Carbon density behaviour in NBI heated plasma scenarios . . . . .	92
3.2.4.	Carbon transport evolution in NBI heated plasma scenarios . . . . .	97
3.2.5.	Carbon density in plasmas with combined ECRH and NBI heating . . . . .	110
3.2.6.	Carbon density in pellet induced high performance plasma scenarios . . . . .	114
<b>4.</b>	<b>Conclusions</b>	<b>121</b>
<b>5.</b>	<b>Outlook</b>	<b>125</b>
<b>A.</b>	<b>Acknowledgements</b>	<b>127</b>
	<b>Statutory declaration</b>	<b>129</b>
	<b>List of Figures</b>	<b>131</b>
	<b>List of Tables</b>	<b>141</b>
	<b>Bibliography</b>	<b>143</b>

# Chapter 1.

## Introduction

### 1.1. Basics of fusion research

Nuclear fusion has been researched as an energy producing option more reliable and environmentally friendly than the current energy producing methods. During the fusion of light nuclei, excess energy is released. To overcome the Coulomb barrier between two nuclei for the fusion reaction to happen, high energy particles are needed. This can be accomplished by random collisions in a high temperature environment. The threshold energy is the lowest in the case of deuterium-tritium fusion, making it the easiest to use for energy production on Earth and the current goal of fusion research. This fusion reaction typically needs  $\approx 10$  keV. In most current experimental fusion machines, deuterium or simply hydrogen is used to investigate the plasma and machine conditions that are suitable for future reactors, as the production and safe handling of tritium is more complicated than the other two commonly used hydrogen isotopes.

At the temperatures needed, the hydrogen isotopes are in the plasma state because as the temperature rises, the electrons gain enough energy to be freed from the atom, leading to an ion and an electron population. Thus, in case of the investigated hydrogen plasmas, the two main populations are fully ionised hydrogen nuclei, the so-called main ions and the electrons, forming a quasi neutral composition.

Assuming a homogenous steady-state plasma with 50 – 50% deuterium and tritium composition, the criterion for self-sustaining fusion operation [1] describes that the so-called triple product needs to be above a certain level. This is the Lawson criterion [2] [3], shown in Equation 1.1.

$$n_i \tau_E T_i \approx 10^{22} \text{ m}^{-3} \text{ keV s} \quad (1.1)$$

$n_i$  is the ion density,  $T_i$  is the ion temperature and  $\tau_E$  is the energy confinement time. The exact threshold level depends on the profile shape of  $n_i$  and  $T_i$ , while it stays in the same order of magnitude. The energy confinement time characterises the energy losses of the system, it describes how fast (in how much time) the plasma loses its thermal energy [4]. It is calculated according to the following:

$$\tau_E = \frac{W_{total}}{P_{losses}} = \frac{W_{dia}}{P_{heating}} \quad (1.2)$$

$W_{total}$  is the total internal stored energy of the plasma that is equal to the measured diamagnetic energy,  $W_{dia}$ , if the energy distribution of the ions is isotropic.  $W_{dia}$  is calculated from the changes in the toroidal magnetic flux measured by magnetic coils [5].  $P_{losses}$  is the power loss of the plasma that is equal to the power put into the plasma in a steady-state scenario. The input power is measured by the heating power,  $P_{heating}$ . The Lawson criterion describes that the plasma needs to be sufficiently confined from its environment at a sufficient temperature with a sufficient density to provide self-sustaining energy production. This is generally true for any fusion device, therefore the triple product is commonly used to compare different fusion experiments, even if they have significantly different properties. Empirical scaling laws have been established in the parameter space where the different devices are compared against each other [6] [7]. These scaling laws can be extrapolated towards reactor-like conditions, providing a guideline for the development of fusion device.

## 1.2. Wendelstein 7-X

### 1.2.1. General structure and properties

To satisfy the criterion of the triple product, one of the main concepts is magnetic confinement of low density plasmas ( $\approx 10^{20} \text{ m}^{-3}$ ) for a sufficiently long time. The basis of the concept is that the charged particles of the plasma follow the magnetic field lines by following circular gyro orbits around the lines, making it possible to shape the plasma by the magnetic field [8]. A

linear configuration is not suitable for energy production as there are too big energy losses at the two ends of a linear device. Instead, the plasma is shaped into a torus with magnetic coils used for confining its charged particles. However, in a toroidal magnetic field scenario, the combination of forces created by the inhomogeneous magnetic and electric field moves the plasma particles towards the wall of the machine. This can be eliminated by helically twisting the magnetic field lines. There are two methods to do this that result in the two types of current experimental magnetic fusion devices, tokamaks [9] and stellarators [10]. The created magnetic field results in embedded closed magnetic surfaces which are called flux surfaces. The plasma pressure and many other quantities such as temperatures and densities are either exactly or approximately constant on a given flux surface, due to fast transport along the field lines.

In a stellarator, the magnetic field is twisted by a series of external coils that result in a ribbon-like non-symmetric plasma shape. To do this, the magnetic coils have to be specially shaped. Wendelstein 7-X (W7-X) is an optimised stellarator located in Greifswald, Germany [11] [12]. A description of its structure and components will be given in the following.

W7-X is currently the largest stellarator in the world. Its magnetic structure was optimised to achieve reduced energy transport due to drifts of the particle orbits (neoclassical transport) and good fast particle confinement, as well as minimisation of self-generated plasma currents [14] [15] [16]. Its general structure can be seen in Figure 1.1. The plasma is confined in a vacuum vessel that is surrounded by superconducting magnetic coils. The whole structure is housed within a cryostat that serves as a temperature seal to keep the superconductors at sufficiently low temperatures.

W7-X consists of 5 identical magnetic field modules, each module is symmetric to its central cross section. To observe the plasma, a series of diagnostic ports is installed, these are displayed in Figure 1.1. Each port has their opening in the cryostat and an immersion tube that leads to the vacuum vessel.

The inner wall of the vacuum vessel is covered with carbon tiles. This is the area that the exhaust of the plasma can come into contact with, and can sputter carbon particles in towards the plasma. Carbon is a material that can withstand the high heat loads found in the exhaust of the plasma wall, minimising sputtering. Additionally, it has a relatively low  $Z$ , which means lower radiation losses in case the particle penetrates into the plasma core,

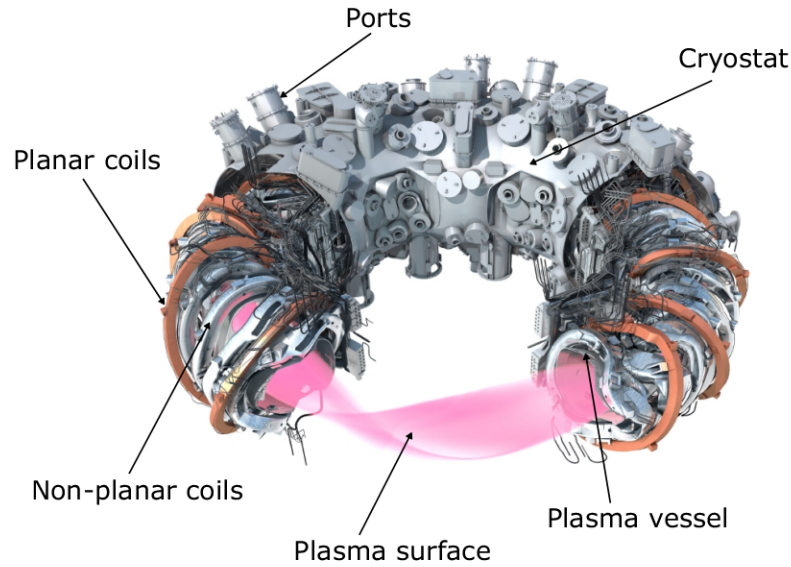


**Figure 1.1.:** Outline of the Wendelstein 7-X stellarator. The plasma (pink) located in a vacuum vessel is confined by the non-planar coils (grey). The magnetic field is adjusted by the planar coils (orange) to for example modify the radial position of the plasma. The external superconducting coils are surrounded by the cryostat (grey). Source: [13]

as low- $Z$  are fully ionised and therefore do not radiate at typical plasma core temperatures. The magnetic field, that shapes the plasma, is separated into a region of closed and open field lines. The region of closed field lines defines the confined plasma region. The region of open field lines is called the Scrape-Off Layer (SOL) where the electron density and temperature values exponentially drop. The boundary between the closed and the open field lines is called the separatrix, or the Last Closed Flux Surface (LCFS). The plasma particles that diffuse out of the confined region into the SOL are transported towards the wall along the open field lines. To minimize the penetration of impurities from the wall in towards the confined plasma, a divertor system is installed [17]. The divertor, made of specifically designed carbon tiles, is located away from the confined region, with all the open magnetic field lines guided towards them. Thus, most of the heat and particle flux that moves out of the confined plasma hits the divertor that is designed to withstand a much higher heat load than the other wall surfaces. The



**Figure 1.2.:** The divertor plates (black) arranged in five bundles around the confined plasma (orange). The special carbon tiles of the divertor system are used to safely take up the heat and particle load coming from the plasma. Source: [18]

arrangement of the divertor system around the plasma is shown in Figure 1.2.

The first W7-X measurement campaign OP1.1 was run with no divertor, with the plasma edge defined simply by a set of carbon tiles on the inner wall called a limiter. The second campaign, OP1.2 was aiming at testing the machine capabilities with the installed non-cooled carbon divertor [19] [20]. The first carbon divertor campaign, OP1.2a was conducted in autumn 2017. There was no Neutral Beam Injection (NBI) heating (see Section 1.2.3) available during this campaign. The second, referred to as OP1.2b was conducted in summer and autumn 2018. The NBI heating was available for the first time at W7-X during this campaign, making the Charge Exchange Recombination Spectroscopy (CXRS) diagnostic available (see Chapter 3). One plasma experiment is referred to as discharge. Every discharge is named with the date it was conducted on and a number referring to the experiment on a given day.

### 1.2.2. Magnetic structure

The magnetic field of W7-X is created by a set of non-planar coils (grey in Figure 1.1) that generate the baseline magnetic field, and by a set of planar coils (orange in Figure 1.1) that generate additional magnetic fields to flexibly modify the given magnetic configuration. This provides a possibility of several configurations [21] to explore the confinement and stability of different regimes [22]. The most optimised configuration is called the standard configuration.

The magnetic field of W7-X is constructed in a way that there is a chain of magnetic islands in the SOL region [17]. An example cross section of the plasma can be seen in Figure 1.3, showing flux surfaces of the standard magnetic configuration, as well as the magnetic islands around the confined region. The field lines consisting the islands are designed to be cut by the divertor. The SOL acts as a barrier between the divertor and the confined plasma, and the magnetic island structure is an effective way of withholding impurities reaching the confined region. It maximises the friction forces between the impurities and the main ions that pushes the impurities back towards the divertor, and minimises the thermal forces that push the impurities towards the confined region via the ion temperature gradient [23].

The 3D geometry of W7-X is typically described by two different coordinate systems, cylindrical and magnetic flux. The cylindrical coordinates are radial ( $R$ ), vertical ( $Z$ ) and toroidal ( $\phi$ ). The radial coordinate  $R$  is the major radius of the stellarator, measured from the middle of the torus. The vertical coordinate ( $Z$ ) is perpendicular to the major radius. The magnetic flux coordinates are radial ( $r_{Eff}$ ), toroidal ( $\phi$ ) and poloidal ( $\theta$ ). This coordinate system depends on the flux surfaces, unlike the cylindrical. The effective minor radius,  $r_{Eff}$  is calculated from the minor radius ( $r$ ) which measured from the middle of the plasma cross section, called the magnetic axis.  $r_{Eff}$  is needed because the cross section and therefore its radius changes with toroidal angle. it is defined so that the effective radius of any given point is the average radius of the flux surface that goes through that point, resulting in the flux surfaces to be labelled with  $r_{Eff}$ .  $\rho$  is a radial coordinate that is defined as 0 at the magnetic axis, and 1 at the LCFS, as an alternative average radius. Considering the axis of the major radius, the plasma region on the outer side of the magnetic axis is called the Low Field Side (LFS),

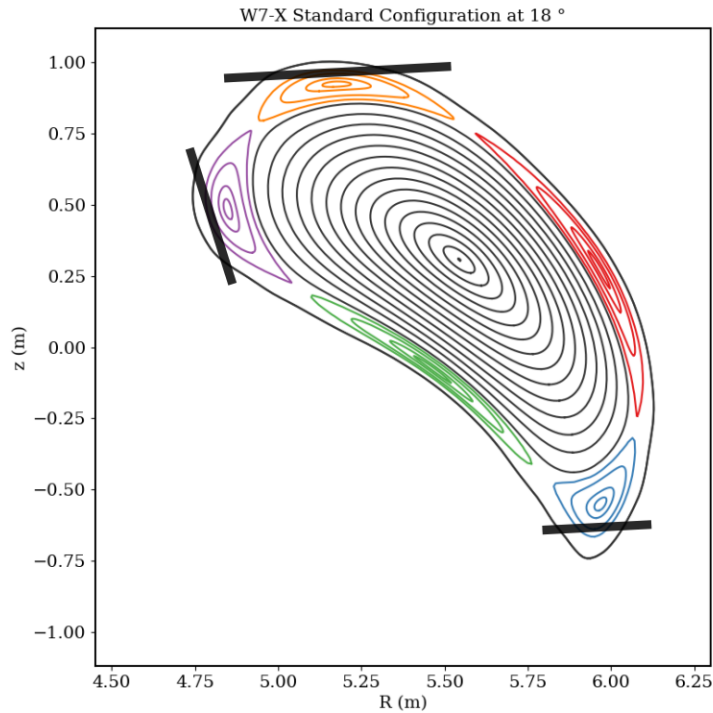


**Figure 1.3.:** Magnetic flux surfaces of a standard configuration plasma. Outside of the confined region of closed magnetic surfaces, there are 5 magnetic island (with color) in the SOL region. The divertor is displayed with black lines. Source: [24]

and the inner side of the plasma is called the High Field Side (HFS), as the magnetic field lines are less dense in the outer side than in the inner one.

To calculate the position of the flux surfaces given in the described coordinates, the Variational Moments Equilibrium Code (VMEC) is used. This code solves the magnetohydrodynamic force balance equation in the 3D geometry of W7-X for given pressure profiles [25].

### 1.2.3. Heating methods

At W7-X, two heating methods are currently used: Electron Cyclotron Resonance Heating (ECRH) [26] [27] and Neutral Beam Injection (NBI) [28] [29].

In the case of ECRH, an electromagnetic wave is introduced into the

plasma that matches the cyclotron frequency of the electrons ( $f_c$ ).

$$f_c = \frac{eB}{2\pi m_e} \quad (1.3)$$

$B$  is the magnetic field,  $e$  and  $m_e$  are the charge and mass of the electron, respectively. The electron cyclotron frequency of W7-X is  $\approx 140$  GHz [30]. The ECRH system is designed to create a microwave that is then lead into the plasma. As the magnetic field changes through the flux surfaces, so does the electron cyclotron frequency. The wave penetrates the plasma and transfers its energy to the electrons of the plasma with the corresponding frequency at a given location in the plasma. The fast energy transport on the given flux surface distributes this thermal energy on the surface.

The wave cannot propagate into the plasma, if its frequency is lower than the plasma frequency ( $\omega_p$ ) shown in Equation 1.4.

$$\omega_p = \sqrt{\frac{n_e e^2}{\epsilon_0 m_e}} \quad (1.4)$$

The plasma frequency is proportional to the square root of the electron density ( $n_e$ ). This means that above a certain electron density (cut-off density), the plasma frequency is higher than the electron cyclotron frequency. In these high density cases, the microwave does not reach the resonant surface, and therefore cannot heat the plasma. Instead, the second or third harmonic frequency of the electrons can be used. These however, have a lower absorption rate, particularly the third harmonic, making them less efficient. Using the first, second or third harmonic is referred to as  $X1$ ,  $X2$  and  $X3$  heating, respectively. The standard heating used at W7-X is  $X2$ . To access plasma regimes of electron density higher than the cut-off density for the  $X2$  heating, the polarisation of the microwave has to be changed. Heating with the second harmonic of circularly polarised microwave is referred to as  $O2$  heating. This is the utilised heating method as of now for electron densities above the  $X2$  cut-off density. [31]

During NBI heating, a beam of accelerated neutral hydrogen atoms is injected into the plasma that penetrates the magnetic field initially without interaction. The main processes [32] [33] between the neutral atoms and the plasma particles are listed in the following and shown in Figure 1.4. The dominating processes when colliding with a thermal hydrogen ions of

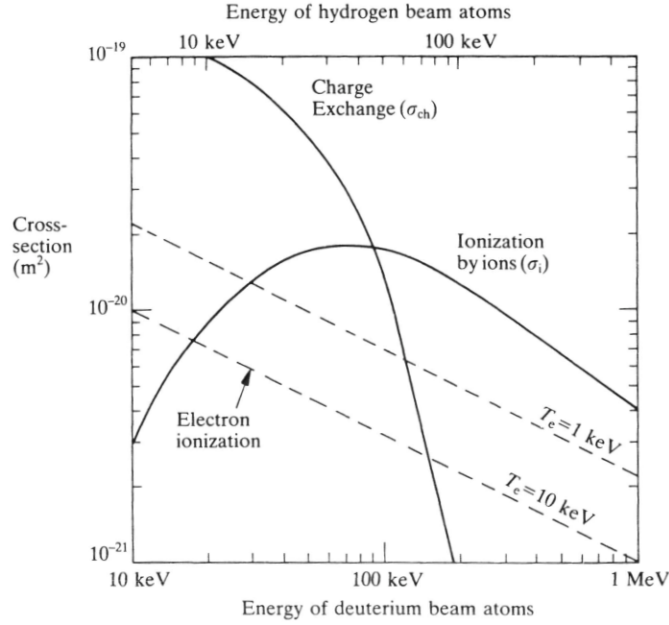
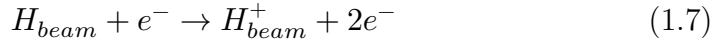
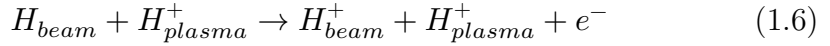
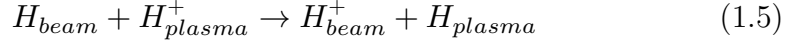


**Figure 1.4.:** Cross section for the main processes, charge exchange and ionisation, between a neutral beam atom and a thermal plasma ion, as well as effective cross section for ionisation of neutral beam atoms by electrons. All cross sections are shown as a function of the neutral beam energy. Source: [32] Fig. 5.3.1

the plasma are charge exchange and ion impact ionisation, described by Equation 1.5 and 1.6. Equation 1.7 displays electron impact ionisation, the main process when colliding with electrons of the plasma.  $H_{beam}$  and  $H_{beam}^+$  refer to neutral beam hydrogens and hydrogen ions created from the beam neutrals, respectively.  $H_{plasma}^+$  and  $H_{plasma}$  correspond to thermal hydrogen ions of the plasma and neutral hydrogen created from them, respectively. The neutral beam particles become fast ions in all these processes [34]. As their kinetic energy is higher than the energy of the plasma ions and electrons, most of them are thermalised via collisions, transferring their energy to the plasma ions and electrons while becoming part of the main plasma population themselves. Therefore, NBI fuels and heats the plasma at the same time. The beam neutrals can also collide with particles in the plasma other than the electron and main hydrogen ion population. The

main process between these impurities and the neutral of the beam is charge exchange. However, the density of the impurities is significantly lower than the density of the electrons and hydrogen ions, and therefore processes with them are negligible when discussing general properties and mechanisms of the neutral beam.



If charge exchange happens between a neutral beam atom and a thermal  $H^+$  ion of the plasma, the electron of the neutral hydrogen is transferred to the thermal ion (Equation 1.5), making the ion a neutral hydrogen. The lifetime of neutral hydrogen is short at the high temperatures of the plasma core, therefore these new thermal neutrals become ions again by either charge exchange with thermal ions or by ion or electron impact ionisation, shortly after being created. In case this process is again charge exchange with a  $H^+$  ion, the transferred electron will make that ion a thermal neutral hydrogen, and so on, creating a chain process as the reaction is repeated by the subsequent neutrals. After a certain amount of steps, the charge exchange and ionisation of the newly created thermal neutrals become balanced, and when this happens, the chain process dies out within a certain distance. This creates the so-called halo around the beam that consists of neutral hydrogen within a certain radius from the centre of the beam line.

The source of the neutral beam at W7-X is a positive hydrogen ion source [35]. Its ions are accelerated in an electric field to gain significant kinetic energy. The average acceleration energy of the NBI at W7-X is 50 keV. The accelerated ions are then lead through a background of neutral hydrogen. The neutral background atoms of the chamber transfer an electron to the accelerated ions via charge exchange, neutralising them. As the charge exchange process does not involve energy exchange, the now neutral atoms of the beam keep their earlier high velocity, when they are injected into the plasma. The neutralisation is not perfect, therefore the remaining high velocity ions are diverted by a magnetic field. [36]

During the measurement campaign OP1.2b, the length of NBI operation within one plasma discharge was limited to 5s due to wall safety reasons. Not all fast ions, created when the beam neutrals are ionised in the plasma, thermalise fully with the bulk plasma. These ions leave the plasma with still relatively high energy and can transfer large heat loads to small areas of the wall of the vacuum vessel, often in places not designed to take high heat loads, unlike the divertor. The total NBI injection time was limited in order to monitor and protect against melting of components in such areas. The NBI operation can be split into two types according to its length. When the NBI was operating for  $> 30$  ms, it is referred to as NBI pulse in the following. This typically means continuous NBI operation of  $0.5 - 5$  s in the investigated cases. NBI pulses of  $< 30$  ms are referred to as NBI blips. Blips were typically used in a series of consecutive pulses with the same length throughout a given discharge. In these cases, the average effect of one NBI blip on the global plasma conditions is negligible. The NBI blips are therefore suitable to be used as a neutral source for the Charge Exchange Recombination Spectroscopy (CXRS) system (see Section 3.1.1) so that the impurity conditions can be investigated in ECRH dominated plasma scenarios. The limit value of 30 ms was determined by several factors. It is marginally below the typical energy confinement time of the plasma, which means no significant heating effect compared to the existing plasma energy. Additionally, early measurements by the CXRS diagnostic showed that above 30 ms NBI operation the NBI begins to have a measurable effect on the plasma edge conditions and as such, the background intensity of the CXRS signal, as described in Section 3.1.2.

#### 1.2.4. Additional components and diagnostic systems

This work is based on the plasma diagnostic Charge Exchange Recombination Spectroscopy (CXRS). The theoretical and technical details of the CXRS diagnostic are described in Section 3.1.1. In the following section, diagnostic systems and additional components of W7-X are presented that provided supporting data for this work.

The Thomson Scattering diagnostic system is designed to measure the electron temperature and density profile. When an electromagnetic wave collides with a free charged particle, the charge starts to oscillate and emits radiation with the same frequency as the original wave. Thus, the wave

is scattered. This phenomena is called Thomson-scattering. For diagnostic purposes, a monochromatic infrared laser is injected into the plasma, and the spatially resolved scattered radiation is detected. The scattering on the plasma ions is negligible, as their oscillation is marginal due to their higher mass. The intensity of the scattered radiation is directly proportional to the density of electrons, allowing for electron density measurements. The scattered light is Doppler shifted due to the thermal velocity of the electrons, which is dependant on the electron temperature. Therefore, measuring the wavelength shift of the laser provides electron temperature measurements. Three lasers are shot into the plasma consecutively every  $\approx 100$  ms which gives the system's time resolution. [37]

The Interferometer diagnostic system measures the line integrated electron density. It uses the the change in the phase velocity of an infrared wave ( $\lambda = 5 - 10 \mu\text{m}$ ) passing through the plasma particles. The phase change happens due to the refractive nature of the plasma. At frequencies comparable to the plasma frequency, the phase velocity is proportional to the density of the refractive population, which are the free electrons in this case. A laser is shot through the plasma, and the line integrated electron density can be derived along the laser path. As this measurement is only sensitive to one plasma parameter, the electron density, it is used for the density control of the machine. [38]

Hydrogen pellets are frozen hydrogen balls of 2 mm that can be injected into the plasma. In the plasma, they are ionised and thermalised, becoming part of the main ion population. Penetration depth of 10 – 20 cm is achievable, which allows influence on the plasma core. The Hydrogen Pellet Injection system at W7-X is intended for deep fuelling the core and for flattening the density profiles in case of hollowness. Additionally, repetitive (10–30 Hz) pellet injection allows the investigation of enhanced performance (see in Section 3.2.6). [39] [40]

The Neutral Pressure Gauges diagnostic system measures the neutral pressure in front of the pumping duct of the vacuum vessel, close to the divertor. Hot cathode ionisation gauges are used which are applicable to high magnetic field environments, such as W7-X. The measurement is done at  $\approx 18$  different locations in the vessel. This is the only diagnostic at the time of this work that measures any parameters of the neutrals present in the machine. While this measurement cannot be done in the confined plasma region, it is suitable to provide a comparison for estimations on neutrals

within the LCFS. [41]

The X-Ray Imaging Crystal Spectrometer (XICS) is able to provide radial profiles of the ion temperature ( $T_i$ ), the electron temperature ( $T_e$ ) and the radial electric field ( $E_r$ ) [42] [43]. Trace amounts of *Ar* or *Fe* are injected into the plasma, the X-ray emission of which is imaged on a two dimensional detector through spherical bent crystals. Each channel of the spectrometer provides line integrated data. The profiles of the provided plasma parameters can be obtained by inverting the measured spectra (similarly to that described in this work in Section 2.1.3). The ion temperature measured by the XICS system was used as a comparison for the ion temperature profiles calculated directly from the CXRS spectra. The advantage of the XICS system in relation to the CXRS system is its ability to measure the inverted profiles during operation times without NBI heating. [44] [45]

### 1.3. Transport in plasmas

In this section, the fundamentals of particle transport in a fusion plasma are described as the basis for the focus of this work, the impurity transport.

The fundamental interactions between the particles in the confined region are Coulomb-collisions. The colliding particles suffer displacement which leads to diffusive and convective transport, characterised by the diffusion ( $D$ ) and convection velocity ( $v$ ) transport coefficients [46]. The characteristic size of the steps resulting from collisions is the radius of the gyro orbit of the particles. The diffusion is orders of magnitude higher along the magnetic field lines than perpendicular to them, with long mean free path between the collisions ( $D_{\parallel} \gg D_{\perp}$ ). This fast transport equalizes the temperature and the density of a given plasma population on a given flux surface on a time scale much shorter than the other components of the particle transport. This picture of colliding plasma particles is called classical transport.

Due to the toroidal geometry, additional drift forces are formed that increase the characteristic step size of the particles making their bounce orbit to reach further across magnetic surfaces. This is called neoclassical transport and is dominated by radial transport perpendicular to the magnetic field lines that increases  $D_{\perp}$  above the classical level. Neoclassical transport is always present in a toroidal plasma, and therefore sets a minimum level for the transport and thus, the transport coefficients.

To describe the particle movement due to collisions, the quantity collisionality ( $\nu_a^*$ ) is defined with Equation 1.8 [47]. The collisionality can be different for the main ion or electron population and the impurities [48].

$$\nu_a^* = \frac{\nu_a}{v_a} q R \epsilon^{-\frac{3}{2}} \quad (1.8)$$

$$v_a = \sqrt{\frac{k_B T_{e,i}}{m_{e,i}}} \quad (1.9)$$

$\nu_a$  is the collision frequency between the two given species that is determined by the collision rate in a given volume in a given time.  $v_a$  is the mean thermal velocity of the given particle species in a Maxwell-Boltzmann distribution shown at Equation 1.9.  $k_B$  is the Boltzmann constant,  $T_{e,i}$  is the electron or ion temperature and  $m_{e,i}$  is the mass of an electron or an ion.  $\epsilon$  is the inverse aspect ratio, the fraction of the minor radius ( $r$ ) to the major radius ( $R$ ), and  $q$  is the safety factor. The safety factor gives the number of toroidal rounds a given field line makes while one poloidal round is completed. In stellarators, its inverse is more commonly used, namely the rotational transform:  $\iota = 2\pi/q$  [49]. As both the toroidal and poloidal magnetic field vary with radius, so does the safety factor and the rotational transform.

The safety factor is closely connected with the stability of the plasma. It has been shown that for  $q \geq 1$ , the plasma reaches higher stability. This is due to the fact that for such a magnetic structure, the characteristic wavelength of some particular instabilities is longer than the radius of the machine, and thus the energy loss caused by those instabilities is heavily decreased.

The diffusive behaviour changes with the collisionality and different transport regimes can be defined [47], as seen in Figure 1.5. The radial diffusion coefficient, perpendicular to the magnetic field lines, was chosen to describe how strong the transport is.

When the collision frequency is low, and thus the mean free path is larger than the size of the device, some particles become trapped as they move on a flux surface. There is a movement perpendicular to the magnetic field, but the ratio of perpendicular and parallel kinetic energy is low enough to keep the particles around the flux surface. This regime is traditionally called

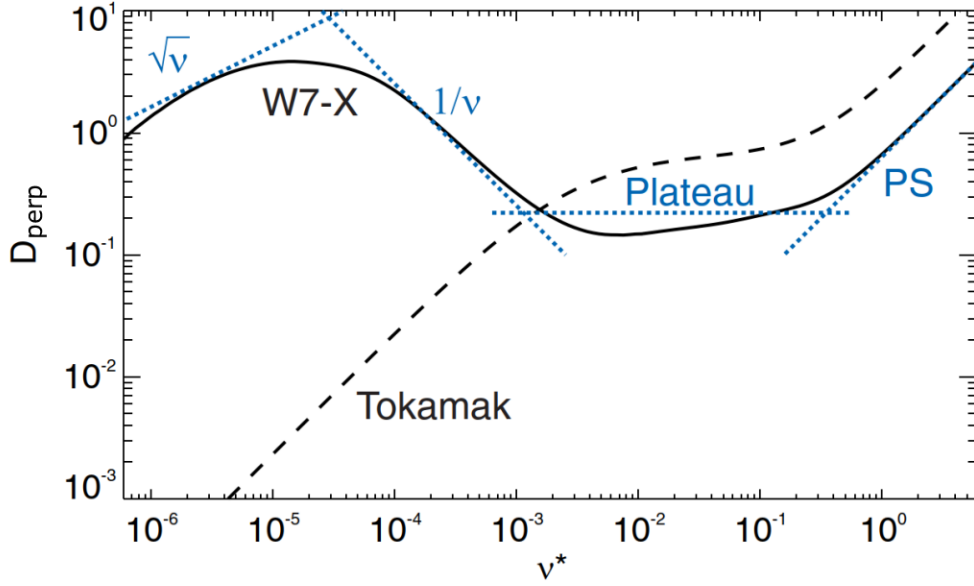


**Figure 1.5.:** Radial diffusion (perpendicular to the magnetic field lines) as a function of collisionality ( $\nu_a^*$ ), with solid black line for a W7-X standard configuration example and dashed black line for a tokamak as a comparison. A number of transport regimes can be defined, indicated by dashed blue lines: trapped ( $\sqrt{\nu_a^*}$  and  $\frac{1}{\nu_a^*}$ ), plateau and Pfirsch-Schütler regime. Source: [50] Fig. 4

the Banana regime, as the trapped particles follow orbits around the field lines that resemble the shape of a banana. Due to low collisionality, the particles can complete their orbits several times before they collide. The level of neoclassical diffusion is distinct for tokamaks and stellarators in this transport regime, as the trajectory of the particle orbits depend strongly on the magnetic structure of the device. In stellarators, the toroidal movement of the particle orbits can lead to the particles switching flux surfaces even without collisions due to the asymmetric magnetic field, resulting in neoclassical transport 1 – 2 orders of magnitude higher than in tokamaks. Part of the optimisation of W7-X was to create a magnetic geometry that allows the particles to stay on their original flux surface in case of low collisionality, decreasing the neoclassical transport in this regime. Two diffusion mechanisms can be distinguished in stellarators within the trapped regime due to

the ambipolarity condition. According to the condition, the radial electron and ion fluxes have to be equal. If this is not fulfilled, a radial electric field is created to shift the particle balance towards ambipolarity. In the lowest collisionality case, the diffusion is proportional to  $\sqrt{\nu_a^*}$  in stellarators and the electrons and ions are decoupled. These regimes are usually observed in ECRH dominated plasmas, where the electrons are the predominantly heated population, which results in  $T_e \gg T_i$  due to the decoupling. As a result, this case is not favourable for reactor-like conditions, as the ions are not sufficiently heated. The created positive radial electric field decreases the radial movement of the electrons, decreasing the neoclassical diffusion. This state is called electron-root regime. For higher collisionalities within the trapped transport regime, the diffusion changes according to  $\frac{1}{\nu_a^*}$ . This is called the ion-root solution of the ambipolarity condition, where the created radial electric field is negative. This is the regime relevant for reactor-like conditions.

As the collisionality increases, the characteristic collision time becomes shorter than the transit time of a trapped particle. Particles can gain enough perpendicular kinetic energy to break out from the trapped orbit and become passing particles. For  $\nu_a^* \approx \epsilon^{-\frac{3}{2}}$ , the collision times and mean free paths are so short that the orbits cannot be completed undisturbed and the radial transport is increased. This is the Pfirsch-Schütler regime. As the particle orbits are not fulfilled, the diffusion does not depend on magnetic geometry as significantly as in lower collisionality regimes. Therefore, the stellarator and the tokamak transport is similar at such high collisionality and the diffusion is directly dependent on the classical transport:  $D_{PS} \approx q^2 D_{cl}$ . The transition between the  $1/\nu$  and the Pfirsch-Schütler regime is called the Plateau. [50] [51]

The neoclassical transport can be numerically calculated as it consists of well understood physical processes [52]. Detailed neoclassical models are available for different W7-X plasma scenarios [53]. The level of collisionality and diffusion is determined by the global plasma parameters within the limits set by the shape of the device and the magnetic configuration. In standard ECRH dominated plasmas at W7-X, the neoclassical transport typically follows the high collisionality end of the trapped regime and the lower end of the Plateau regime. In NBI heating dominated plasma, the collisionality is predicted to increase and the neoclassical transport to be at

the high end of the Plateau regime or at the starting of the Pfirsch-Schütler regime.

The energy losses of the plasma seen in many experiments are 1 – 2 orders of magnitude higher than predicted by neoclassical models [54]. This means that there are additional transport effects present besides the neoclassical transport. These are collectively called anomalous transport. The anomalous diffusion is observed to be orders of magnitude higher than the neoclassical diffusion. This decreases the energy confinement time for a given plasma size and therefore increases the size a reactor would need to be to meet the required triple product condition (see Equation 1.1). Turbulent flows are found to provide a big part of the anomalous transport. Radial temperature or density gradients drive micro instabilities that cause fluctuations in the plasma. The underlying mechanism and causalities are not yet fully understood and are still being investigated. This is due to their complex behaviour and the fact that the length scale of these fluctuations is  $< 1$  cm and their time scale is  $< 1$  ms, making it challenging to detect and examine them. The perpendicular component of the turbulent transport is usually much higher than the perpendicular neoclassical transport, and therefore is often the predominant mechanism of the radial transport.

## 1.4. Impurities in fusion plasmas

In fusion plasmas, species that aren't hydrogen are called impurities. Their radiation can increase the energy losses of the confined plasma. Additionally, they dilute the plasma which is also not beneficial considering a fusion reactor, as it reduces the likelihood of fusion reaction between two hydrogen isotopes. However, radiation from impurities in front of the divertor contribute to distributing the heat load of the plasma on the divertor and other wall surfaces. Thus, the control of impurities in the plasma is crucial for future fusion devices. To be able to control them, their behaviour and its dependencies need to be understood. This provides the main focus of the presented work.

Low-Z and High-Z impurities are differentiated. Low-Z impurities are fully ionised for most of the confined plasma radius, therefore they do not cause power losses by line radiation. High-Z impurities do not get fully ionised in the plasma core, their line radiation causes significant losses to the plasma.

To describe the amount of impurities present in the plasma, considering its different particle populations, an effective ion charge ( $Z_{eff}$ ) is defined by Equation 1.10. It is the effective charge at the same total density that would lead to the same bremsstrahlung in the given plasma.  $n$  is the density and  $Z$  is the atomic number of a given species  $j$ .

$$Z_{eff} = \frac{\sum_j n_j Z_j^2}{\sum_j n_j Z_j} \quad (1.10)$$

Most impurities enter the confined region from the plasma facing elements. All impurities that are consistently present in the plasma to some extent are called intrinsic impurities. As the wall and divertor of W7-X is made of carbon, carbon is the main impurity present in this device. Carbon particles can leave the wall structure by interaction with the high temperature plasma particles that hit the wall at the end of the open field lines. There are several types of erosion reactions that can cause carbon atoms to leave the wall, the most significant being sputtering. Sputtering is a phenomenon in which particles of a solid material are knocked off due to high energy plasma particles hitting the solid surface [55]. An energy transfer takes place from the high energy plasma particles to the solid particles. As a result, a bombarding particle can directly weaken the bond between two carbon atoms (chemical sputtering) or electronic excitation can happen that lead to carbon particles being in anti bonding states (physical sputtering). These atoms enter the SOL, and get ionised. Most of them is being recycled in the SOL region, due to the retention ability of the magnetic islands. These ions do not diffuse into the confined region but get redirected towards the wall. The amount of carbon that leaves the wall can be described with the source rate, which gives the number of particles leaving the wall per second. Other intrinsic impurities in the W7-X plasma are oxygen and boron.

Impurities can also be present in the confined region as a result of an impurity injection for diagnostic purposes. These are called extrinsic impurities. The signature of some of these impurities can still be seen several discharges after their initial injection, however, a general decay of their content can be observed in each successive plasma discharge with no injection of the given impurity. Impurities like this are for example helium, nitrogen and neon and are typically injected at the plasma edge. Injections can be done into the core of the plasma as well, typically in order to investigate the time scale of

the injected impurities leaving the confined region [56] [57]. This is a measure for the impurity confinement time. The lower the impurity confinement time is, the better the ability of the plasma is to keep the impurities out of its core. This means better plasma performance due to reduced radiation losses. Typically core injected impurities are iron, argon, copper and silicon.

Typical low-Z intrinsic or injected impurities besides carbon are oxygen, nitrogen, helium, neon and boron. Typical high-Z impurities that are mostly injected, are iron and argon. [58]

As the impurity atoms enter the plasma, they get ionised due to the high temperature [59]. Moving radially inwards, the temperature increases, and the impurity ions step into higher and higher ionisation stages. A simple model describing the temperature dependence of the different ionisation stages is called collisional ionisation equilibrium (CIE) or coronal equilibrium [60]. It describes the balance between collisional ionisation from the ground state of the particles and recombination from the higher ionisation stages. This equilibrium is modelled for a given temperature and with all ions being in ground state. An other model describing the phenomena is the local thermodynamic equilibrium (LTE). This equilibrium differs from the coronal equilibrium, as it has all excited states of the ions populated. Figure 1.6 shows the emissivity of the ionisation stages of carbon as a function of temperature using both models. For this work, the coronal equilibrium was considered. According to Figure 1.6, the carbon ions are predominantly fully ionised for  $T > 200$  eV, this corresponds to most of the confined plasma radius at W7-X.

## 1.5. Impurity transport modelling

To understand the behaviour of impurities in the plasma, their transport need to be modelled. The impurity transport can be described by the radial continuity equation based on the law of particle conservation, as seen in Equation 1.11.  $n_{imp}^{Z+}$  is the density of a given impurity at a given ionisation stage,  $\Gamma_{imp}^{Z+}$  is the radial component of the flux density of the given impurity.  $Q_{sources,imp}^{Z+}$  and  $Q_{sinks,imp}^{Z+}$  refer to all the sources and sinks of the impurity, respectively, due to atomic processes like ionisation, recombination and charge exchange. Assuming a steady-state scenario, the sources, sinks and transport balance each other out. The impurity transport coefficients, and

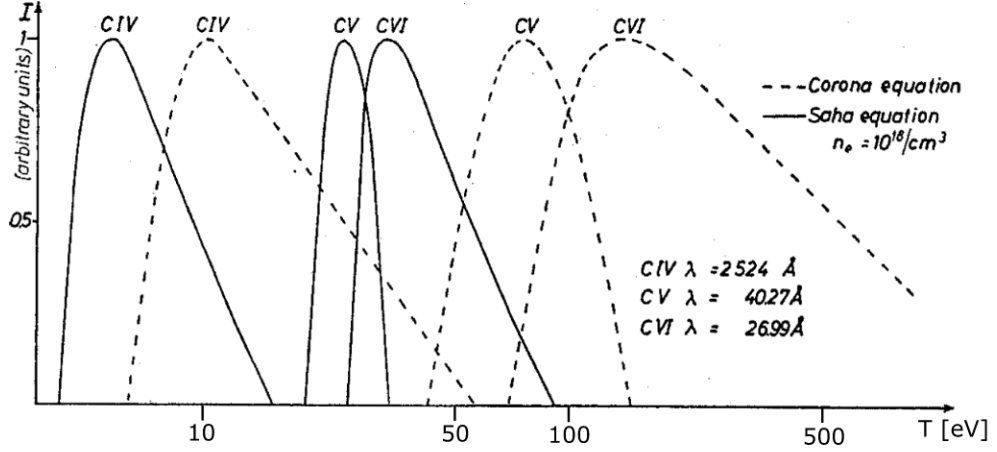


**Figure 1.6.:** Relative intensity of the radiation of carbon in different ionisation stages according to the coronal equilibrium (dashed lines) and the local thermodynamic equilibrium, which is described by the Saha equation (solid lines). Source: [61] Fig. 2, rescaled x-axis

therefore the transport times parallel to the magnetic field are orders of magnitude higher than perpendicular to the magnetic field, keeping the given impurity density constant on a given flux surface even if there are local sources and sinks (e.g. impurity injection). Thus, radial transport dominates the changes observed in the total impurity transport induced by the plasma behaviour. The driving processes of the radial impurity transport are the poloidal variations in the density and temperature gradients due to the distance of the magnetic surfaces being smaller at the HFS and higher at the LFS, and the  $1/R$  dependence of the toroidal magnetic field.

$$\frac{\partial n_{imp}^{Z+}}{\partial t} = -\frac{1}{r} \frac{\partial}{\partial r} (r \Gamma_{imp}^{Z+}) + Q_{sources,imp}^{Z+} + Q_{sinks,imp}^{Z+} \quad (1.11)$$

The radial component of the impurity particle flux is defined in Equation 1.12. The transport is described by the two transport coefficients, the diffusion ( $D$ ) and the convection velocity ( $v$ ).

$$\Gamma_{imp} = -D \frac{\partial n_{imp}}{\partial r} + v n_{imp} \quad (1.12)$$

Neoclassical calculations were done for W7-X that investigated the impurity behaviour in purely neoclassical transport regimes. These models predict impurity accumulation in the plasma core [62]. Accumulation is a transient process during which the number of impurity particles increases in the plasma core, in relation to the other radial regions of the confined plasma. This process can reach steady-state when the sinks and sources reach a balance. Accumulation often refers to when the rise of impurity density is continuous and it does not reach steady-state within the given plasma conditions, or when it does reach steady-state, however, the resulting level of impurity density is high enough to cause performance problems. Impurity ions accumulating like this as a result of the plasma configuration without a possibility to extract them out of the confined plasma region is not favourable for reactor-like conditions due to the resulting dilution and radiation losses. Previous impurity transport studies on the W7-AS stellarator show that the neoclassical transport properties heavily depend on the background plasma parameters [63]. Therefore, plasma configurations, where impurity accumulation can be avoided, need to be identified and investigated.

While neoclassical impurity transport can be precisely calculated for given background plasma parameters, anomalous transport can only be approximated by models and need to be compared with impurity density measurements. In this work, carbon density measurements are taken from the CXRS diagnostic to be compared with simulated results.

To investigate the level of anomalous impurity transport, the pySTRAHL modelling code is used in this work [64] [65]. PySTRAHL is a one dimensional code that calculates the radial transport of given impurities in the plasma. The code solves Equation 1.11 for each ionisation stage of the given impurities at given background plasma (e. g.  $n_e$ ,  $T_e$ ,  $T_i$ ) and edge conditions (e. g. source rate from the walls). The terms representing the sources and sinks of the given impurity stage connect the neighbouring charge states as described in Equation 1.13.  $S_{imp}^{Z+}$ ,  $\alpha_{imp}^{Z+}$  and  $\beta_{imp}^{Z+}$  are the rate coefficient for ionisation, recombination and charge exchange of the  $Z$  ionisation stage of the given impurity, respectively.

$$\begin{aligned}
 Q_{sources,imp}^{Z+} + Q_{sinks,imp}^{Z+} = & - (n_e S_{imp}^{Z+} + n_e \alpha_{imp}^{Z+} + n_H \beta_{imp}^{Z+}) n_{imp}^{Z+} \quad (1.13) \\
 & + n_e S_{imp}^{(Z-1)+} n_{imp}^{(Z-1)+} \\
 & + (n_e \alpha_{imp}^{(Z+1)+} + n_H \beta_{imp}^{(Z+1)+}) n_{imp}^{(Z+1)+}
 \end{aligned}$$

A one dimensional model is not well suited for describing the processes of the SOL and the interactions between the plasma and the wall. Thus, the modelling of this region is simplistic, using a few input parameters. A parallel loss time is defined, a characteristic decay length that corresponds to the parallel transport to the divertor. Additionally, a source rate can be defined with which the impurity is entering the plasma at the boundary either by injection or by continuous flow from the wall components.

For the numerical solution of the impurity transport equation, the radial dependency of background plasma parameters is needed: electron density ( $n_e$ ), electron temperature ( $T_e$ ), ion temperature ( $T_i$ ) and neutral hydrogen density ( $n_H$ ). Radial profiles of the transport coefficients: diffusion and convection velocity are also required. The code handles given neoclassical and additional anomalous transport coefficients separately. The result of the simulation with the given input profiles and parameters is the radial profile of the impurity density for all ionisation stages.

# Chapter 2.

## Passive Spectroscopy

A Passive Spectroscopy system was set up at Wendelstein 7-X to measure spectral lines of low-Z impurities present in the plasma. It aims at investigating the radial distribution and possibly content of carbon, the main impurity present in the plasma, in order to investigate its transport and possible effects on the plasma in different configurations. The density of the carbon can be estimated from the intensity of the spectral line [59]. The measured radiation is line integrated along the given LOS, thus an inversion method was needed to assess the radial distribution.

In this section, the experimental setup and the results from the Passive Spectroscopy system will be presented from OP1.2a. A different Passive Spectroscopy system was set up at the same viewing location during OP1.2b, but the measured data from this system has not been analysed. The camera used in OP1.2a was used for the Active Spectroscopy system during OP1.2b, as the focus of this work was moved to analysis based on that diagnostic (see Chapter 3). Other cameras were tested for the OP1.2b Passive Spectroscopy system, but none gave sufficient signal to noise ratio for a feasible analysis.

### 2.1. Methods

#### 2.1.1. Observation system at W7-X

The core of the diagnostic system is a multichannel Czerny-Turner mirror spectrometer able to look at spectral lines in the visible wavelength range. During OP1.2a, it was set to the  $C^{5+}$  spectral line at 529.07 nm which is the result of the transition from state  $n = 8$  to state  $n = 7$ .

The line radiation is collected by fifteen 400  $\mu\text{m}$  optical fibres at the

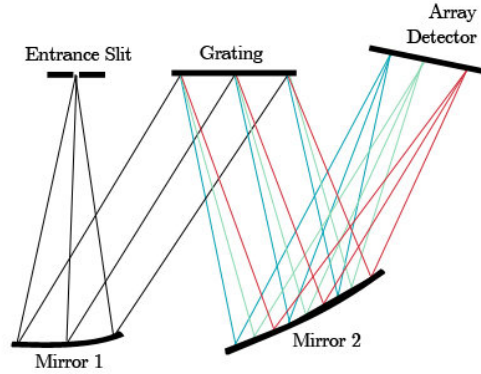


**Figure 2.1.:** Schematic structure of a typical Czerny-Turner spectrometer. The spectrometer used for measuring the line-integrated radiation coming from the plasma is arranged according to this setup.

AEK41 port of module 4 of W7-X. A metal box is installed on the outside of a vacuum window looking in the direction of the plasma. On the opposite end of the box is an array of optical fibres which leads from the stellarator to the laboratory where they are connected to the spectrometer. A schematic image of the structure of the spectrometer can be seen in Figure 2.1, its specific parameters are listed in Table 2.1. After entering the spectrometer through the entrance slit, the light is reflected and collimated by a curved mirror to the grating, which splits the light according to wavelength, then a second mirror focuses the radiation from different wavelengths. Finally, the light is detected by a PiCam (Princeton Instruments) CCD camera at the chosen wavelength range (523.8 – 530.1 nm) that transforms the measured light intensity into a 2 dimensional digital image. One dimension is the wavelength direction with 1024 pixels, the other dimension is along the optical fibres as described below.

To detect line-integrated radiation from different volumes of the plasma, multiple Lines of Sight (LOS) are used. Every LOS is represented by an optical fibre. A slice of the plasma is imaged onto the array of fibres at the machine and then the same array of fibres is imaged onto the CCD at the spectrometer. All LOSs used for this diagnostic system can be seen in Figure 2.2 in relation to the flux surfaces of a standard plasma equilibrium.

Two main bundles of optical fibres were used. One is the so-called Edge-

**Table 2.1.:** Parameters of the Czerny Turner mirror spectrometer that were used for the Passive Spectroscopy system during OP1.2a.

<b>Manufacturer and Model</b>	Spex 750M
<b>Focal length</b>	750 mm
<b>F number</b>	1/6
<b>Slit width</b>	Variable 8 – 200 $\mu\text{m}$
<b>Grating</b>	2400 $\text{nm}^{-1}$

VIS bundle, which looks through the outer half of the plasma volume (solid lines in Figure 2.2). The outer most LOSs are close to the LCFS or look directly through the SOL, depending on the configuration, allowing the examination of changes in the plasma edge. There are 11 optical fibres in this bundle that were connected to the spectrometer. The other fibre bundle is the so-called Pellets-K bundle that looks through the core region of the plasma (the name Pellets-K was given as this bundle was originally designed to look at active charge exchange with donor neutrals from pellet injection). The Pellets-K bundle had 4 fibres that were connected to the spectrometer. Thus, all together 15 fibres were used of the total of 50 fibres from the two bundles. This number was limited by the spectrometer at hand. The LOSs were fairly evenly distributed throughout the plasma radius, with higher resolution at  $0.7 < \rho < 1.0$  taking into account that the outer plasma is where the  $C^{5+}$  emission was expected to be seen which is the main region of interest in this analysis. The radiation collected by these 15 fibres appearing on the CCD image is shown in an example in Figure 2.3. This is not the raw image measured by the CCD camera, but an image to which a relative intensity calibration as described in Section 2.1.3 is already applied. A LOS is also referred to as "channel" in the following.

### 2.1.2. Processing the measured spectra

An example spectrum of the  $C^{5+}$  line measured by a given channel is shown in Figure 2.4. The value of spectrum corresponds to the radiation detected by the given channel (number of photons,  $n_\gamma$ ) emitted by a given surface

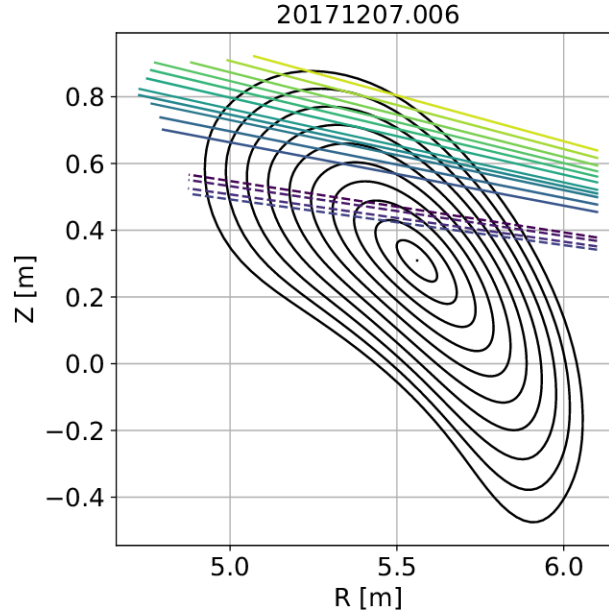


**Figure 2.2.:** All lines of sight of the Passive Spectroscopy system shown for standard equilibrium flux surfaces as a function of the radial (major radius,  $R$ ) and vertical ( $Z$ ) coordinates. The numbers are given from the full set of 80 channels available.

( $\text{m}^{-2}$ ) per light cone (steradian,  $\text{sr}^{-1}$ ) per unit wavelength ( $\text{nm}^{-1}$ ) per unit time ( $\text{s}^{-1}$ ). Thus, its dimension is  $N_\gamma \text{ sr}^{-1} \text{ m}^{-2} \text{ nm}^{-1} \text{ s}^{-1}$ . Two types of background radiation have to be considered, bremsstrahlung and background not originating from the plasma, like stray light radiation in the torus hall collected by the optical fibres and camera noise. The latter will be called no plasma background in the following. It is measured right before and after the plasma discharge. Both backgrounds are displayed in Figure 2.5 besides the measured spectral line with a narrowed down wavelength range. After subtracting both backgrounds, the intensity of the line is calculated by fitting a Gaussian to the spectrum in the displayed wavelength range and taking the area under it. Only a narrowed range is used for the fit, because spectral lines of other impurities can be present throughout the measured spectrum (for instance  $\text{Ne}^{9+}$ ). Additionally, the baseline coming from the

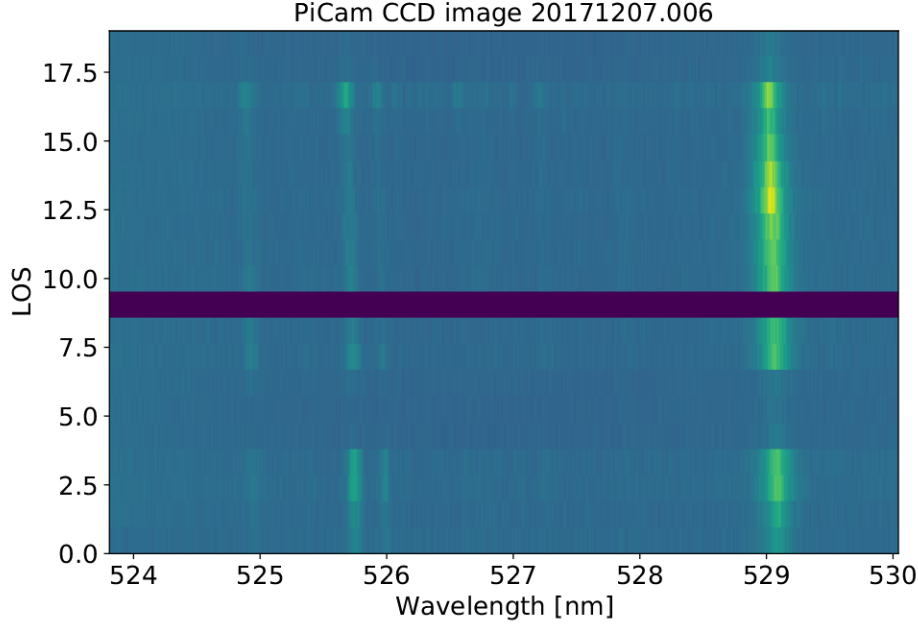


**Figure 2.3.:** Example image of radiation from the plasma as detected by the CCD camera. The horizontal axis is the wavelength, the vertical axis represents the different channels. The colour scale shows the photon count of a given channel at a given wavelength. One channel was used as a calibration channel, and thus it does not detect any light from the plasma.

two backgrounds cannot be approximated by a constant throughout the whole measured wavelength range, as seen in Figure 2.4, while assuming a constant background is feasible within the immediate surrounding of the  $C^{5+}$  line. Taking the area under the Gaussian eliminates the wavelength dependency, making the dimension of the intensity  $N_\gamma \text{ sr}^{-1} \text{ m}^{-2} \text{ s}^{-1}$ .

Before fitting, a wavelength and a relative intensity calibration is applied to the spectrum. The wavelength calibration is conducted by a  $Ne$  lamp to obtain the dispersion (nm/pixel). Three  $Ne$  spectral lines in the wavelength range of the camera give three fixed points to determine the dispersion function. Since the exact wavelength range differs to some extent for different channels depending on their exact location to the grating, the radiation of

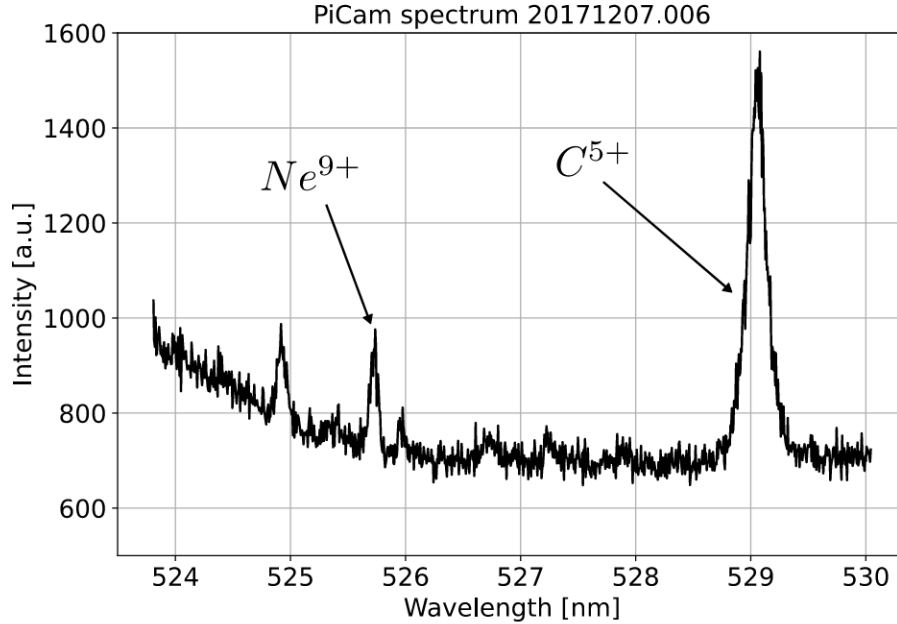


**Figure 2.4.:** Example spectrum of one channel with the  $C^{5+}$  line as measured by the CCD camera. It can be seen that the baseline of the spectrum is changing gradually throughout the detected wavelength range. The background can be approximated as a constant in the vicinity of the spectral line of interest.

the *Ne* lamp is measured by every channel separately. A second order polynomial is fitted to the three known points for each channel. Using this dispersion function, the horizontal axis is transformed from pixel to nm. One channel was not connected to the observation of the plasma, but was used as a calibration channel connected to the *Ne* lamp throughout OP1.2a for wavelength calibration on every morning of a measurement day. This was necessary because the exact wavelength range can change with time because of changes of room temperature. Furthermore, a relative intensity calibration is needed between the channels. The amount of light transferred by the fibres from the plasma to the entrance of the spectrometer and then to the detecting camera is different for each fibre. The losses that reduce the amount of light depend primarily on the quality of the given fibre as

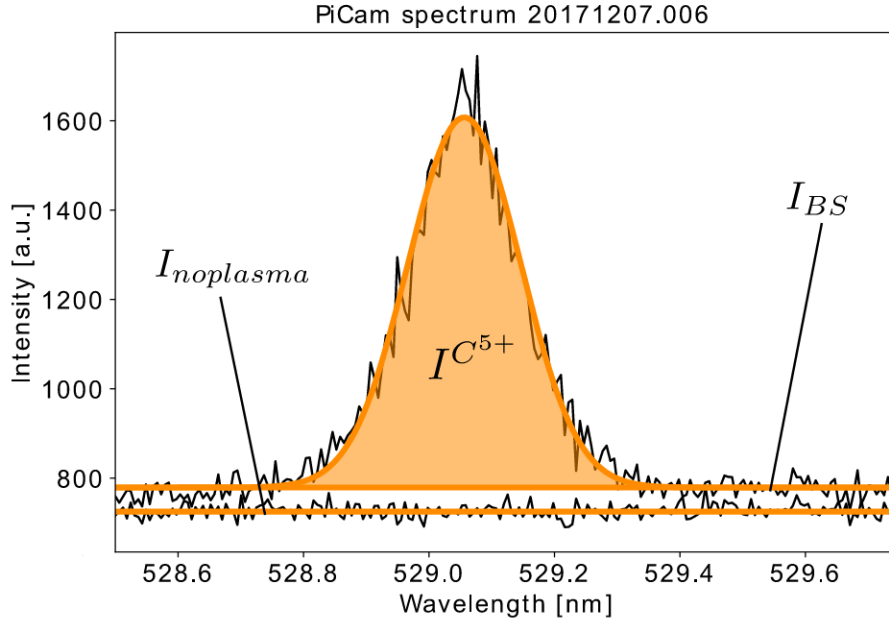


**Figure 2.5.:** Measured  $C^{5+}$  spectral line in black with the fitted Gaussian and its baseline in orange. The no-plasma background is also displayed in black with a fitted constant in orange. The difference between the no-plasma background level and the baseline of the Gaussian is the bremsstrahlung level. The intensity derived from the spectrum is the area under the Gaussian, displayed as the enclosed orange area.

well as the exact position within the fibre bundle. Fibre connectors are also a major source of deviations between the light level of the fibres. By conducting an intensity calibration where all of the fibres are illuminated with the same intensity, this difference in light level can be determined. The intensity calibration was done with a calibration sphere. The sphere emits homogenous light on all wavelengths, and is placed in front of each channel for calibration. By measuring the emitted known light intensity (number of photons per second) with each channel, the difference in their light level, as well as their conversion from the electron count of the camera to the detected photon count can be calculated. From the intensity levels measured during the calibration, a so-called calibration factor,  $0 < F_{cal} \leq 1$  is calculated for

each fibre, which the measured plasma spectrum of each channel is divided with accordingly.

### 2.1.3. Forward modelling to obtain carbon emission intensity

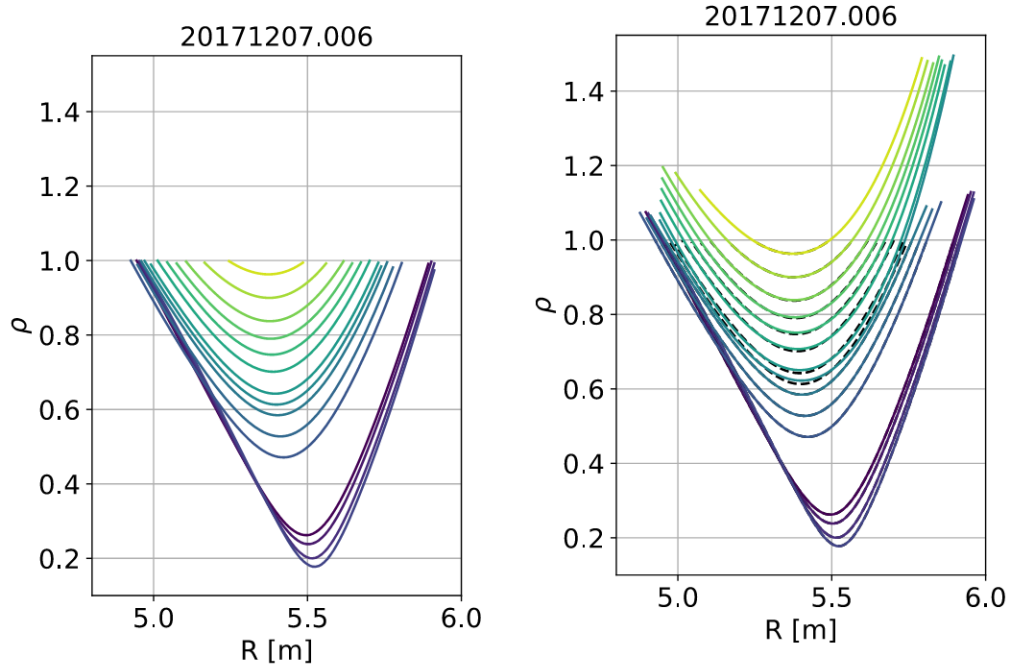
As the intensity measured by the spectrometer is line integrated along the given LOSs, an inversion needs to be done to determine the radial profile of the  $C^{5+}$  distribution [66]. Forward modelling was chosen as the base of the conducted inversion. Forward modelling is an analytic method during which a simulation of a known quantity is considered, then the input of this simulation is iterated so that the output matches the measurements. This is called an inversion. In this case, the known quantity is the measured line integrated intensity curve as a function of channels, where every value represents a LOS. The input quantity that is intended to be recreated is the radiant flux emitted by  $C^{5+}$  ions from a given plasma volume. It is assumed to be constant on flux surfaces (see later discussions). Thus for the inversion, it is modelled as a function of  $\rho$ . It will be called emission intensity in the following.

The spectral radiation emitted by the  $C^{5+}$  ions is directly correlated with the density of the ion. Additionally, it depends on plasma parameters such as  $n_e$ ,  $n_i$ ,  $T_e$ ,  $T_i$ . It is a flux surface quantity that changes from flux surface to flux surface as all the above mentioned quantities are. Although it is theoretically possible to model the emission based on these quantities and assumptions on the thermal equilibrium, this work does not aim at separating the  $C^{5+}$  density itself from a given emission intensity. The analysis focuses on the radial distribution on the  $C^{5+}$  emission intensity instead of the density profile of the ion. It is important to note that an absolute intensity calibration was not applied to the Passive Spectroscopy data, thus every subsequent intensity and emission intensity calculated using these intensities does not have absolute values. The profile shape and relative values are sufficient to make observations on the radial distribution of the  $C^{5+}$  emission intensity in the plasma.

A couple of additional assumptions are made for the forward modelling. The line integrated intensity measured by one channel of the Passive Spectroscopy camera is theorised to be the emission intensity integrated over

the flux surfaces the given LOS looks through. For a full calculation, the cone of the LOS should be treated in three dimensions. The width of the cone is estimated to be  $\approx 2$  cm. Furthermore,  $\rho$ , the quantity describing the flux surfaces, should also be treated as a three dimensional grid, taking into account its resolution coming from the VMEC calculations. For simplicity, the LOS is approximated as a one dimensional line, thus a one dimensional integral is used instead of a volume integral. This makes the dimension of the emission intensity  $N_\gamma \text{ sr}^{-1} \text{ m}^{-3} \text{ s}^{-1}$ . In summary, the line integrated intensity is calculated by adding up the emission intensity of the flux surfaces the LOS is looking through.

The designed position of every LOS in relation to the plasma vessel, hence in cylindrical coordinates, were calculated by the design CAD model of the diagnostic. After installing the diagnostic system, a calibration was done to inspect where the LOSs are in reality in relation to the designed setup. This calibration was done before the measurement campaign started. A selection of channels were illuminated from the laboratory, so that a light spot could be seen inside the plasma vessel on the wall where the sight lines of the selected channels end. Connecting the coordinates of this spot with the position of the optical head, the coordinates of the LOSs were calculated. The difference between the measured and designed ending coordinates of each LOS was a few cm. The optical head was moved manually to make this difference sufficiently small such that the designed coordinates could be used for further analysis. The intersection between each LOS and the equilibrium flux surfaces of the given magnetic configuration is calculated, providing the flux surface array each LOS looks through. Every flux surface is represented by a value of  $\rho$ . In Figure 2.6a, the sets of  $\rho$  values corresponding to each LOS are shown as a function of major radius ( $R$ ). The left and right half of the image corresponds to the LFS and HFS, respectively. The VMEC equilibria is calculated for  $\rho < 1$ , in other words until the LCFS. As the highest occurrence of the observed  $C^{5+}$  is expected to be close to the LCFS,  $\rho(R)$  is extended to  $\rho > 1$  to get a wider measurement range. The extension is done in two ways. For LOSs that look through the inner part of the plasma as well ( $\rho < 0.6$ ) besides the plasma edge, a linear extrapolation of the outer most five points is done on both the LFS and the HFS end of the curves. A linear extrapolation is not suitable for the curves corresponding to the remaining LOSs (that look through only  $\rho > 0.6$  plasma regions) due to the changing shape of the curve according to how deep the LOS looks through the plasma.



(a)  $\rho$  arrays determined directly from the intersections of the designed path of each LOS and the flux surfaces.

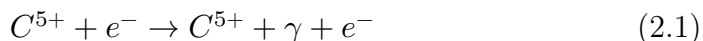
(b) Fitted polynomials on each  $\rho$  curve, as well as the extrapolation of these fitted functions for  $\rho > 1$  and the original curves in dashed black lines in the background.

**Figure 2.6.:** Arrays of  $\rho$  representing the flux surfaces each LOS is looking through and thus, detecting radiation from. They are shown as a function of major radius ( $R$ ). The colour of curves of each LOS corresponds to the colours shown in Figure 2.2.

For the remaining LOSs, the curves are less steep on the side. Carrying out a linear extrapolation on these curves would give an unrealistic result where the curves cross each other and heavily deviate from the original order of the LOSs. Therefore, a third polynomial function is fitted to the  $\rho(R)$  function for these remaining LOSs, and the polynomials are extrapolated on each side of the curves. This extension model is physically invalid as there is a set of magnetic islands outside of the LCFS making the flux surface structure

more complicated, as well as dependent on the poloidal and toroidal angle additionally. Nevertheless, the presented method to extrapolate  $\rho(R)$  is used initially. Later results show that the emission intensity in the SOL is not required to explain the observed radial distribution, thus the used extension method is acceptable for the scope of the current analysis. The fitted and extrapolated functions together with the original  $\rho(R)$  curves can be seen in Figure 2.6b for each LOS.

To make the inversion, the shape of the input emission intensity is parametrised based on previous results from other experimental fusion devices [66]. Then parameters of this function are fitted with least square fitting method to match the output line integrated intensity to the measured intensity. To approximate the profile shape and the initial guess for the parameters of this function, we need to estimate which part of the plasma volume the measured radiation is mostly coming from. For this, the corresponding atomic processes leading to the measured ion need to be considered. There are two main sources for  $C^{5+}$  to appear in the plasma: electron impact excitation of  $C^{5+}$  and charge exchange between  $C^{6+}$  and thermal neutrals. The processes are shown in Equation 2.1 and Equation 2.2, respectively. Other processes can lead to  $C^{5+}$ , such as ion impact excitation and recombination, however, the contribution of these processes to the measured signal at the investigated plasma conditions is negligible.



The first process to be considered is electron impact excitation from  $C^{5+}$ . When the surrounding temperature becomes high enough,  $C^{5+}$  ions take enough energy according to the coronal approximation so that their outermost electron is emitted and the ions become  $C^{5+}$ . This process is expected to happen in the plasma region with the necessary temperature of  $\approx 50 - 150$  eV according to the coronal approximation. This temperature corresponds to  $\rho \approx 0.95 - 1$  given the electron temperature measured by the Thomson Scattering diagnostic as shown in Figure 2.7 for an example discharge of interest.

The other main process to take into account is charge exchange with a neutral atom. When a positive ion collides with a neutral atom in the

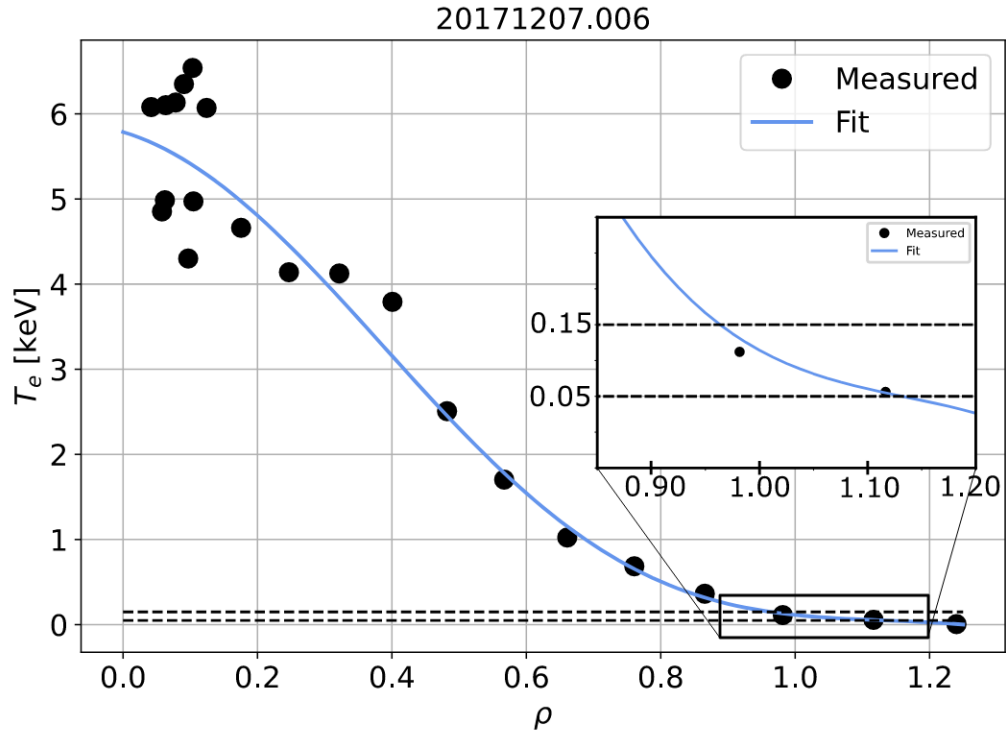


**Figure 2.7.:** Electron temperature measured by the Thomson Scattering diagnostic at  $t = 3$  s during discharge 20171207.006.

plasma, one of the neutral's electrons can be transferred to the ion. When one of these neutral atoms collide with a fully-ionised  $C^{6+}$  ion, the ion will become  $C^{5+}$ . Charge exchange is the dominant collision process between neutrals and ions, especially at the high temperature of W7-X plasmas.

A significant population of neutral atoms can be introduced to the plasma via an external source, like the Neutral Beam Injection heating system. The effect of these neutrals was used and investigated by the Active Spectroscopy system (see Chapter 3). Additionally, thermal hydrogen neutral atoms are present in the plasma also without a dedicated external source. These neutrals are created via recombination between a main plasma ion and an electron. The probability of this process is highest in the low temperatures outside of the LCFS, close to the divertor targets, and significantly decreases as the temperature rises towards the plasma boundary and further in. Once

created at the divertor, a small fraction of these neutrals can diffuse inside the LCFS before being re-ionised. These so-called "recycling neutrals" are the neutral source of charge exchange with  $C^{6+}$  in the experiments during OP1.2a when the NBI system was not yet fully installed. The probability of re-ionisation increases with the increase of the electron density and therefore it is significantly higher close to and inside the LCFS than in the rest of the SOL, where the electron density is lower. The density of the neutral population in the confined region is not expected to be noticeable for  $\rho < 0.9$ . At the time of this analysis, there is no diagnostic at Wendelstein 7-X measuring the density of these thermal neutrals inside the LCFS, thus there is no measurement aiding the estimation of the radial distribution of the neutral particle density.

Given these two sources for the detected  $C^{5+}$  line radiation, it can be assumed that the distribution of the measured ion is a sum of the radial distribution of  $C^{5+}$  ions and that of thermal neutrals. A Gaussian or Gaussian-like function is usually a safe starting point for distributions like this as both populations are mainly found in a specific range within the full radius with smooth decline towards the core and edge. The two source distributions of the emission intensity of  $C^{5+}$  were tested to be represented by one common Gaussian or two separate Gaussian. This was done as at this point of the analysis, it was unconfirmed which one or whether both played a significant role in creating  $C^{5+}$ . Both symmetrical and two-sided Gaussian functions were tested for both cases. The results showed that the two sources need to be handled with separate peaks. However, making these two Gaussian two-sided does not improve the precision of the fit significantly. Thus, the addition of two symmetric Gaussian was chosen for the analysis, as this shortened the time need for the inversion. The function is described by Equation 2.3.

$$f(x) = a_1 \exp\left(\frac{-(x - x_{0,1})^2}{2\sigma_1^2}\right) + a_2 \exp\left(\frac{-(x - x_{0,2})^2}{2\sigma_2^2}\right) \quad (2.3)$$

$a_1$  and  $a_2$  are the value of the maximum,  $x_{0,1}$  and  $x_{0,2}$  are the position of the maximum,  $\sigma_1$  and  $\sigma_2$  are the quadratic mean width of the respective single Gaussian peaks. The quadratic mean width is connected to the Full Width at Half Maximum:  $FWHM = 2\sqrt{2\ln 2}\sigma$ . To conclude, a double Gaussian function was chosen to approximate the overall profile shape of

the emission intensity, assuming that each Gaussian represents one of the sources for the measured ion. This assumption is not entirely confirmed, even though this chosen method gives acceptable fits to the measured data.

## 2.2. Investigation of carbon content in the outer plasma

For detailed analysis with Forward modelling, one particular discharge, 20171207.006 was chosen. An overview of the discharge is presented in the following. Figure 2.8 shows the time evolution of the main global plasma parameters. This experiment is particularly of interest because this is the record high performance discharge of OP1.2a with record triple product values [67]. This is achieved by injecting a series of pellets into the plasma at  $t = 1.2 - 1.8$  s, with the high performance phase with the maximum triple product happening after the pellet phase [40]. While investigations on the high performance phase is not the focus of this analysis, using a discharge generally in the interest of other diagnostics is beneficial as well analysed and validated measurements are available for these experiments. Worth mentioning is a singular, presumably magnetic fluctuation related event happening at 2.3 s [68]. Its short effect can be seen in the line integrated density. The plasma is undisturbed after this event until the plasma termination starts.

The line integrated intensity extracted from the fitted Passive Spectroscopy spectrum of each channel is shown in Figure 2.9 as a function of time, together with the line integrated electron density for reference. Considering the pellet phase, a sudden intense and short peak can be observed occasionally in a few channels. This is directly an effect of the pellets, as they consist of neutral hydrogen, providing a source for charge exchange with fully-stripped carbon. However, the neutral atoms of the pellets are extremely short-lived, with an average life time of 0.5 – 1 ms before being ionized [39], thus they don't have any long-term effect on the  $C^{5+}$  content. Additionally, as pellets are small (diameter of 2 mm) compared to the width of a LOS cone ( $\approx 2$  cm) and their trajectories show an angular scatter of  $5^\circ$  in the plasma [39], they affect the measured  $C^{5+}$  intensity only randomly in a few channels. At the singular magnetic event, the  $C^{5+}$  increases signific-

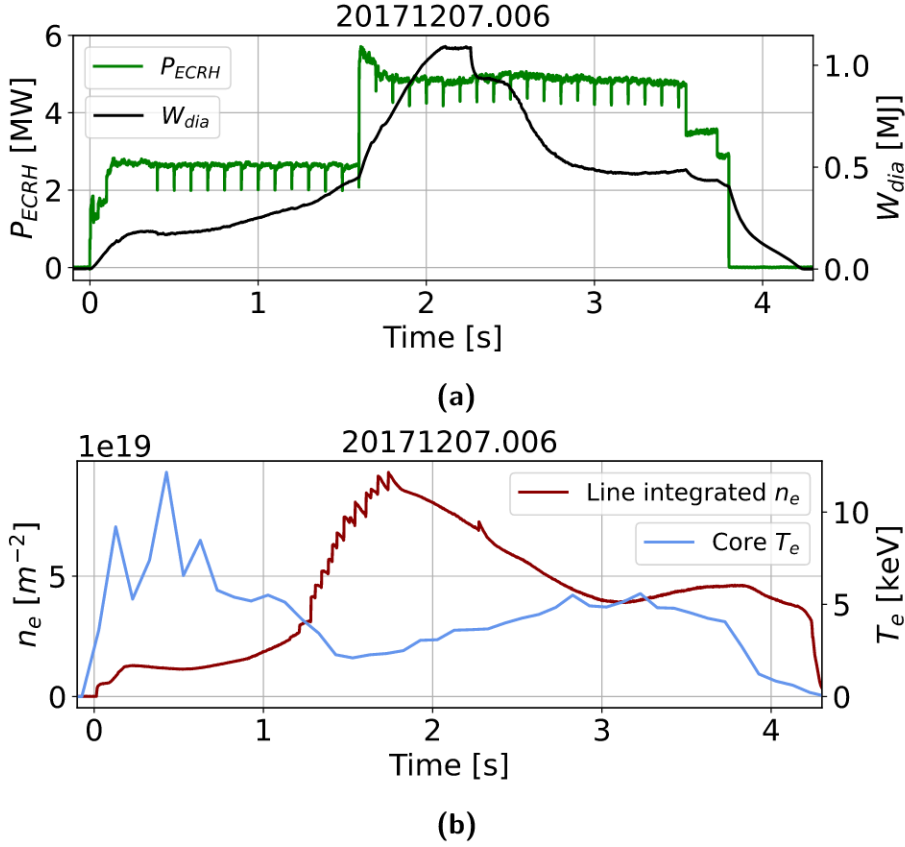


**Figure 2.8.:** Time evolution of plasma parameters during discharge 20171207.006. ECRH power is shown in green and diamagnetic energy shown in black (a). Line integrated electron density measured by the Interferometer shown in dark red and core electron temperature measured by the Thomson Scattering diagnostic in blue (b).

antly on all channels, then decreases with a high, but noticeable decay time. Shortly after, there is a smaller, but longer lasting bump in the measured intensity, even though there is no particular change to be seen in the plasma parameters. Nonetheless, this singular event and its effects are under investigation within other projects without a reliable conclusion as of now [68]. For the  $C^{5+}$  emissivity analysis, an unperturbed plasma phase was chosen:  $t = 2.6 - 3.5$  s.

An example measured line integrated intensities for each channel at 2.7 s

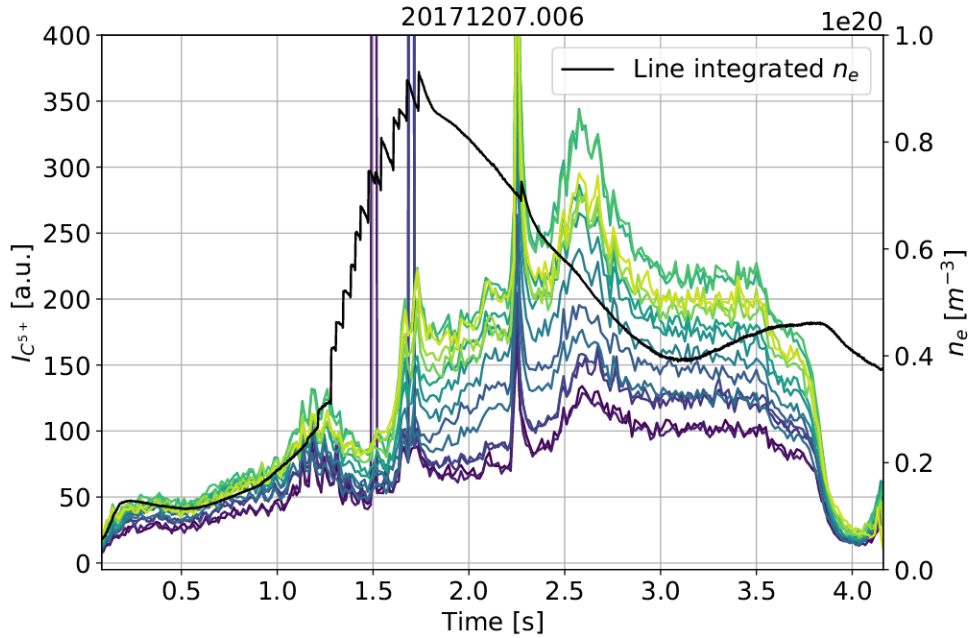


**Figure 2.9.:** Time evolution of the measured line integrated intensity during discharge 20171207.006. The coloured curves refer to the LOSs shown in Figure 2.2. The black curve is the line integrated density from the interferometer. The time range of interest is  $2.6 \text{ s} < t < 3.5 \text{ s}$  when the plasma was in a stable phase.

is shown in Figure 2.10 in black. In general, higher numbered channels detect higher intensities, this is due to the fact that those channels are looking through more plasma edge volume, while the lower numbered channels look more through the middle region of the plasma, thus only catching light from the edge right after entering and right before leaving the plasma, as seen in Figure 2.2. Two peak like shapes can be observed at the right side of the curve that are consistently present throughout the discharge. It is possible that these are correlated with the two relevant emission processes leading to  $C^{5+}$  and their different location within the plasma radius, but the fits are needed to confirm this. The line integrated intensities for each channel calculated from the double Gaussian shaped emission intensity fit applying the Forward model are shown in red in Figure 2.10. The fitted intensities

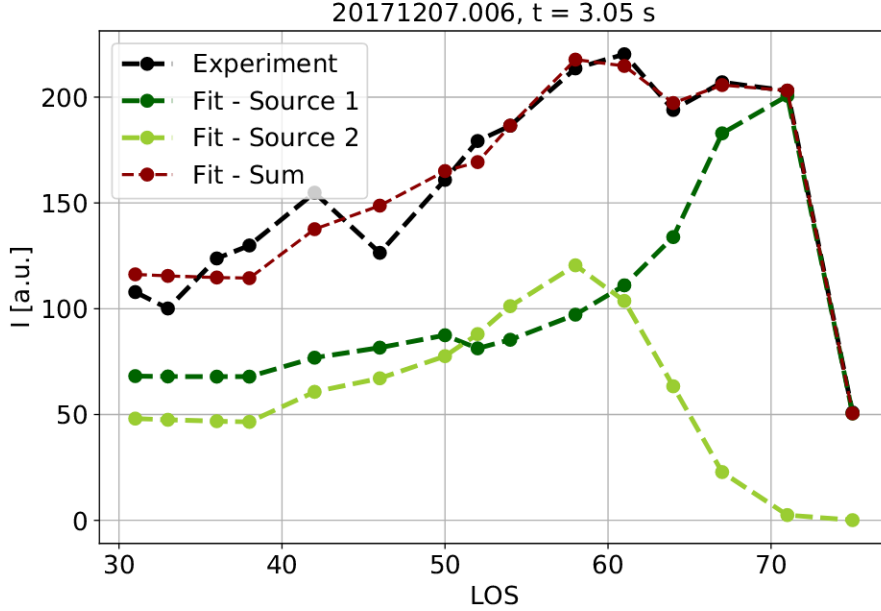


**Figure 2.10.:** Measured line integrated intensity curve as a function of channels at  $t = 2.14$  s in black with the fitted intensities from the inversion process in red. The light and dark green curves are the intensities derived from the two Gaussian of the emissivity separately, representing the electron excitation and the thermal neutral contributions. It seems to be clear that the two bump-like structure in the detected line integrated intensity curve can be traced back to the two sources individually.

agree well with the experimental values for the higher channel numbers, which is the main region of interest. The accuracy of the fit is lower for the channels looking through the core plasma, but still sufficient. The overall fit precision could most likely be improved with a more sophisticated emission intensity shape, but the agreement between the measured and fitted curve is applicable enough for the aim of this analysis. The inversion was done for all time points throughout the discharge and the quality of the fit is similar for the further time points of the steady-state phase as shown in Figure 2.10.

The line integrated intensities for each channel calculated separately from

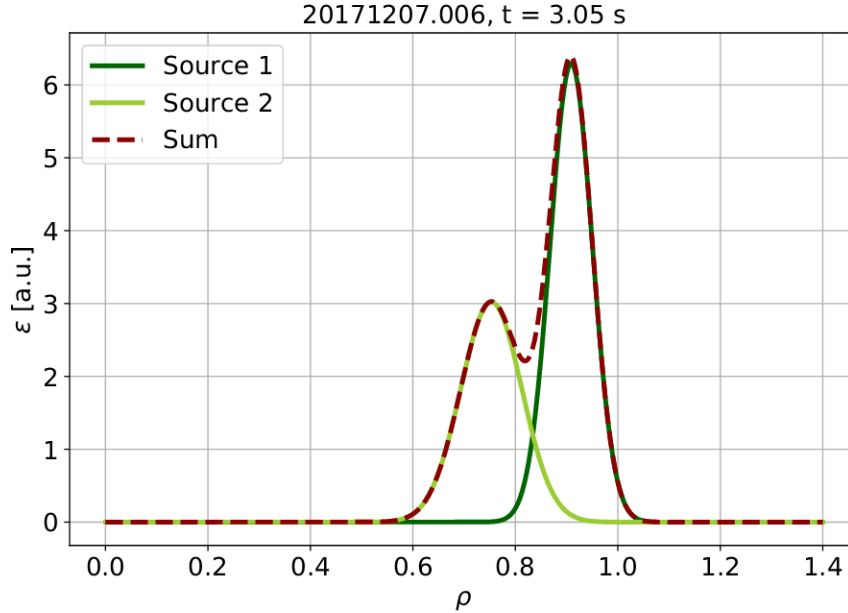


**Figure 2.11.:** Fitted profile of the  $C^{5+}$  emission intensity as a function of  $\rho$  at  $t = 2.7$  s of discharge 20171207.006. The light and dark green curves are the two Gaussian that summed up construct the full emission intensity in dark red.

the two Gaussian corresponding to the two sources of  $C^{5+}$  are shown in light and dark green in Figure 2.10. It is clearly visible that the two mentioned apexes are connected to the two separate Gaussian and thus, could be originating from the  $C^{5+}$  and the neutral population accordingly. To identify if the peaks correspond to the two separate emission processes, the fitted emission intensity profile is further inspected. Figure 2.11 shows this profile from the example time point.

The radial position and full width at half maximum (FWHM) of both peaks remained mostly unchanged during the discharge. The time evolution of these parameters of the separate peaks can be seen in Figure 2.12a and 2.12c, respectively. Both parameters are slightly shifted in the first 1.2 s of the discharge. This is expected as this is the time range when the plasma is building up before the pellet phase.

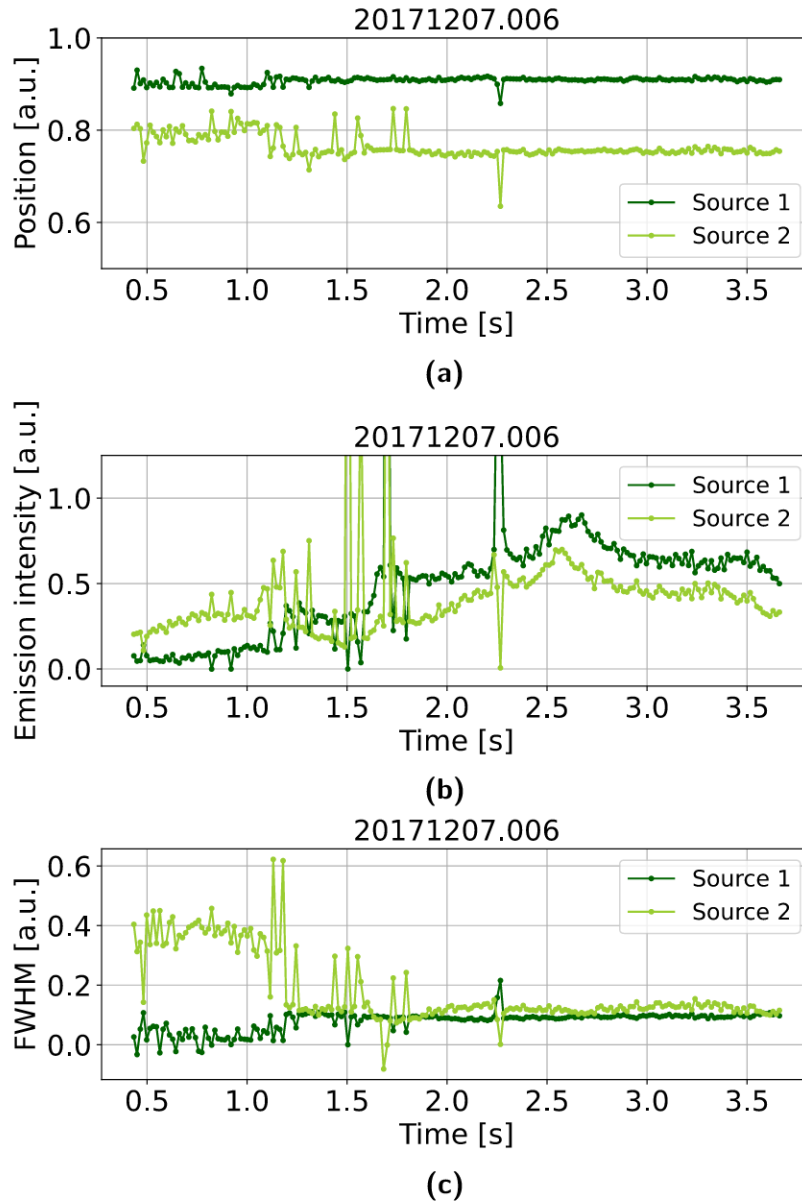


**Figure 2.12.:** Time evolution of the middle position (a), intensity (b) and FWHM (c) of the electron excitation and charge exchange peak as a result of the inversion.

The inner peak's position has outliers during the pellet phase, while the outer peak shows no such behaviour, it is stabilized with minimum noise level already during the pellet phase. Both peaks' position have decreased noise levels in time in the more steady state like post-pellet phase. Both time traces show a distinct outlier value during the magnetic event at  $t = 2.3$  s.

Since the radial location of the two contributions are reasonably distinct, it is a good starting point for their identification. According to the coronal approximation,  $C^{5+}$  ions solely formed by electron excitation are expected to exist at 50 – 150 eV. This corresponds to  $\rho = 0.95$  in the  $T_e$  profile during the stationary phase of the observed discharge. Assuming  $T_i \approx T_e$ , this region is where the electron excitation peak of the  $C^{5+}$  ion is expected. This matches the radial position of the outer peak. This would mean that the inner emission intensity peak is coming from charge exchange with neutrals in the plasma.  $\rho = 0.75$  is marginally inwards from the expected radial distribution of thermal neutrals. However, the lack of measurements on the neutral density profile leaves room for deviation from expectations from theoretical models and experimental results of other relevant machines. The other option also has to be taken into consideration, namely that the outer peak is coming from charge exchange, corresponding to the expected radial distribution of thermal neutrals. In this case the inner emission intensity peak corresponds to electron excitation, having most of the  $C^{5+}$  ions present in the plasma allocated at  $\rho = 0.75$ . At this radial location,  $T_e$  is around 500 eV, which means  $C^{5+}$  ions should be already ionised into  $C^{6+}$ . For  $C^{5+}$  to be carried radially so deeply into the plasma without being ionised further out in the SOL, significantly short transport times are needed. This could be caused by sufficiently high diffusion, as shown later with STRAHL simulations.

The width of the two peaks after the first 1.2 s of the plasma become very similar within  $\approx 20\%$ . No additional conclusion can be drawn solely from the width of the two peaks, as such emission widths are reasonable for both the  $C^{5+}$  and the thermal neutral population.

The third parameter to examine is the intensity of the intensity of the two peaks integrated under the line that can be seen in Figure 2.12b as a function of time. Both time evolutions follow a similar pattern as the time evolution of the line integrated intensity in Figure 2.9. This means that both sources are significantly present throughout the whole discharge. During the pellet phase, both peaks have outliers, although those of the

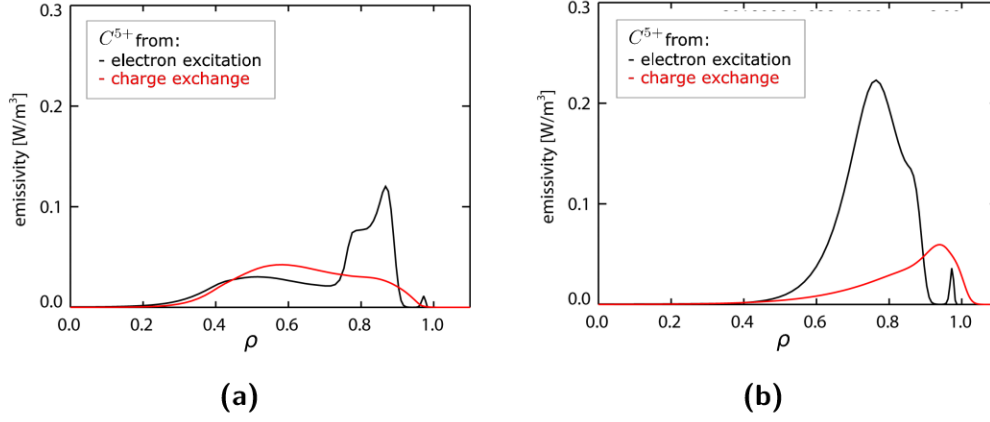


**Figure 2.13.:**  $C^{5+}$  emissivity with electron impact excitation and charge exchange as sources, calculated by the STRAHL impurity transport code for typical ECRH plasma parameters at W7-X. The emissivity was calculated assuming transport dominated by neoclassical effects (a) and assuming high anomalous diffusion (b). Source: [69]

inner peak are of higher intensity. In general, the inner peak's amplitude is around 30 – 50% lower throughout the discharge than that of the outer peak, except during the first 1.2s when the inner peak is around five times higher than the outer peak.

Preliminary radiation calculations with the STRAHL impurity transport code [69] indicate that the inner peak corresponds to the electron impact excitation. The emissivity of the  $C^{5+}$ , shown in Figure 2.13b, was modelled with typical background plasma parameters and included strong anomalous transport. As a comparison, Figure 2.13a shows the same emissivity assuming a neoclassical transport with significantly low anomalous transport. The emissivity, is directly proportional to the previously shown emission intensity that was calculated by inversion, it is scaled to have a physical unit. The radial positions of the two modelled peaks in the STRAHL simulation match the radial position of the emission intensity in Figure 2.11, supporting the validity of the preliminary results. The strong anomalous diffusion, resulting in faster transport, used in the STRAHL calculation could explain how the  $C^{5+}$  ions could be carried inwards to  $\rho \approx 0.7$  without being ionised earlier in the presence of high temperature.

## 2.3. Estimation of the neutral density inside the separatrix

Using the intensity of the charge exchange and electron excitation peak integrated under the line, the neutral density present in the plasma volume can be estimated. This estimation is based on the coronal equilibrium, which is a neoclassical model. However, with the implications of the STRAHL simulation, the carbon transport seems to have a strong anomalous component with high diffusion. This would mean that the neutral density estimation based on a neoclassical model is not reliable in these types of plasmas. The approach is presented nevertheless, as it could be suitable as the base of a more thorough neutral density calculation that takes into account the additional anomalous effects. This could be achieved with the usage of corresponding STRAHL simulations. As the density of thermal neutrals is currently not measured by any diagnostic during at W7-X inside the LCFS, even a rough estimation can be important.

Equation 2.4 shows the emissivity of a spectrum line of the transition from  $j$  to  $i$  ( $\varepsilon_{i \rightarrow j}$ ) built up from three terms, each corresponding to one of the processes leading to the given spectral line according to the collisional radiative model: electron impact excitation (Equation 2.5), recombination (Equation 2.6) and charge exchange (Equation 2.7). Each term consists of: the photon emission coefficient of the specific process ( $PEC^{(exc)}$ ,  $PEC^{(rec)}$ ,  $PEC^{(CX)}$ ), which corresponds to the emission probability of the process (obtained from the OPEN-ADAS database [70]); the number density of the source population ( $n_{\sigma}^{Z+}$  and  $n_{\sigma}^{(Z+1)+}$ ) and the number density of the driving population. The latter is free electrons during electron excitation and recombination ( $n_e$ ) and thermal neutral hydrogen during charge exchange ( $n_H$ ).

$$\varepsilon_{i \rightarrow j} = \varepsilon_{i \rightarrow j}^{exc} + \varepsilon_{i \rightarrow j}^{rec} + \varepsilon_{i \rightarrow j}^{CX} \quad (2.4)$$

$$\varepsilon_{i \rightarrow j}^{exc} = \sum_{\sigma} PEC_{\sigma, i \rightarrow j}^{(exc)} n_e n_{\sigma}^{Z+} \quad (2.5)$$

$$\varepsilon_{i \rightarrow j}^{rec} = \sum_{\rho} PEC_{\rho, i \rightarrow j}^{(rec)} n_e n_{\sigma}^{(Z+1)+} \quad (2.6)$$

$$\varepsilon_{i \rightarrow j}^{CX} = \sum_{\rho} PEC_{\rho, i \rightarrow j}^{(CX)} n_H n_{\sigma}^{(Z+1)+} \quad (2.7)$$

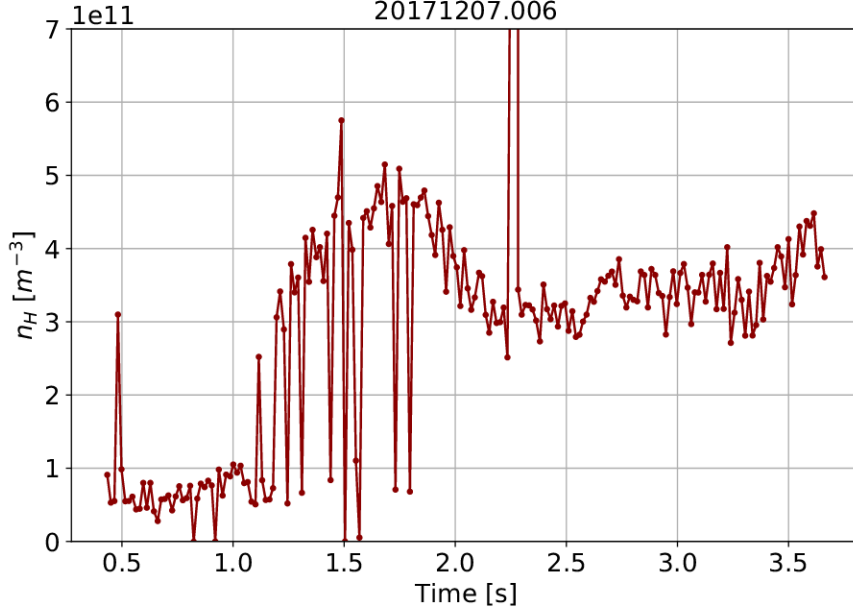


**Figure 2.14.:** Thermal neutral density estimated from the ratio of electron excitation and charge exchange peak in the emission intensity.

In the investigated case of observing  $C^{5+}$  in plasma, the proportion of recombination leading to  $C^{5+}$  is insignificant compared to the proportion of electron excitation and charge exchange. Thus, the recombination term is neglected. The photon emission coefficients are available in the Open-ADAS database. The remaining quantities are  $n_e$  and  $n_{C^{5+}}$ , which the electron excitation peak depends on; and  $n_H$  and  $n_{C^{5+}}$ , which the charge exchange peak depends on. Although these quantities are present in the shown inversion calculation, the model summarised in Equation 2.4 can't be fully resolved in order to calculate the specific quantities, for example the neutral density. This is partly because the variables are inconclusive, and partly because no absolute intensity calibration was done for this inversion and therefore the values of the emission intensity peaks are arbitrary. However, the ratio of the two peaks' intensities can be used to give a rough estimation of the neutral density using the modelling routine CX-Simul [71] that is based on the collisional radiative model. Using the ratio of the intensities eliminates the

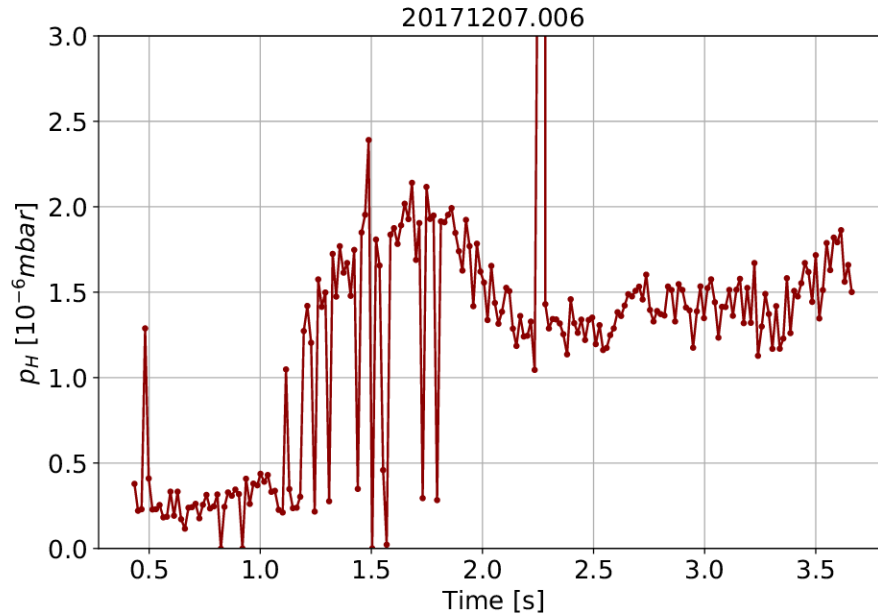


**Figure 2.15.:** Neutral pressure calculated from the estimated neutral density. The pressure level is marginally lower than that measured by the Neutral Pressure Gauges in front of the divertor, as expected.

need for an absolute calibration, as the intensity of the two peaks would use the same calibration. Thus, an estimate of the absolute value of the neutral density is possible despite the lack of an absolute intensity calibration of the measured emission lines. Since the integrated peak intensities of the radial emission intensity profile are needed for this calculation, a radial profile of the neutral density is not possible to obtain via this method, only an average density for each time point. The time evolution of the estimated thermal neutral density is shown in Figure 2.14. According to the observations made on the emission intensity peaks, it is assumed for this estimation that the inner peak corresponds to charge exchange and the outer peak corresponds to electron excitation.

For comparison, the neutral pressure measured by the Neutral Pressure Gauges is used. This neutral pressure is measured at the divertor or close to the divertor, always outside of the LCFS, which is expected to be higher

### 2.3. Estimation of the neutral density inside the separatrix

---

than the neutral pressure inside the LCFS. After an exchange to pressure units from the estimated neutral density, the average neutral pressure during most of the plasma inside the LCFS is  $p_H \approx 1.5 * 10^{-6}$  mbar as seen in Figure 2.15. The neutral pressure measured by the Neutral Pressure Gauges throughout the steady-state like plasma phase is  $p_H \approx 2 - 3 * 10^{-6}$  mbar. The rough estimation made from the  $C^{5+}$  emission intensity profile agrees very well with this. The estimation on thermal neutral pressure at the edge of the confined plasma is of the same order of magnitude but marginally lower than that measured at the divertor targets. This is consistent with the qualitative expectation of thermal neutral density and pressure being higher in the SOL and towards the divertor targets due to lower temperature than in the confined plasma region. With a more thorough method, for instance with included absolute intensity calibration, this estimation can be improved to give a more reliable neutral density for inside of the LCFS.



## Chapter 3.

# Active Spectroscopy

A Charge Exchange Spectroscopy (CXRS) system was set up at Wendelstein 7-X as an active spectroscopy diagnostic. An NBI heating system is running from the operational campaign OP1.2b onwards, which provides the opportunity for this active system, as the neutrals of the NBI are the neutral source for the charge exchange process [72] [73]. From the intersection of the LOSs with the NBI, the CXRS diagnostic is able to give spatially resolved information about impurities in the plasma (as opposed to the Passive Spectroscopy system presented in Chapter 2) along the beam line. The directly measured spatial resolution provides impurity density, temperature and flow velocity profiles from the plasma edge to the plasma core [59]. Currently, this is the only diagnostic at Wendelstein 7-X that is able to measure the low-Z impurity content in the core directly without tomographic inversion or assumptions about the ionisation state balance or transport.

The Active Spectroscopy system consists of several visible wavelength range spectrometers and focuses on low-Z impurities. This work concentrates on the carbon density, obtained from the spectral line measured by the main spectrometer, with the highest etendue. The aim of the analysis is to obtain absolute values of the carbon density along the plasma radius in different plasma scenarios, and to determine the properties of carbon transport using these profiles.

## 3.1. Methods

### 3.1.1. Observation system at W7-X

The detailed description of the CXRS diagnostic system at W7-X can be found in [74]. Elements of the description relevant to this work are presented in the following section.

Five spectrometers were used within the CXRS system during OP1.2b, of which the one able to detect the most light intensity in a given time interval is the so-called ITER-like Spectrometer (*ILS*) with three detecting cameras with fixed wavelength ranges. This is the main spectrometer of the diagnostic and the focus of this analysis. Two other spectrometers, *NIFS* – 1 and *NIFS* – 2 have fixed wavelength ranges, detecting  $H_\alpha$  and  $He^+$  lines respectively, and two further spectrometers, *AUG* – 1 and *AUG* – 2 have variable wavelength ranges which were modified throughout the measurement campaign based on impurities of interest.

The NBI is located in module two of W7-X. Light is collected by 400  $\mu\text{m}$  optical fibres at three ports looking at the beam lines: the *AEA21* port that is located on the left side of the NBI box (counter-clockwise in W7-X; the *AEM21* port that is located above the NBI box; and the *AET21* port that is located on the right side of the NBI (clockwise in W7-X). The diagnostic system was set up with these three viewing angles in order to carry out three dimensional flow velocity measurements based on the observed Doppler shift of the measured spectral line from the different angles [75]. The location of the three ports as well as their LOSs in relation to the two operating NBI beam lines, *S7* and *S8* are shown in Figure 3.1 with the carbon divertor and wall tiles displayed in the background.

The light collecting optical fibres in each port are arranged in an optical head at the inside of the port, near the plasma. They are set behind lenses so that the beam lines are imaged onto the fibres. The intersection of the LOSs and the beam lines provide the spatial points of the carbon profiles later in the analysis. Figure 3.2 shows the LOS layout of each port as they are located within the plasma cross section, with flux surfaces from the standard equilibrium plasma. Each point represents the intersection of a LOS and one or both beams. The *AEA21* optical fibres are arranged in two main lines, *AEA21* – *A* and *AEA21* – *B* with 40 LOSs each, looking through the centre of the neutral beams. There are two secondary lines of

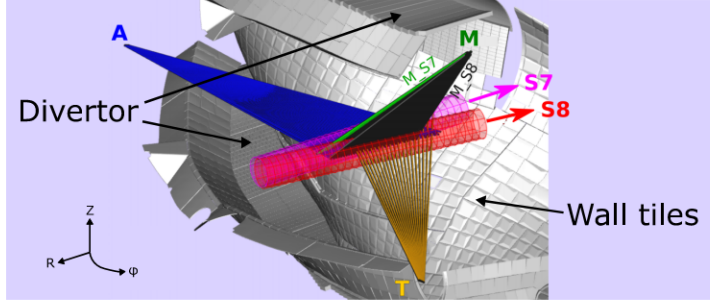


**Figure 3.1.:** The LOSs of the three viewing ports of the CXRS system, *AEA21* (toroidal, blue), *AEM21* (partially poloidal, green and grey) and *AET21* (yellow), in relation to the two operating neutral beams, *S7* (pink) and *S8* (red). The carbon divertor and wall tiles are displayed in the background. Source: [74] Fig. 1. (a)

spatial points, *AEA21* – *X1* and *AEA21* – *X2* with 6 LOSs each that collect radiation from the flux surfaces near the core and the edge, looking across the beam line. All LOSs of the *AEA21* system look through both beams at the same time with a toroidal view. The *AEA21* LOSs have a resolution of 1 – 3 cm. The LOSs of the *AEM21* system are arranged similarly with the difference that one main line of optical fibres (*AEM21* – *S7*) is set to look through the centre of only the *S7* beam, the other main line (*AEM21* – *S8*) is set to look through the centre of only the *S8* beam. Both have 54 LOSs. The optical fibres of *AEM21* – *X1* with 8 LOSs and *AEM21* – *X2* with 9 LOSs look through either or both of the beams depending on their location. This port is located above the beam lines in a  $45^\circ$  angle, thus providing a partially poloidal view on the observed impurities. Its LOS array has a 2 – 8 cm resolution. These are the two main ports of the active spectroscopy system. The *AET21* system consists of only one line of fibres with 20 LOSs that look through both beams, but not entirely through their centre. These fibres were barely used during OP1.2b, due to the fact that the *AET21* system has a resolution of only 10 – 14 cm making it less favourable for the analysis presented here.

The optical head is located at the end of each port’s immersion tube where a fused silica window is placed to separate the optical head from the vacuum. The collected radiation is reflected by a mirror towards the vacuum window, through which it reaches the optical head. The optical fibres are

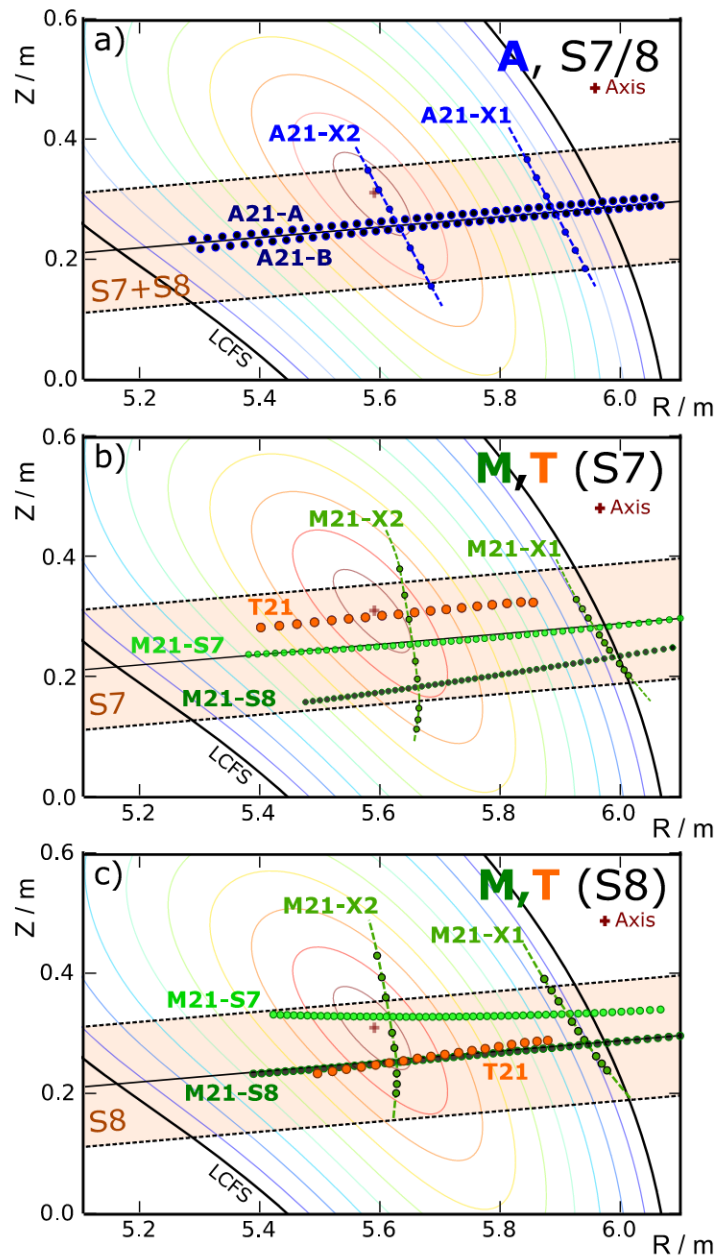


**Figure 3.2.:** Intersection points of each LOS of the CXRS system with the neutral beams displayed over standard equilibrium flux surfaces shown in relation to the two neutral beams,  $S7$  and  $S8$ . A red cross indicates the magnetic axis in the centre of the cross section. Source: [74] Fig. 2.

then led through the immersion tube, exit at the entrance of the port and led to the laboratory from all three ports. There they are connected to a patch panel, that has a set of optical fibres connected to it on the other side, which lead to the spectrometers. The optical fibres of the spectrometers are referred to as channels, and each channel corresponds to a LOS. The channels of the five spectrometers were distributed among the LOSs of the ports so that every spectrometer has a coverage of all LOS arrays in the two main viewing systems.

The spectrometers *AUG-1* and *AUG-2* have a simple lens spectrometer structure. After entering through the entrance slit, a lens directs the light onto the grating, after which an other lens focuses the wavelength-split rays towards the detecting camera. Both spectrometers have 45 channels. During OP1.2b, both were mainly targeted to measure the intensity of secondary impurities, such as  $B^{4+}$  at 494.46 nm from the transition  $n = 7 \rightarrow 6$ ,  $O^{7+}$  at 606.8 nm from the transition  $n = 10 \rightarrow 9$ ,  $N^{6+}$  at 566.94 nm from the transition  $n = 9 \rightarrow 8$  and  $Ar^{15+}$  at 436.52 nm from the transition  $n = 14 \rightarrow 13$ . Occasionally they were set to look at spectral lines of the main impurity (carbon) and the two possible main plasma species (hydrogen and helium), which were covered by the *ILS*. Having the *AUG-1* and *AUG-2* measure these spectral lines additionally allowed for much higher spatial resolution profiles for specific plasma discharges, such as plasmas with higher performance.

The *ILS* is a high etendue spectrometer that was originally built as a prototype for the ITER tokamak [76], and was later used as part of the CXRS system at the ASDEX Upgrade tokamak [78] [77]. Its parameters are listed in Table 3.1. Its high etendue allows for more light to enter the spectrometer and be collected by the detecting cameras in a given time compared to typical spectrometers, e. g. the variable wavelength *AUG-1* and *AUG-2*, which provides possibility for higher time resolution with sufficient signal to noise ratio. It has three detecting systems, a CMOS camera that measures the  $C^{5+}$  line at 529.06 nm, a CMOS camera detecting the  $H^\alpha$  line at 656.028 nm, and a CCD camera measuring the  $He^+$  line at 468.58 nm from the transition  $n = 4 \rightarrow 3$ . This analysis obtains the carbon density profiles from the  $C^{5+}$  camera while using the intensities measured by the  $H^\alpha$  camera as well. The data measured by the  $He^+$  camera was not analysed in this work. The *ILS* has 54 channels, with 3 of them not connected to the plasma so that they can be used for calibration. The typical exposure time of the  $C^{5+}$  and the

**Table 3.1.:** Parameters of the ITER-like Spectrometer (*ILS*) spectrometer as were used for the Active Spectroscopy system during OP1.2b. [76] [77]

<b>Focal length</b>	$\approx 1$ m
<b>F number</b>	2.3
<b>Slit width of <math>H^\alpha</math> detector</b>	400 $\mu\text{m}$
<b>Slit width of <math>C^{5+}</math> detector</b>	600 $\mu\text{m}$
<b>Slit width of <math>He^+</math> detector</b>	500 $\mu\text{m}$
<b>Slit width equivalent at fibre of <math>H^\alpha</math> detector</b>	65 $\mu\text{m}$
<b>Slit width equivalent at fibre of <math>C^{5+}</math> detector</b>	100 $\mu\text{m}$
<b>Slit width equivalent at fibre of <math>He^+</math> detector</b>	75 $\mu\text{m}$
<b>Resolution of <math>H^\alpha</math> detector</b>	0.1 nm
<b>Resolution of <math>C^{5+}</math> detector</b>	0.1 nm
<b>Resolution of <math>He^+</math> detector</b>	0.07 nm
<b>Grating</b>	500 lines / mm
<b>Grating area</b>	$\approx 92$ mm $\times$ 200 mm
<b>Grating order of <math>H^\alpha</math> detector</b>	5 <sup>th</sup>
<b>Grating order of <math>C^{5+}</math> detector</b>	6 <sup>th</sup>
<b>Grating order of <math>He^+</math> detector</b>	7 <sup>th</sup>

$H^\alpha$  camera throughout the measurement campaign was 7.5 ms and 16 ms, respectively. With shorter exposure times, the signal to noise ratio in the measured spectra is higher, therefore the values were chosen to optimise between a good time resolution and acceptable signal to noise ratio.

The optical layout of the spectrometer can be seen in Figure 3.3. It is built in a way that the light is separated within the spectrometer into three wavelength ranges corresponding to the three measured spectral lines. This allows a unique analysis opportunity, as the LOSs, and thus the origin location of the radiation in the plasma, is the same for all three detected

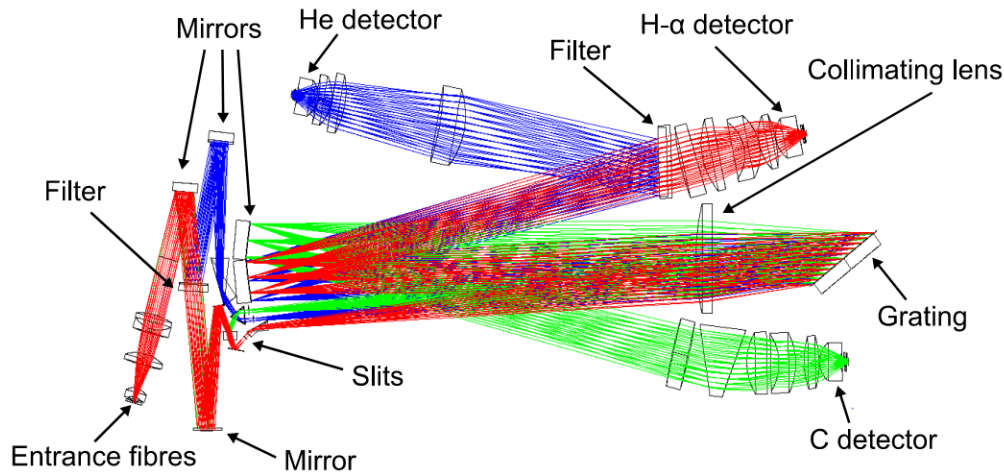


**Figure 3.3.:** Schematic structure of the *ILS* showing how the light rays are directed and then filtered within the spectrometer. The green, red and blue light rays refer to radiation from the wavelength range around the  $C^{5+}$  line at 529.06 nm, the  $H^{\alpha}$  line at 656.028 nm and the  $He^{+}$  line at 468.58 nm, respectively. Source: [76] Fig. 1.

impurities. In Figure 3.3, the green, red and blue light rays refer to the  $C^{5+}$ ,  $H^{\alpha}$  and  $He^{+}$  wavelength ranges, respectively. After entering the spectrometer, the light goes through a series of focusing lenses and mirrors. The first filter separates the blue radiation from the green and red, then both lead through another series of mirrors and lenses to be then lead through the slits after being separated. Afterwards, all three types of light rays go through the collimating lens and are refracted with distinct angles by the grating. Finally, they are reflected by 2 mirrors to be aimed at the cameras via a final set of focusing lenses. The refracting angle of the  $H^{\alpha}$  and the  $He^{+}$  radiation are so close to each other that one common mirror is used to direct both of them towards the  $H^{\alpha}$  camera. In front of the camera, a red interference filter is used that lets the  $H^{\alpha}$  radiation through, and reflects the  $He^{+}$  radiation towards its corresponding camera. The  $C^{5+}$  radiation is directly reflected by a mirror after after the grating to its detecting camera. The 2D images depicted by the three cameras have the same structure as those measured by the Passive Spectroscopy system, as seen in Figure

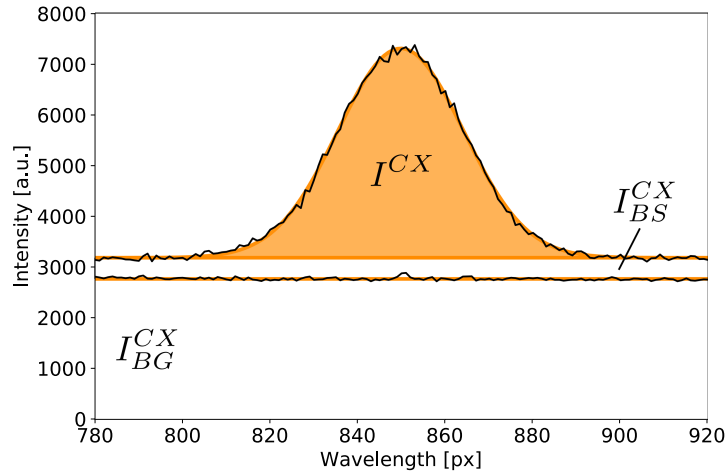


**Figure 3.4.:** Spectrum measured by the  $ILS\ C^{5+}$  camera in black with the no-plasma background level displayed below it. The difference is the bremsstrahlung level. Both underlying backgrounds are subtracted before further processing.

2.3. The horizontal axis is the wavelength, the vertical axis represents the different LOSs.

### 3.1.2. Processing the measured spectra

An example spectrum measured by the  $C^{5+}$  camera is shown in Figure 3.4. The units of spectrum are the same as for the spectra measured by the Passive Spectroscopy system as described in Section 2.1.2 with the dimension  $N_{\gamma}\ \text{sr}^{-1}\ \text{m}^{-2}\ \text{nm}^{-1}\ \text{s}^{-1}$ . The bremsstrahlung and the no-plasma background were subtracted from the spectra, they are both displayed in Figure 3.4.

The remaining  $C^{5+}$  spectral line consists of two components, a so-called active and a passive part. The passive component is what the spectral line would look like without the additional neutral source of the NBI. This is directly measured during frames when the NBI is turned off and is exactly the same radiation that the Passive Spectroscopy system detects. The active component is the additional intensity that appears when the NBI is turned on. The neutrals of the NBI transfer an electron to fully-stripped  $C^{6+}$  ions via charge exchange, as shown in Equation 3.1, and the radiation of these

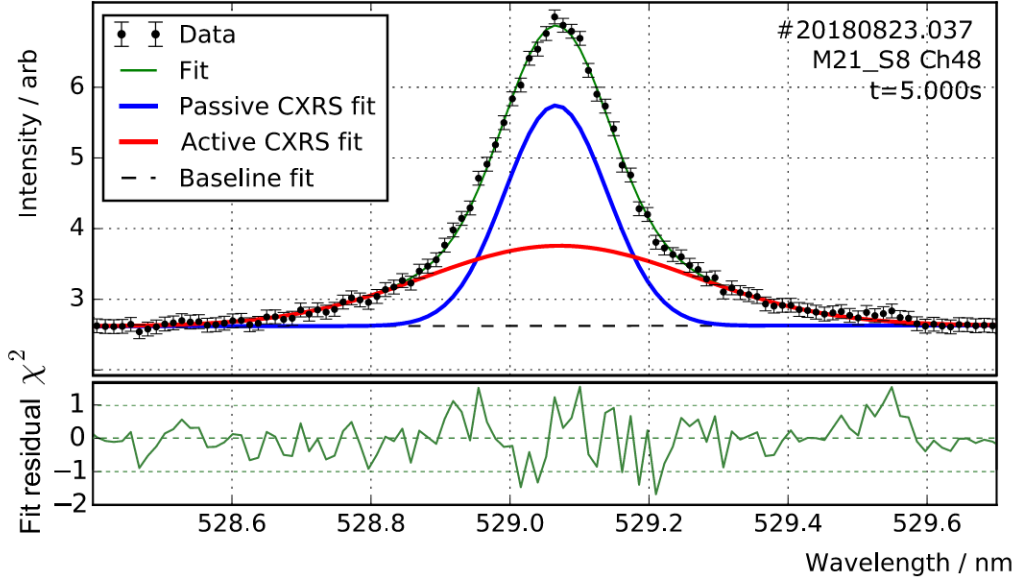
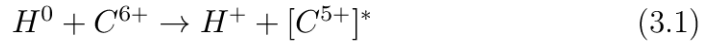


**Figure 3.5.:** Separation of the active (red) and passive (blue) component of an example measured  $C^{5+}$  spectra (black dots). Both components are fitted with a Gaussian, with their addition (green, upper plot) matching the measurement. The lower plot (green) shows the difference of the measured data (points and error bars, top plot). Source: [74] Fig. 7. (a)

new  $C^{5+}$  ions is the source of the additional intensity.



For spatially resolved carbon analysis, the active component is needed, since that is the only part of the spectrum that is spatially localised and not line integrated, due to the radiation originating from the intersection of the LOSs and the neutral beam. Therefore, a proper separation of the active and the passive component of the spectrum is needed for all NBI time points. Both components are fitted by a Gaussian, and their intensity is the area under their respective Gaussian. An example separation of the two components is shown in Figure 3.5. This example is taken from the plasma core, where the temperature of the active component is considerably higher than that of the edge-dominated passive component, hence the active component is wider than the passive.

The measured  $C^{5+}$  passive intensity immediately after the NBI operation is noticeably higher than in the passive spectra before the NBI is turned on. This means that the both components are changing while the NBI is operating and none of them are measured independently in this phase, which makes the separation of the two components not straightforward. The life time of the measured excited  $C^{5+}(n = 8)$  ions is  $\sim 10^{-8}$  s, which is negligible compared to the exposure time of the camera. This means that from the measurement point of view, the  $C^{5+}(n = 8)$  ions that were created via charge exchange from NBI neutrals are measured immediately after the NBI is turned on and disappear from the measured spectrum as soon as the NBI is turned off. There could be  $C^{5+}(n < 8)$  ions that get re-excited later, to become  $C^{5+}(n = 8)$  and be measured again, but the life time of these ions is also of a similar order of magnitude. Thus, the increase of the passive signal is not originating from  $C^{5+}$  ions that were created by NBI neutrals. The origin of the increase of the passive signal is unclear. It could be due to changes in the background plasma caused by the NBI or because more carbon is released from the wall while the NBI is turned on.

To account for the increase in the passive component, that is not measured directly, and to make sure that the component separation is realistic, two methods were used depending on the length of the given NBI operation. First, a double Gaussian (one Gaussian for each component) was fitted to the measured spectra in the plasma core, as seen in Figure 3.5, in cases where the separation of the two Gaussian is clearer due to the temperature difference of the two components. The time evolution of the intensity of the resulting two fitted Gaussian is shown in Figure 3.6. This shows gradually increasing passive intensity during NBI operation that decreases marginally when the NBI switches off to levels that are higher than the passive intensity measured before the NBI. This additional increase appears after  $\approx 30$  ms of NBI operation. Thus, for NBI blips with a length  $< 30$  ms, the passive component is estimated by interpolating the spectra immediately before and after the NBI blip consisting only the passive component. The last frames before the NBI is turned on, as well as the first frames after the NBI is turned off, are averaged into a "before" and an "after" passive frame. Averaging is needed to reduce noise. Then a linear interpolation is done between the "before" and the "after" passive frame. This estimated passive spectrum is directly subtracted from the measured spectrum for every NBI frame. For NBI pulses with a length  $> 30$  ms, this subtraction method is

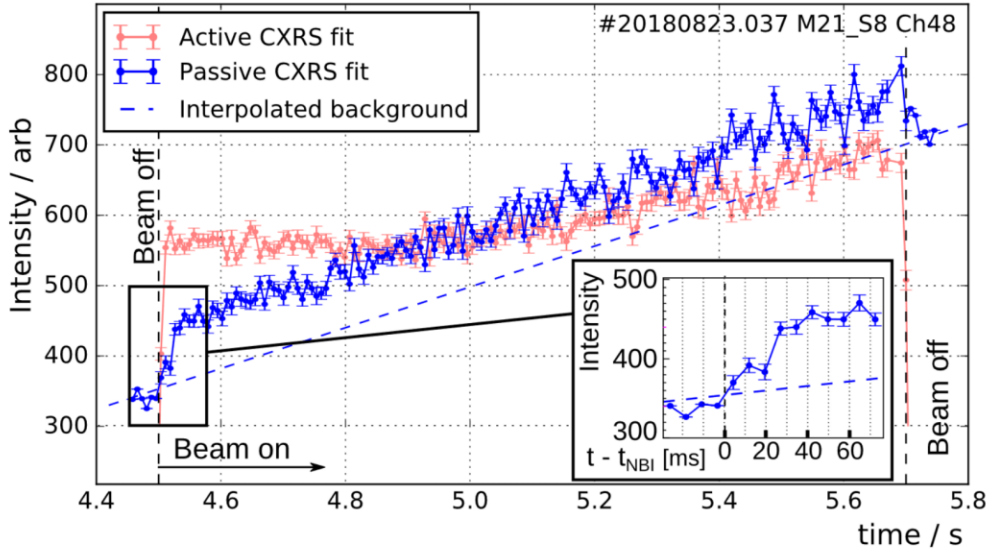


**Figure 3.6.:** Time trace of the fitted active (solid red) and passive (solid blue) component in relation to the linear interpolation of the passive component between the measured passive frames before and after the NBI operation (dashed blue). Source: [74] Fig. 7. (b)

inaccurate due to the increased level of the passive component as seen in the core fit. The level of this increase depends on the background plasma parameters and is not trivial to simulate. Additionally, there are plasma scenarios when the plasma parameters are changing strongly enough so that the time evolution of the increased passive intensity can deviate heavily from linear. Scenarios like this are for instance plasmas with NBI operation but without ECRH operation, plasmas with series of pellet injections or plasmas with injection of impurities. In these cases, a careful dual Gaussian fit is done for all channels. This becomes less well defined in plasma regions where the temperature of the active and passive components are similar, as is the case towards the plasma edge. This is why the earlier described subtraction method is more reliable and is used for plasmas with short NBI blips.

Figure 3.7 shows an example spectrum measured by the  $H_\alpha$  camera without NBI operation in grey and during NBI operation in black. When the NBI is turned off, the measured  $H_\alpha$  intensity comes from the main

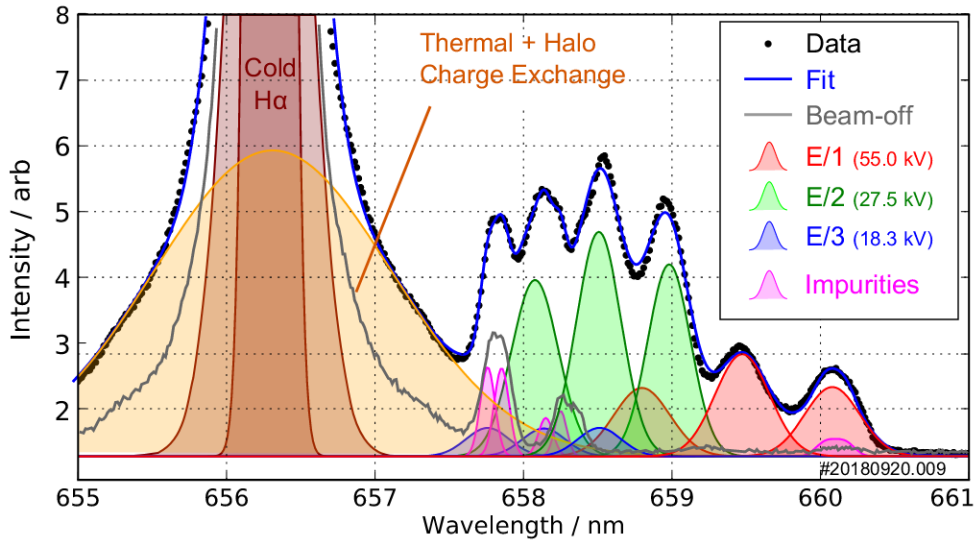


**Figure 3.7.:** Example measured  $H_\alpha$  spectrum (black dots) and its fitted components during NBI operation: cold  $H_\alpha$  (brown); 1st (red), 2nd (green) and 3rd (blue) energy components; halo (yellow); and nearby impurity lines (pink). The result of adding up the fits of all components (blue line) matches the measured spectrum sufficiently. Additionally, the  $H_\alpha$  spectrum measured when the NBI is turned off is displayed in grey. Source: [74] Fig. 10. (a)

$H^0$  population of the plasma getting excited by collisions. Most  $H^0$  atoms are located in front of the divertor. Their radiation is referred to as "cold  $H_\alpha$ ", because temperature is  $\approx 1 - 2$  eV at the divertor, much colder than in the confined plasma, which causes the thin spectral line without NBI operation. Additionally, there are a few impurities that have a spectral line in the measured vicinity of the  $H_\alpha$  spectrum, such as two  $C^{3+}$  lines. These are displayed in pink in Figure 3.7. When the NBI is turned on, several additional components of the  $H_\alpha$  spectrum appear due to the fact that the NBI consists of hydrogen atoms.

To create the neutral hydrogen beam, three different kinds of hydrogen molecules are ionised then accelerated by a unified acceleration energy. The three kinds are  $H^+$ ,  $H_2^+$  and  $H_3^+$ . After acceleration,  $H_2^+$  and  $H_3^+$  molecules are broken down into single hydrogen particles, with the unified acceleration

energy being divided between these single hydrogen ions. Once neutralized, the beam consists of neutral hydrogen atoms of three different energies, from full, half or third of the original acceleration voltage. These three hydrogen populations are referred to as 1st, 2nd and 3rd energy components in the following. As the beam penetrates the plasma, the radiation of the excited neutral hydrogen atoms will appear in the measured spectra. As there are three different energies and thus, three different velocities present in the additional  $H^0$  population, the spectral line of the three energy components have different Doppler shifts compared to the cold  $H^0$  line. Additionally, the spectral line of each energy component is split into 3 separate lines due to Motional Stark Effect. The middle line is referred to as  $\sigma$ , the two side lines are referred to as  $\pi^+$  and  $\pi^-$ .

Additionally, the radiation of the halo neutrals re-excited by collisions appears around the main  $H_\alpha$  spectral line, this is displayed in yellow in Figure 3.7.

All components of the  $H_\alpha$  spectrum are fitted by a Gaussian, making the fit of the full spectrum consist 17 Gaussian.

The fitting of both the  $C^{5+}$  and the  $H_\alpha$  spectrum is done after converting the wavelength axis from pixel to nm according to a wavelength calibration. This calibration was done with a Ne lamp as it is described in Section 2.1.2.

### 3.1.3. Calculating carbon density profiles with cross calibration

To calculate carbon density profiles from the intensity of the active component of the  $C^{5+}$  spectral line ( $I^{CX}$ ), the conventional way is to directly convert the intensity values (photon count) into real density values with an absolute intensity calibration and the need for a relatively complex model of the attenuation of the neutral beam at all positions as it passes through the plasma [79] [73]. However, there is another method to obtain absolute carbon densities, without the need for processing an absolute intensity calibration and without the need for using models to calculate the beam density that is not directly measured. This method uses the intensity of the beam energy components ( $I_E^{BES}$ ,  $E = E_0, E_0/2, E_0/3$ ) besides the intensity of the  $C^{5+}$  line [80] [81], and is easily available for the CXRS system at W7-X given that the  $C^{5+}$  and the  $H_\alpha$  cameras share the same LOSs and optical

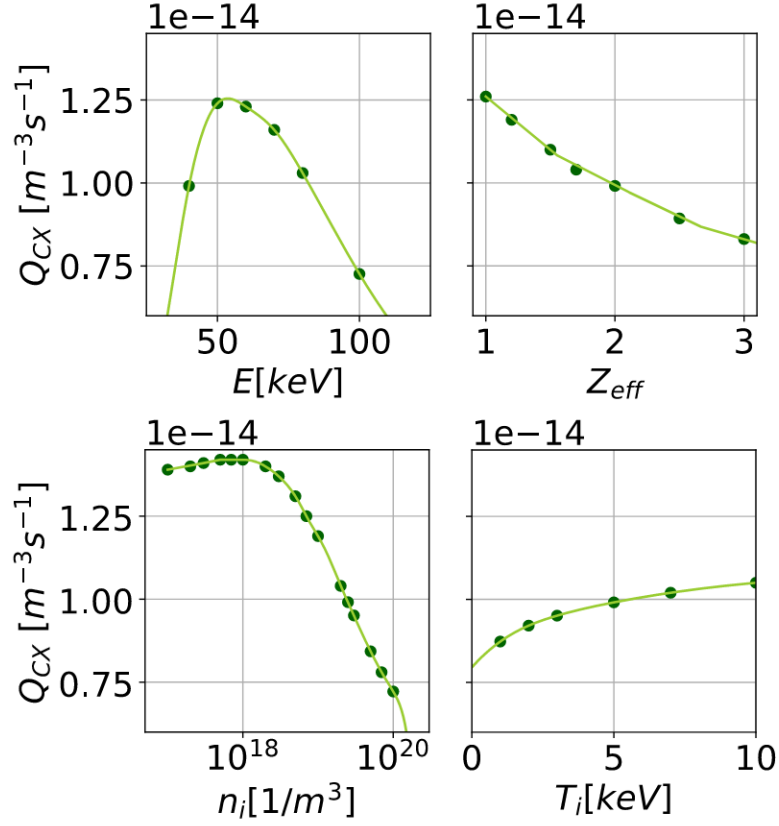


**Figure 3.8.:** Dependencies of the charge exchange emission coefficient ( $Q_{CX}$ ) in relevant plasma parameter ranges based on data from the OPEN-ADAS database [82].  $Q_{CX}$  is shown as a function of the neutral beam energy (upper left),  $Z_{eff}$  (upper right), ion density (lower left) and ion temperature (lower right).

fibres.

The measured  $C^{5+}$  intensity is given by Equation 3.2 and is the sum of the  $C^{5+}$  intensity originating from charge exchange with each of the three beam energy components. These are proportional to the density of the beam energy component ( $n_E^{beam}$ ), the charge exchange emission coefficient at the given energy ( $Q_E^{CX}$ ) and the density of the  $C^{6+}$  ion ( $n_C$ ), integrated over the intersection volume between the beam and the given LOS. The charge exchange emission coefficient describes the probability of the  $C^{6+} + H^0 \rightarrow$

$C^{5+*} + H^+$  reaction to the specific  $C^{5+}$  level. It relates the population of  $C^{5+*}$  to the population of  $C^{6+}$  and  $H^0$  at the given ion temperature ( $T_i$ ), ion density ( $n_i$ ), beam energy ( $E$ ) and  $Z_{Eff}$ , and is calculated according to a collisional-radiative model. Figure 3.8 shows the changes of  $Q_E^{CX}$  in the W7-X relevant parameter range. The charge exchange emission coefficients were obtained from the OPEN-ADAS database [82] for the investigated plasma configurations.

$$I^{CX} = \sum_{E=E_0, E_0/2, E_0/3} I_E^{CX} = \int_{LOS} n_C(l) \sum_{E=E_0, E_0/2, E_0/3} Q_E^{CX}(l) n_E^{beam}(l) dl \quad (3.2)$$

The measured intensity of a given beam energy component is given by Equation 3.3 and is proportional to the background plasma electron density ( $n_e$ ), the density of the beam energy component ( $n_E^{beam}$ ) and the beam emission coefficient ( $Q_E^{BES}$ ), integrated over the intersection of the beam and the given LOS. The beam emission coefficient describes the excitation of the beam neutrals by collisions with electrons at a given beam energy, ion temperature and ion density. These coefficients were obtained from the OPEN-ADAS database [83] for the investigated plasma configurations.

$$I_E^{BES} = \int_{LOS} n_e(l) Q_E^{BES}(l) n_E^{beam}(l) dl \quad (3.3)$$

It is assumed that the plasma parameters  $n_C$ ,  $n_e$ ,  $T_e$ ,  $T_i$  etc. and hence  $Q_{CX}$  and  $Q_{BES}$ , do not change along a given LOS within the intersection volume with the beam. This assumption is realistic for most of the LOSs except the for the channels of the *AEM21* system close to the plasma core. These channels look almost directly through the central flux surfaces, and detect light from more flux surfaces within the intersection volume of the measured light, meaning more significant changes of the plasma parameters along the LOS. Channels that do not look directly through the core, cross a small range of flux surfaces. In these cases, it can be assumed that plasma parameters, including  $n_C$  and  $n_e$ , do not change significantly along the LOS within the intersection volume, and therefore they do not depend strongly on  $l$ . This means that their average value weighted by the beam density integrated over the intersection between the given LOS and the beam, shown

by Equation 3.4 and 3.5, can be approximated by the carbon and electron density at the intersection, respectively.

$$\langle n_C \rangle = \frac{\int_{LOS} n_C(l) n_{beam}^E(l) dl}{\int_{LOS} n_{beam}^E(l) dl} \equiv n_C(\langle r \rangle) \quad (3.4)$$

$$\langle n_e \rangle = \frac{\int_{LOS} n_e(l) n_{beam}^E(l) dl}{\int_{LOS} n_{beam}^E(l) dl} \equiv n_e(\langle r \rangle) \quad (3.5)$$

Under this assumption, and similarly assuming that the effective rate coefficients  $Q_{CX}$  and  $Q_{BES}$  do not change significantly within the intersection volume, these parameters can be taken outside the integral, shown on Equation 3.6 and 3.7.

$$I^{CX} = \sum_{E=E_0, E_0/2, E_0/3} n_C Q_E^{CX} \int_{LOS} n_E^{beam}(l) dl \quad (3.6)$$

$$I_E^{BES} = n_e Q_E^{BES} \int_{LOS} n_E^{beam}(l) dl \quad (3.7)$$

As the  $C^{5+}$  and the  $H_\alpha$  cameras have the same LOSs, the determination of the intersection integral between the NBI and the LOSs can be eliminated. From Equation 3.7, the integral density of a given beam energy component (Equation 3.8) can be substituted into Equation 3.6, resulting in Equation 3.9.

$$\int_{LOS} n_E^{beam}(l) dl = \frac{I_E^{BES}}{n_e Q_E^{BES}} \quad (3.8)$$

$$I^{CX} = \sum_{E=E_0, E_0/2, E_0/3} \frac{I_E^{BES} Q_E^{CX} n_C}{n_e Q_E^{BES}} = \frac{n_C}{n_e} \sum_{E=E_0, E_0/2, E_0/3} \frac{I_E^{BES} Q_E^{CX}}{Q_E^{BES}} \quad (3.9)$$

From Equation 3.9, the fraction of the carbon density and the electron density is derived:

$$\frac{n_C}{n_e} = \frac{I^{CX}}{\sum_{E=E_0, E_0/2, E_0/3} \frac{I_E^{BES} Q_E^{CX}}{Q_E^{BES}}} \quad (3.10)$$

The carbon density is derived by multiplying this fraction with the electron density. Here, the electron density measured by the Thomson Scattering system is used. The resulting density is the  $C^{6+}$  density and will be referred to as carbon density in the following, as the vast majority of the total carbon population in the confined plasma (for approximately  $\rho < 0.8$ ) is fully stripped, due to the high temperature.

In some particular cases, like comparing the carbon content of W7-X to that of other fusion devices, it is beneficial to investigate carbon concentration instead of carbon density profiles. The concentration is defined to describe the ratio of carbon and all the fully stripped ions present in the plasma. To calculate the carbon concentration from the fraction of the carbon and electron density, it is assumed that carbon is the only impurity present in the plasma. The electron density can be written as an addition of all electrons that were stripped from the different fully-stripped ions (hydrogen and carbon ion in the presented case) present in the plasma, as shown in Equation 3.11.  $n_H$  is the density of the main hydrogen ions,  $n_C$  is the carbon density and  $Z_C$  is the atomic number of carbon.

$$n_e = n_H + n_C Z_C \rightarrow n_H = n_e - n_C Z_C \quad (3.11)$$

The definition of carbon concentration ( $C_C$ ) is shown in Equation 3.12. Deriving  $n_H$  from Equation 3.11 and constituting it into the concentration definition allows to express the concentration with the fraction of  $n_C$  and  $n_e$  as the only variable.

$$\begin{aligned} C_C &= \frac{n_C}{n_H + n_C} = \frac{n_C}{n_e - n_C Z_C + n_C} = \\ &= \frac{n_C}{n_e + n_C(1 - Z_C)} = \frac{n_C}{n_e} \frac{1}{1 + \frac{n_C}{n_e}(1 - Z_C)} \end{aligned} \quad (3.12)$$

Apart from sharing the same LOSs and optical fibres, the  $C^{5+}$  and the  $H_\alpha$  cameras naturally have a different sensitivity due to their photon to electron conversion, their dispersion, as well as sensitivities and other characteristics of the optics after the wavelength separation of the detected radiation. Because of the different sensitivities of the cameras, their signal and their bremsstrahlung level differ from each other. Their no-plasma background

also differs as the noise coming from the camera itself is different. Additionally, their individual settings were chosen to match the requirements of the given spectral line. They have independent binning (process to separate the signal of individual channels from each other), exposure time and other observational settings. These differences would need to be addressed and taken into account, if the absolute carbon density would be obtained through absolute intensity calibration. For the previously introduced method, using the measured intensity of the beam energy components, a cross calibration is possible that eliminates all differences between the measured ( $I_m^{CX}$  and  $I_{E,m}^{BES}$ ) and theoretical absolute intensities ( $I^{CX}$  and  $I_E^{BES}$ ). This is needed to acquire absolute carbon densities. The absolute intensities of  $C^{5+}$  and  $H_\alpha$  can be written as the product of the corresponding measured intensities and the sensitivities of the respective cameras ( $\eta_{CX}$  and  $\eta_{BES}$ ) as shown in Equation 3.13 and 3.14.

$$I^{CX} = \eta_{CX} I_m^{CX} \quad (3.13)$$

$$I_E^{BES} = \eta_{BES} I_{E,m}^{BES} \quad (3.14)$$

$\eta$  includes all parameters that would affect the sensitivity of the measurement by the given camera. Taking it into account, Equation 3.10 is changed to Equation 3.15.

$$\frac{n_C}{n_e} = \frac{\eta_{CX} I_m^{CX}}{\sum_{E=E_0, E_0/2, E_0/3} \frac{\eta_{BES} I_E^{BES} Q_E^{CX}}{Q_E^{BES}}} \quad (3.15)$$

The bremsstrahlung light measured by the two cameras is used for quantifying  $\eta$ , as its value depends on all the above mentioned characteristics and settings of the given camera. The bremsstrahlung level cannot be obtained from the exact wavelength of the spectral line, as the line itself obstructs this region, therefore it is taken from the edge of the measured spectra where there are no spectral lines. The wavelength difference from the position of the line to the wavelength range where the bremsstrahlung level is taken from is  $\approx 5nm$  for both the  $C^{5+}$  and the  $H_\alpha$  cameras. The bremsstrahlung level changes with  $1/\lambda^2$  within the given wavelength ranges, which means the change in bremsstrahlung is  $\approx 2\%$  across the wavelength

range of each measured spectrum. Based on this, the bremsstrahlung background is assumed to be flat within the spectral range of each camera. The exact bremsstrahlung value for a given channel in a given time point is taken by averaging  $\approx 10 - 30$  points from the chosen wavelength range near the observed spectral line in the raw spectrum to eliminate the noisiness of the signal. The theoretical acquired bremsstrahlung background of the  $C^{5+}$  and the  $H_\alpha$  cameras is shown in Equation 3.16 and 3.17, respectively.

$$B^{CX} = \frac{dI_{BS}^{CX}}{dl} \quad (3.16)$$

$$B^{BES} = \frac{dI_{BS}^{BES}}{dl} \quad (3.17)$$

$I_{BS}^{CX}$  and  $I_{BS}^{BES}$  are the respective bremsstrahlung intensities that are integrated over the wavelength ( $l$ ). Both theoretical bremsstrahlung levels ( $B^{CX}$  and  $B^{BES}$ ) can be expressed with the corresponding empirical levels ( $B_m^{CX}$  and  $B_m^{BES}$ ) and the sensitivity of the cameras, as shown in Equation 3.18 and 3.19, respectively.

$$B^{CX} = \eta_{CX} B_m^{CX} \quad (3.18)$$

$$B_E^{BES} = \eta_{BES} B_m^{BES} \quad (3.19)$$

For further clarity, Table 3.2 lists the dimension of the theoretical and empirical line intensities and bremsstrahlung levels.

The bremsstrahlung level itself depends on wavelength, so the cross calibration is done using the Equation 3.20.  $\lambda^{CX}$  and  $\lambda^{BES}$  are the wavelength of the two measured spectral lines.

$$\frac{B^{CX}}{B^{BES}} = \frac{\lambda^{BES}}{\lambda^{CX}} \quad (3.20)$$

To eliminate  $\eta_{CX}$  and  $\eta_{BES}$  from Equation 3.15, the calculation goes as the following, using the Bremsstrahlung background of both cameras:

$$\frac{\eta_{CX}}{\eta_{BES}} = \frac{B^{CX} B_m^{BES}}{B_m^{CX} B^{BES}} = \frac{B^{CX}}{B^{BES}} \frac{B_m^{BES}}{B_m^{CX}} = \frac{\lambda^{BES}}{\lambda^{CX}} \frac{B_m^{BES}}{B_m^{CX}} \quad (3.21)$$

**Table 3.2.:** Dimension of the theoretical and measured intensity of the  $C^{5+}$  ion ( $I^{CX}$  and  $I_m^{CX}$ ) and the beam energy components ( $I_E^{BES}$  and  $I_{E,m}^{BES}$ ), as well as the dimension of the bremsstrahlung background, theoretical and measured by the  $C^{5+}$  camera ( $B^{CX}$  and  $B_m^{CX}$ ) and the  $H_\alpha$  camera ( $B^{BES}$  and  $B_m^{BES}$ ). The dimension of the dispersion of the two cameras ( $\omega^{CX}$  and  $\omega^{BES}$ ) is also displayed.  $\gamma$  refers to the number of photons emitted, while  $e^-$  refers to the photoelectron count recorded by the cameras.  $t_{frame}^{CX}$  and  $t_{frame}^{BES}$  refer to the time length of one frame of the respective cameras.

$I^{CX}$	$\gamma \text{ m}^{-2} \text{ sr}^{-1} \text{ s}^{-1}$
$I_m^{CX}$	$e^- (t_{frame}^{CX})^{-1}$
$I_E^{BES}$	$\gamma \text{ m}^{-2} \text{ sr}^{-1} \text{ s}^{-1}$
$I_{E,m}^{BES}$	$e^- (t_{frame}^{BES})^{-1}$
$B^{CX}$	$\gamma \text{ m}^{-2} \text{ sr}^{-1} \text{ nm}^{-1} \text{ s}^{-1}$
$B_m^{CX}$	$e^- (t_{frame}^{CX})^{-1} \text{ pixel}_{CX}^{-1}$
$B^{BES}$	$\gamma \text{ m}^{-2} \text{ sr}^{-1} \text{ nm}^{-1} \text{ s}^{-1}$
$B_m^{BES}$	$e^- (t_{frame}^{BES})^{-1} \text{ pixel}_{BES}^{-1}$
$\omega^{CX}$	$\text{pixel}_{CX}^{-1} \text{ nm}$
$\omega^{BES}$	$\text{pixel}_{BES}^{-1} \text{ nm}$

In Equation 3.21,  $B_m^{CX}$  and  $B_m^{BES}$  are regarded integrated over the wavelength as the corresponding theoretical backgrounds (Equation 3.16 and Equation 3.17). However, in reality the spectra are measured in pixel ( $\text{pixel}_{CX}$  and  $\text{pixel}_{BES}$ , respectively) and not in nm. Therefore, the dispersion of the given camera have to be used. The dispersion of the  $C^{5+}$  and the  $H_\alpha$  cameras is displayed in Equation 3.22 and 3.23, respectively.

$$\omega^{CX} = \frac{dl}{dp_{x_{CX}}} \quad (3.22)$$

$$\omega^{BES} = \frac{dl}{dp_{x_{BES}}} \quad (3.23)$$

Equation 3.21 can therefore be changed in a way so that  $B_m^{CX}$  and  $B_m^{BES}$  are regarded integrated over the respective pixel:

$$\frac{\eta_{CX}}{\eta_{BES}} = \frac{\lambda^{BES}}{\lambda^{CX}} \frac{B_m^{CX}/\omega_{CX}}{B_m^{BES}/\omega_{BES}} \quad (3.24)$$

Consequently, the fraction of the carbon density and the electron density is calculated as follows:

$$\frac{n_C}{n_e} = \frac{I_m^{CX}}{\sum_{E=E_0, E_0/2, E_0/3} \frac{I_{E,m}^{BES} Q_E^{CX}}{Q_E^{BES}}} \frac{B_m^{CX}/\omega_{CX}}{B_m^{BES}/\omega_{BES}} \frac{\lambda^{BES}}{\lambda^{CX}} \quad (3.25)$$

The individual frames, and thus spectra, produced by the cameras represent the given impurity radiation that was detected in a time period equal to the length of the exposure time. This needs to be taken into account during the processing of the spectra. During NBI blips with a length comparable to the exposure time of one of the cameras, it is possible that none of the frames cover a time range where the NBI is turned on for the whole period. This typically happens for blips that are  $< 30$  ms. Even if one frame had full NBI coverage in the middle of the blip, the other frames, which in this case are usually the first and last frames for the given NBI blip, do not. Furthermore, this is not necessarily consistent for each blip of a series of blips throughout a plasma discharge, as the the start of a blip does not always line up with the exposure time of the CXRS diagnostic. Example cases of how the NBI blips and the frames can take place related to each other can be seen in Figure 3.9. This is not an issue during NBI pulses  $> 30$  ms, as there are enough NBI frames recorded so that the first and last one can be always disposed. In contrast, for blips  $< 30$  ms, the measured light is summed up between all frames that at least partly overlap with a given NBI blip, creating one summed spectrum for each blip. This ensures that for every blip all the radiation induced by the given NBI blip is recorded in the summed frame for both the  $C^{5+}$  and the  $H_\alpha$  spectra, regardless of the length of the camera exposure time.

However, summing up all frames of a given NBI blip introduces additional problems. For NBI pulses without summing, the time unit of  $I_m^{CX}$  and  $B_m^{CX}$  is both  $(t_{frame}^{CX})^{-1}$ , which therefore cancel out in Equation 3.25. The same is true for  $I_{E,m}^{BES}$  and  $B_m^{BES}$ , as their time unit  $(t_{frame}^{BES})^{-1}$  eliminate each

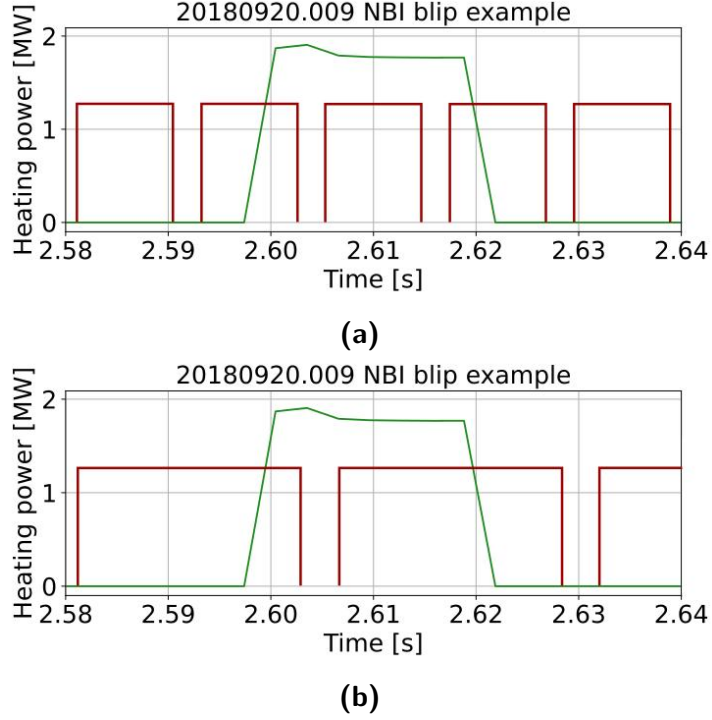


**Figure 3.9.:** Examples for the relation between an NBI blip (green) and the radiation detection by the spectrometer cameras (red) as a function of time.

other. The fraction of  $n_e$  and  $n_C$  is therefore dimensionless, as intended. However, when summing all frames of an NBI blip to obtain  $I_m^{CX}$  and  $I_{E,m}^{BES}$ , their effective exposure time changes to  $t_{blip}$ . These two eliminate each other during the division in Equation 3.25. As a result,  $I_m^{CX}$  and  $I_{E,m}^{BES}$  do not carry the exposure time information any more that would otherwise be eliminated by the bremsstrahlung cross calibration. This leaves  $B_m^{CX}$  and  $B_m^{BES}$  carrying their respective camera exposure time information after the cross calibration. To make their time unit match and eliminate each other, both measured bremsstrahlung intensities are divided by the exposure times of the respective cameras,  $t_{exp}^{CX}$  and  $t_{exp}^{BES}$ .

### 3.1.4. Comparison with carbon density profiles with a different approach

The carbon density is calculated for this analysis with the previously described cross calibration method. The conventional method, not using the practicality of the *ILS* spectrometer and its  $C^{5+}$  and the  $H_\alpha$  cameras would require an absolute intensity calibration to convert the measured intensity into density values. An absolute intensity calibration measurement was done prior and after the measurement campaign with a calibration sphere as described in Chapter 2.1.2, with the exception of the *AEA21* system, where an absolute intensity calibration was done only after the campaign. However, the absolute calibration measurement was not processed by the time of this analysis, nor was its accuracy confirmed. The accuracy of the absolute calibration can be affected by erosion of or coating on the first mirror of the port by the plasma, and thus the transmission of the optics can degrade over the time of plasma operation. Additionally, the density of the beam energy components is also needed for the conventional approach, which would need to be derived from a detailed accurate beam model, which was not available for W7-X at the time. The decision to calculate carbon density with the cross calibration method for this analysis, was made due to the reduced complexity of the calculation, and due to no reliance on an absolute calibration or a beam model.

Towards the end of this work, another investigation has been done on a topic of different focus that calculated the carbon density using the other approach [84]. By the time this new analysis started, the beam modelling code FIDASIM has been developed and tested also for W7-X plasmas [85]. FIDASIM predicts the active  $H_\alpha$  spectrum by calculating the density of neutrals in quantum states  $n = 1 - 6$  within the neutral beam. It models charge exchange reactions between neutrals and ions by solving the rate equations. The predicted experimental beam emission spectra show good agreement with the measured beam emission and therefore the density of the beam energy components calculated by FIDASIM can be reliably used for the carbon density calculation. The new analysis was also able to use the processed and verified absolute intensity calibration of the CXRS system. The absolute intensity calibration is now considered reliable due to both the FIDASIM beam emission comparison and successful modelling of Bremsstrahlung emission from  $Z_{eff}$  profiles [86].

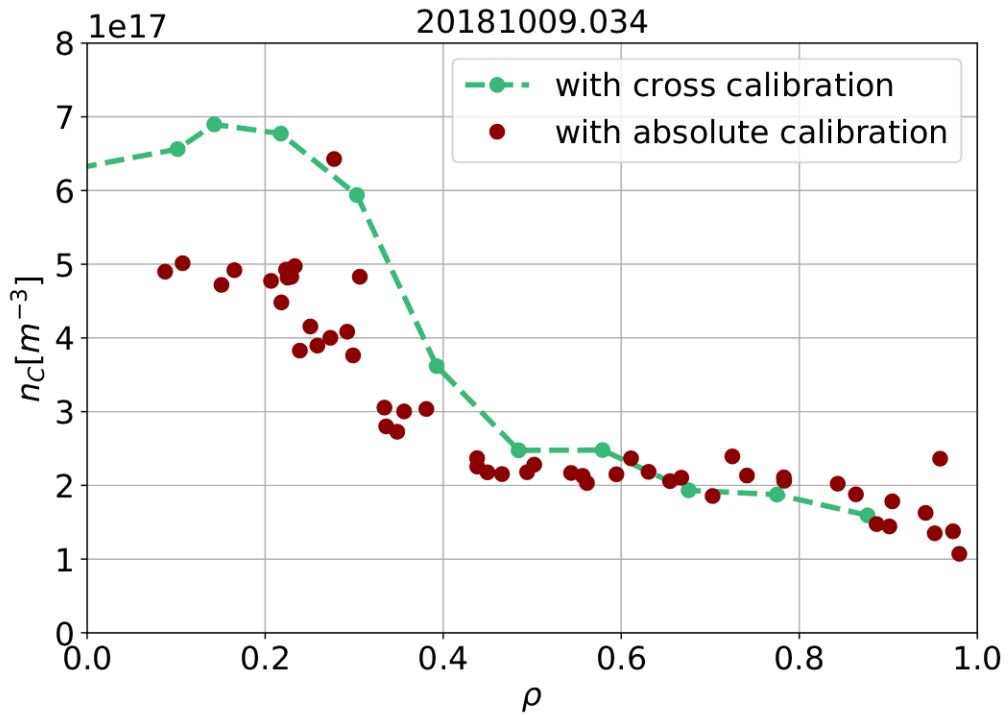


**Figure 3.10.:** Comparison of carbon density profiles from an example time point of discharge 20181009.034. The density was calculated with the cross calibration method described in Section 3.1.3 (green dashed line) and with the use of absolute intensity calibration and modelled beam densities (red dots).

An example carbon density profile calculated from both the presented analysis and the analysis using absolute calibration and modelled beam densities is shown in Figure 3.10. This example is from a pure NBI heated plasma phase. Comparing the two profiles, good agreement can be seen outside half radius as the profiles match. Within half radius, the profile shape is similar, while the density values differ within 15%. For ECRH dominated plasmas, the difference between the profiles from the two methods is higher (around 30%), but all the values stay within the same order of magnitude and the shape of the profiles match in all cases. This agreement is sufficient enough that it validates the results of both works. Further investigation is needed to resolve the observed slight difference between the exact values.

### 3.1.5. Contribution of the neutral beam halo to the measured carbon intensity

The halo of neutral hydrogen around the beam line (see Section 1.2.3) contributes to the active component of the  $C^{5+}$  spectrum. Charge exchange can happen between these neutrals and fully-stripped  $C^{6+}$  ions, creating another source of  $C^{5+}$  ions that are only present while the NBI is being used. This radiation comes from a source of neutrals that is not accounted for in Equation 3.2. The corrected equation taking into account the contribution of the halo is shown in Equation 3.26.

$$I^{CX} = \sum_{E=E_0, E_0/2, E_0/3} I_E^{CX} + I_{halo}^{CX} \quad (3.26)$$

$$I_E^{CX} = \int_{LOS} n_C(l) Q_E^{CX}(l) n_E^{beam}(l) dl \quad (3.27)$$

$$I_{halo}^{CX} = \int_{LOS} n_C(l) Q_{halo}^{CX}(l) n^{halo}(l) dl \quad (3.28)$$

$I_E^{CX}$  is the intensity of the radiation from a given beam energy component without the effect of the halo, as seen earlier, shown in Equation 3.27.  $I_{halo}^{CX}$  is the intensity of the measured radiation resulting from charge exchange with halo neutrals, defined in Equation 3.28.  $n^{halo}$  is the density of the halo and  $Q_{halo}^{CX}$  is the charge exchange emission coefficient at the energy of the halo neutrals. With the modified  $I^{CX}$  definition, Equation 3.9 is not applicable any more. As a result, without considering contributions from halo neutrals, the presented cross calibration approach overestimates the carbon density. Additionally, since the halo is less localised than the beam density, the radiation resulting from charge exchange with halo neutrals makes the LOS integration region longer. However, the beam models from FIDASIM show that this effect is relatively small and the assumption of Equation 3.4 and Equation 3.5 remains valid.

To determine whether the radiation from the beam halo is negligible and if needed, to account for it, the contribution of the halo neutral population in the measured active component has to be estimated. This has been done on other fusion devices with various simulations. For this work, an estimation based on the beam modelling FIDASIM code [87] [88] is used. Besides

the main beam neutral populations (beam energy components), FIDASIM also simulates the density of the halo. According to estimations made for W7-X [85], the  $n = 2$  population of the halo has a contribution to the measured active  $C^{5+}$  signal that is comparable to the contribution of the first energy component, the one with the highest density out of the three energy components. Thus, the halo contribution has to be subtracted from the intensity of the active component. The calculations of the simulated halo density for W7-X plasmas were reliably available towards the end of this work. The percentage of the halo contribution depends on the global plasma parameters, such as  $T_e$  and  $n_e$ , as well as the beam energy. Therefore it has to be estimated for the investigated plasma scenarios individually. For ECRH dominated discharges, the halo contribution is typically around 20%, while for NBI dominated discharges, it can increase to around 30% or more of the active signal.

The carbon densities shown in Section 3.2 all account for the contribution from the halo according to the results of [84].

## 3.2. Investigation of carbon transport in the plasma core

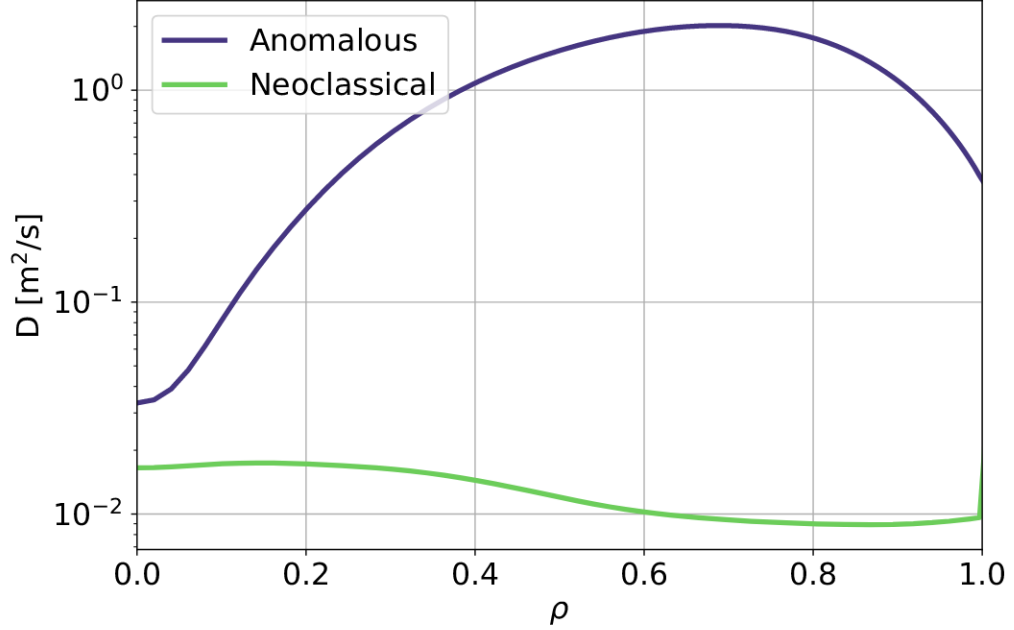
The carbon density profile derived from the measured  $C^{5+}$  spectra with the method described in Section 3.1.3 are investigated and presented in this section. This is done for different plasma scenarios, in order to assess how the carbon behaviour depends on different heating methods in the plasma core. The two primary heating scenarios investigated are plasmas heated by only ECRH (with short NBI blips that do not contribute to the heating of the plasma, only provide a possibility for CXRS measurements) and purely NBI heated plasmas. A carbon transport analysis is done for these cases. Mixed heating and pellet induced high performance scenarios are also examined without a thorough transport analysis.

### 3.2.1. Carbon transport in ECRH dominated plasma scenarios

Plasmas whose dominating heating method is ECRH and which only had NBI blips with a length  $< 30$  ms for diagnostic purposes, are investigated in this section.

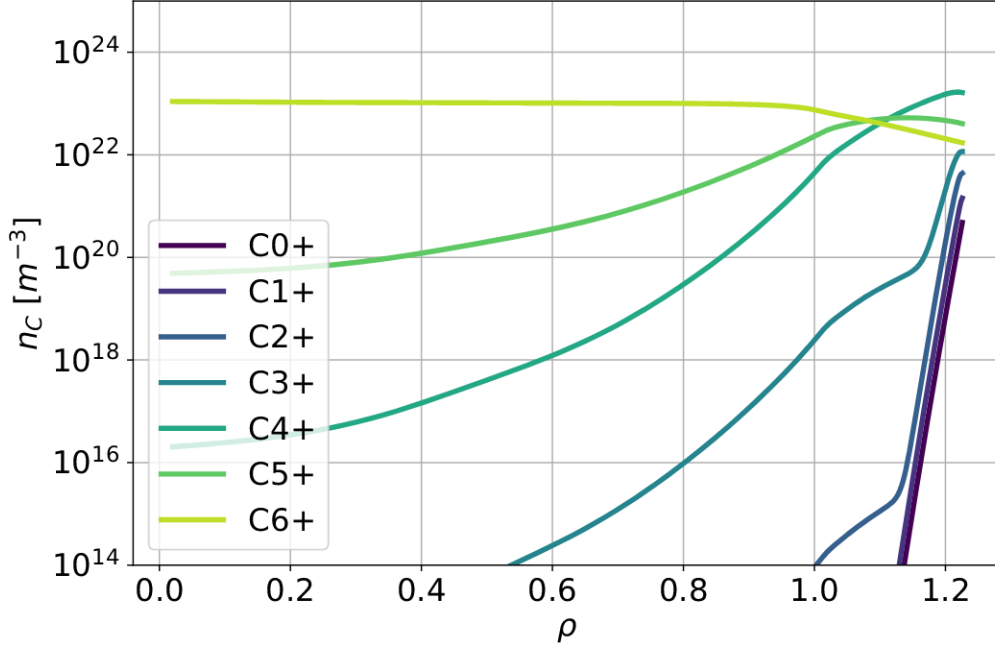
The  $C^{6+}$  density profile shape is consistently flat within  $\rho < 0.9$  during all ECRH dominated discharges analysed. A flat profile is defined if  $\frac{n_{core}}{n_{edge}} \approx 1$ . As neoclassical models for W7-X plasmas typically predict impurity accumulation with peaked impurity density profiles (see Section 1.4), flat carbon density profiles indicate that there is an anomalous component present in the plasma. An additional transport force is needed to keep the profiles flat, to counteract the neoclassical convection that would drive profile peaking. An impurity transport study was previously carried out on W7-X based on high-Z impurity injections that showed around an order of magnitude higher diffusion than the neoclassical level in the ECRH dominated discharge 20180906.038 [89]. Simulations were done for [89] with the impurity transport code pySTRAHL [64] (see Section 1.5), and such high diffusion was needed to match the simulated injected impurity density with the measured ones. The detailed results of the transport properties suggest that the driving force of the anomalous impurity transport is turbulence. This is broadly consistent with other studies which show that heat transport is dominated by turbulence in W7-X plasmas [54] [90] [91]. No strong anomalous convection velocity was found during the study, which agrees with the turbulent transport theory [92]. The diffusion profile was found to scale with the ECRH power level in [89]. This study serves as a basis for the anomalous diffusion of carbon in the following transport investigations. The anomalous diffusion profile established in [89] is scaled according to the ECRH power of the investigated discharges in Section 3.2.1 and Section 3.2.3.

Figure 3.11 shows the neoclassical and scaled anomalous diffusion profile for the ECRH dominated phase of an example discharge. The neoclassical diffusion, along with the neoclassical convection velocity, for carbon is calculated by the neoclassical transport simulation code Neotransp. Neotransp uses tabulated mono-energetic transport coefficients calculated by the DKES transport code [93] [94] for the specific magnetic equilibria used in W7-X.



**Figure 3.11.:** Neoclassical diffusion (green) and the sum of the neoclassical and anomalous diffusion (purple) for the ECRH dominated time range of discharge 20181009.034. The anomalous diffusion is derived from time dependent analysis of impurities injected by Laser Blow-Off [89] [56] and was scaled with the ECRH power used, in accordance with the scaling found in that study.

The transport coefficients are weighted with the Maxwellian distribution and integrated over velocity to obtain a transport matrix. This matrix is then multiplied with the thermodynamic forces related to the radial electric field [42] [43] and the radial gradients of related density and temperature, in order to obtain the radial fluxes and transport characteristics of given particles and energy [53]. The anomalous contribution of the diffusion dominates the neoclassical contribution, as it is several orders of magnitude higher. Carbon density profiles simulated by pySTRAHL using the presented anomalous diffusion with background plasma profiles ( $n_e$ ,  $T_e$ ,  $T_i$ ,  $B$ ) are shown in Figure 3.12 for all carbon ionisation stages. The simulated flat  $C^{6+}$  density profile can be easily understood from the boundary conditions. ECRH dominated plasma phases are in a steady state ( $\Gamma_{imp} = 0$ ), as all the



**Figure 3.12.:** Density profile of all ionisation stages of carbon in a standard ECRH dominated plasma.  $\rho = 1$  marks the LCFS. The carbon is fully ionised for most of the confined plasma and the profile of this ionisation stage is flat throughout the plasma radius.

background parameters stay constant in these cases, as seen in Figure 3.13 for an example discharge. In steady state scenarios, the peaking factor is proportional to  $v/D$  according to Equation 1.12. Thus, the simulated dominating anomalous diffusion and low level convection velocity necessarily results in flat impurity density profiles. These flat profiles match the shape of the experimentally obtained  $C^{6+}$  profile of the corresponding plasma discharge. This is observed consistently in other ECRH dominated plasmas analysed.

It is important to note that the dominating nature of anomalous diffusion limits the accuracy of this type of transport analysis. The precise value of the anomalous diffusion cannot be modelled sensitively, as any diffusion, which is much larger (few orders of magnitude) than the neoclassical diffusion and convection, will produce similarly flat impurity density profiles.

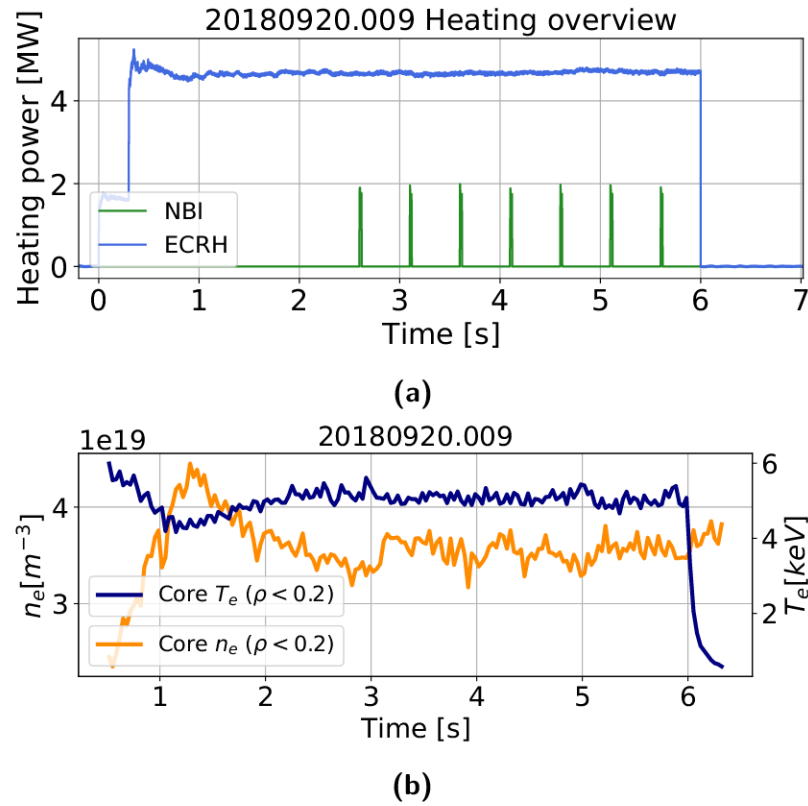


**Figure 3.13.:** Global parameters of discharge 20180920.009. Time evolution of the ECRH power (blue) and NBI heating power (green) (a). Time trace of the core electron density ( $n_e$ , orange) and core electron temperature ( $T_e$ , dark blue) measured by the Thomson Scattering diagnostic (b).

### 3.2.2. Dependencies of carbon density in ECRH dominated plasma scenarios

In this section, the  $C^{6+}$  density was analysed for different background electron densities and different ECRH heating powers to study its dependency on these global parameters. Such dependency investigations are important for the planning of future experiments to further optimise plasma performance regarding the low- $Z$  impurity density in the plasma.

Carbon density profiles calculated from CXRS measurements with the method presented in Section 3.1.3 were used as the basis of a study on the

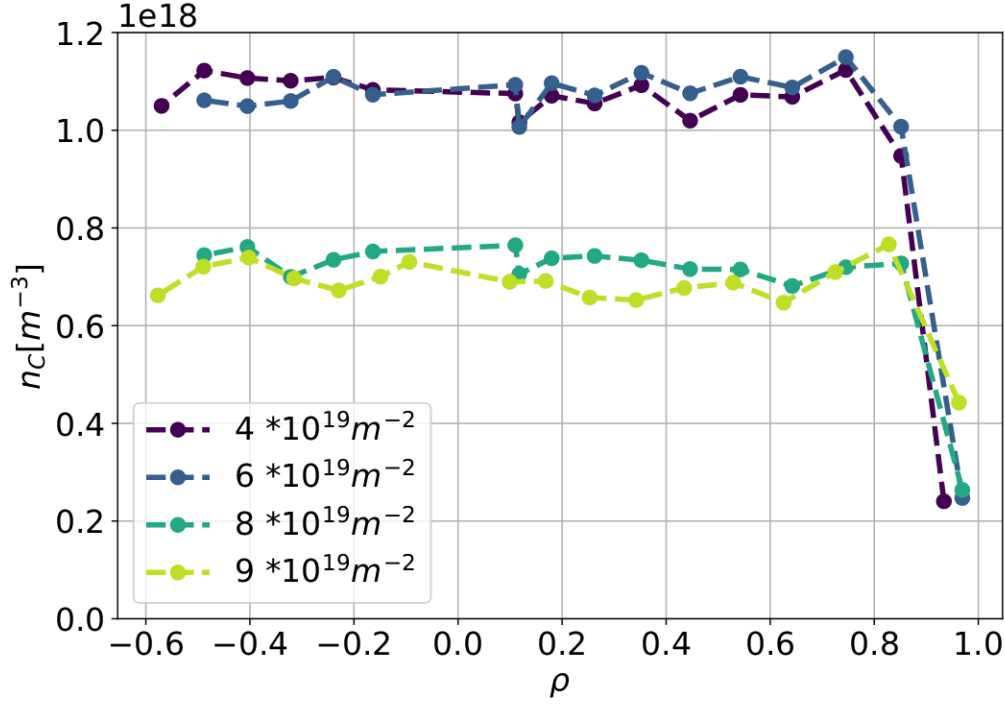


**Figure 3.14.:** Average carbon density profile of discharges 20180920.009, 013, 017, 033. These otherwise identical discharges had electron densities of  $4, 6, 8, 9 \times 10^{19} m^{-3}$ . This allows the investigation of the dependence of the carbon content on the plasma density.

electron density dependence of the carbon density level [95]. A summary of the results of this study are presented here. Four discharges were conducted on the same day with almost identical global parameters, with only  $n_e$  being different, in order to consider the background electron density dependence of the plasma edge conditions. The four discharges of the density scan are 20180920.009, 013, 017, 033, with  $n_e = 4, 6, 8, 9 \times 10^{19} m^{-3}$ , respectively.  $n_e$  in this case refers to the line integrated electron density measured by the Interferometer. All discharges were heated with  $P_{ECCRH} = 4.5$  MW containing 6-7 20 ms long NBI blips throughout the discharge. The heating overview, as well as the time evolution of the background plasma parameters can be seen in Figure 3.13a and Figure 3.13b. As the plasma conditions are

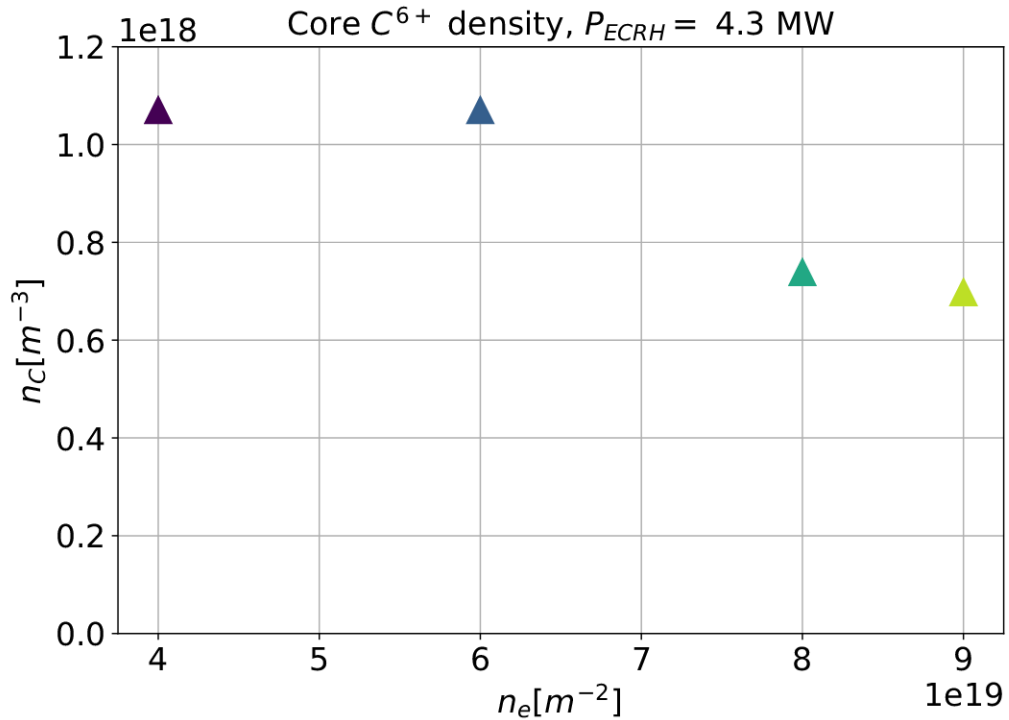


**Figure 3.15.:** Average core carbon density of discharges 20180920.009, 013, 017, 033 as a function of the corresponding background electron densities. With higher the electron density, lower the carbon density levels are observed.

deliberately kept constant throughout the whole period of each discharge, the carbon density and concentration level does not change significantly within one discharge. Therefore, the carbon density profile is averaged over the NBI blips in each discharge. The averaged carbon density profile of the four discharges can be seen in Figure 3.14. The carbon density profiles are flat, while the carbon concentration profiles are slightly hollow, as the electron density profiles are marginally peaked. Figure 3.15 shows the core carbon density as a function of the electron density. As the electron density increases, the observed carbon density generally decreases.

Calculations based on the C<sup>2+</sup> line at 514.3 nm show no significant increase in the carbon source at the divertor with increasing background

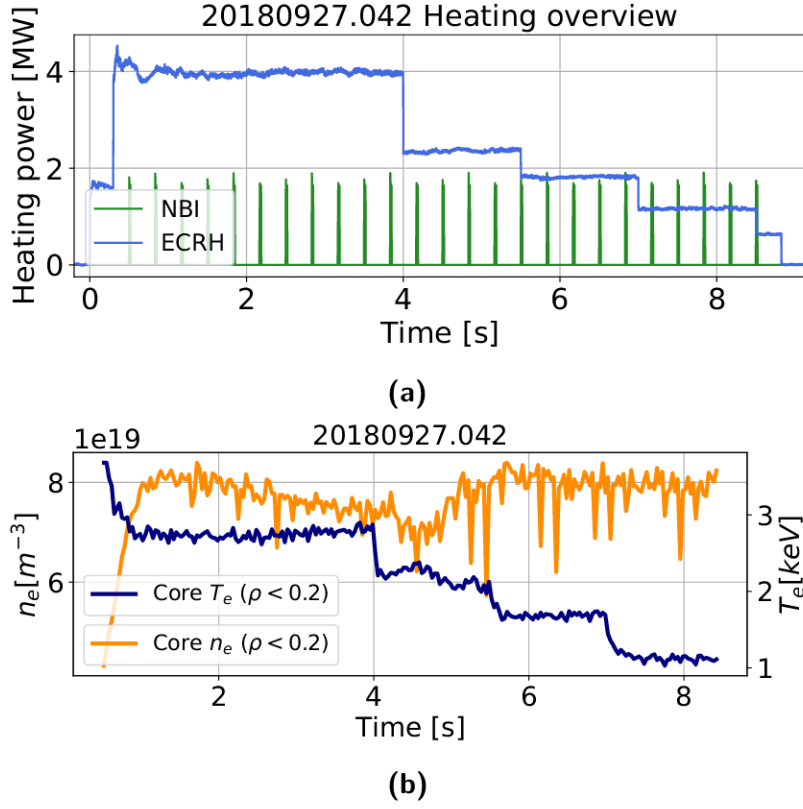


**Figure 3.16.:** Global parameters of discharge 20180927.042. Overview on the heating methods (a) with the time trace of the ECRH power (blue) and NBI heating power (green). Time evolution of the core electron density ( $n_e$ , orange) and core electron temperature ( $T_e$ , dark blue) measured by the Thomson Scattering diagnostic (b).

electron density. As the carbon density decreases in the confined plasma region inside the LCFS with increasing background density as seen in Figure 3.15, this means that more carbon particles are being repelled by processes in the SOL [23] as the background density increases. Models done for the same type of ECRH dominated plasmas predict increasing impurity retention in the island structure of W7-X, if the background density at the LCFS is increased. Higher impurity retention means that the SOL has a better ability to keep the impurities out of the confined plasma inside the LCFS. The experimental carbon retention is consistent with these simulations.

Discharges with changing ECRH power level allow the examination of ECRH power dependence of the confined carbon content. Figure 3.16a shows the the ECRH power of discharge 20180927.042 that has four power steps,  $P_{ECRH} = 1.2, 1.8, 2.4, 3.9$  MW, with  $n_e = 8 * 10^{19} \text{ m}^{-3}$  throughout the whole discharge. There are at least four NBI blips of 20 ms length during each power step. The background plasma conditions do not change within one ECRH power step, as shown in Figure 3.16b. The core carbon density of each power step is shown in Figure 3.17 as a function of ECRH power, with the density of each blip within a given step being averaged. As the ECRH power is increased the carbon density also increases. This is in accordance with expectations regarding the the plasma facing elements, as more heating power means more heat load on the carbon wall and divertor. This increases the carbon source (see Section 1.4), and therefore the density of the confined carbon in the plasma.

The presented electron density and ECRH power scans are consistent. Considering the electron density of discharge 20180927.042 ( $n_e = 8 * 10^{19} \text{ m}^{-3}$ ), it should correspond to a carbon density of  $\approx 7.3 * 10^{17} \text{ m}^{-3}$  in the case of  $P_{ECRH} = 4.3$  MW in the density scan. Extrapolation of a linear fit on the ECRH power dependence of Figure 3.17 results in a measured carbon density of  $7.1 * 10^{17} \text{ m}^{-3}$  at  $P_{ECRH} = 4.3$  MW. The difference of these is small compared to the range of carbon densities seen over the scans.

To provide some context, the carbon concentration observed in the ASDEX Upgrade tokamak is considered in comparison to the W7-X carbon concentration. For  $n_e = 5 * 10^{19} \text{ m}^{-3}$ , the typical carbon concentration observed at the ASDEX Upgrade is  $C_C^{AUG} \approx 0.2\%$  [96]. The carbon concentration observed at W7-X at similar electron densities is  $C_C^{W7-X} \approx 3.2\%$  according to Figure 3.15. The wall and divertor of ASDEX Upgrade is tungsten, as opposed to the carbon wall of W7-X, so  $C_C^{AUG}$  being around one order of magnitude lower than  $C_C^{W7-X}$  is a realistic difference.

### 3.2.3. Carbon density behaviour in NBI heated plasma scenarios

To investigate the effects of the NBI on the impurity conditions in plasma, discharge phases purely heated by NBI were analysed. Their carbon density profiles, as well as transport simulations based on these profiles are presented

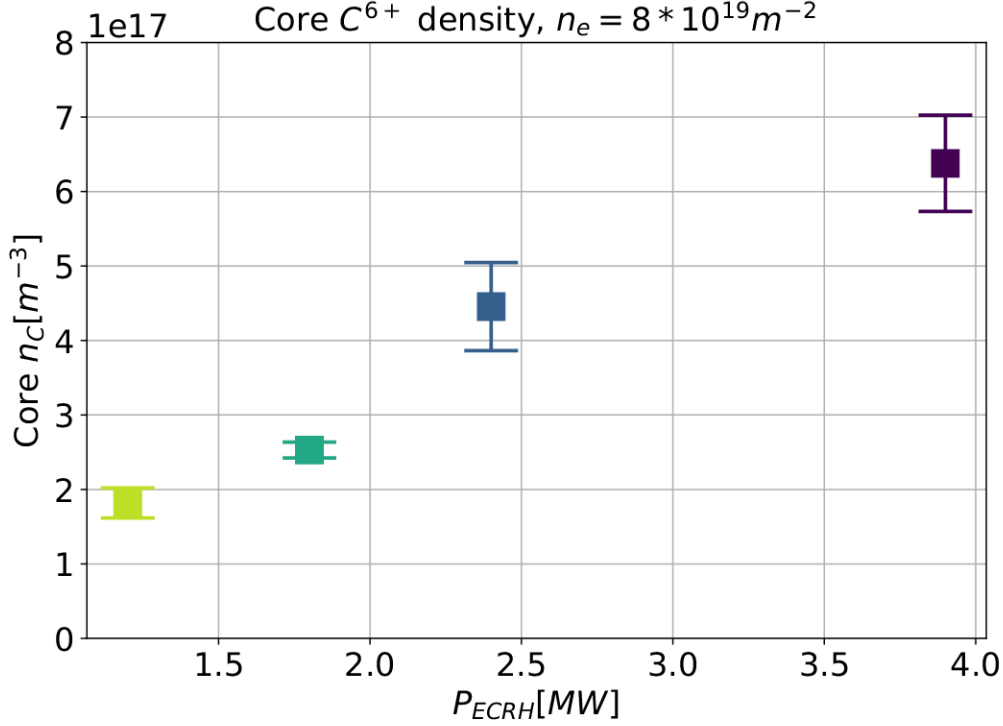


**Figure 3.17.:** Average carbon density level of each NBI blip in discharge 20180927.042 as a function of ECRH power. The two quantities are proportional, the carbon density is increased with higher ECRH power.

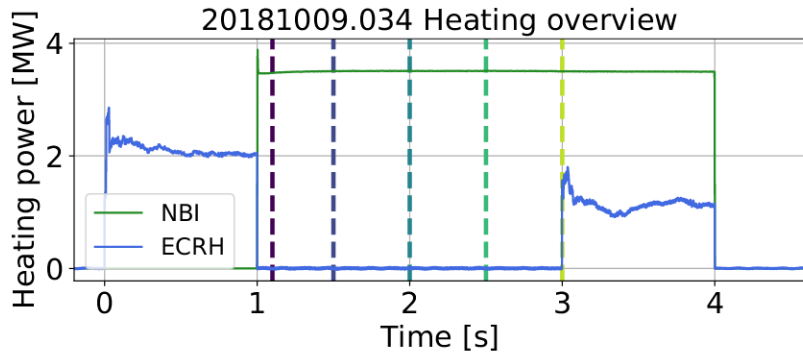
in this section.

Discharge 20181009.034 was chosen as the main subject of this analysis, due to its unique heating conditions. The global parameters through this discharge are shown in Figure 3.18. In the first second, 2 MW X2 ECRH heating was used to start-up the plasma. ECRH is used to start up the plasma in all discharges as NBI is not suitable to generate plasmas in W7-X. The angle of the NBI beam line is close to radial towards the device, and therefore the interaction length of the beam and the plasma is relatively short. This makes the NBI inefficient for plasma generation. [97] At  $t = 1$  s, the ECRH is turned off and from  $t = 1$  s to  $t = 3$  s, the plasma is heated by only NBI, with  $P_{NBI} = 3.5$  MW, using both sources. At  $t = 3$  s, ECRH is turned back on with O2 heating applying  $P_{ECRH} = 1.2$  MW, which

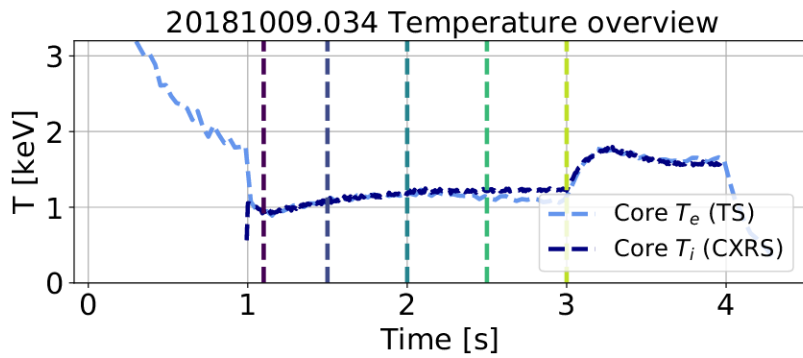
is a relatively low heating power. The NBI is kept on after  $t = 3$  s. The plasma terminates at  $t = 4$  s. The overview of the heating conditions of the discharge is shown in Figure 3.18a.

Figure 3.18b shows the electron temperature ( $T_e$ ) throughout the discharge measured by the Thomson Scattering diagnostic, and the ion temperature ( $T_i$ ) obtained from the carbon spectrum measured by the CXRS diagnostic. The carbon spectrum provides the temperature of the fully stripped carbon ion ( $T_C$ ). It is assumed that the temperature of the thermal  $H^+$  ions ( $T_i$ ) and the other fully stripped ions present in the plasma is the same because the equilibration time of the main ions with the impurities is much shorter than the ion-electron equilibration time of both main ions and impurities. The time trace of the electron density ( $n_e$ ) measured by the Thomson Scattering diagnostic and the carbon density ( $n_C$ ) derived from the CXRS signal (the result of the presented analysis) is displayed in Figure 3.18c.

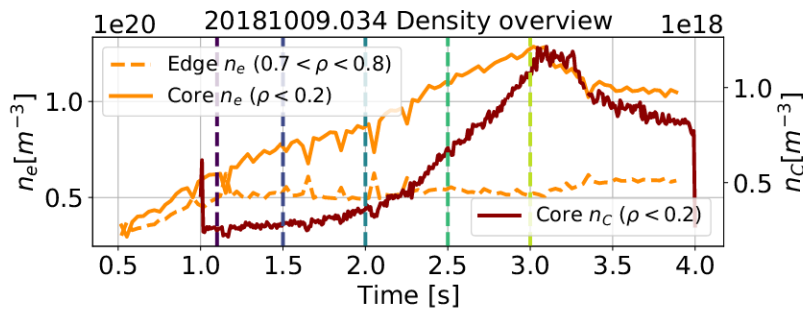
$T_e$  is above  $T_i$  during the ECRH heated phase (there are no active CXRS measurements for this phase, as the NBI was not turned on, but  $T_i$  is also available from the XICS diagnostic). This is commonly observed in ECRH dominated discharges. A so-called  $T_i$  limit is observed at  $T_i \approx 1.6$  keV, above which the ion temperature does not rise in standard ECRH plasma conditions [98] [54]. For reference, temperatures of up to  $T_e = 8$  keV were achieved throughout the campaign. In contrast, models with neoclassical or moderate turbulent transport predict  $T_i \approx 3$  keV. A possible candidate for this limitation is ion temperature gradient (ITG) driven turbulence. This has been found in all plasma scenarios with only gas fuelling (no pellet injection) and ECRH heating. This dominance of the turbulence in the heat transport is also consistent with the observed turbulence dominated impurity transport in ECRH plasmas.  $T_i$  is only observed to be able to rise above this limit when the heating is dominated by NBI with a low level of ECRH power added, or after the injection of a series of hydrogen pellets, impurity pellets or boron powder [98]. It has been shown that the ITG turbulence is suppressed in these plasma scenarios by the strong density gradients. This makes these scenarios favourable for achieving higher ion temperatures in W7-X. Higher ion temperatures are important for possible future fusion reactions in a power plant, since for these reactions to ignite, it is the main ions that need to be heated to the critical temperature (see Section 1.1).



(a)



(b)



(c)

**Figure 3.18.:** Global parameters of discharge 20181009.034. Time trace of the ECRH power (blue) and the NBI heating power (green) (a). Time trace of the core electron temperature (light blue) and the core ion temperature (dark blue) (b). Time trace of the core electron density (orange, solid line), the electron density outside of half radius (orange, dashed line) and the core carbon density (red) (c). The chosen example time points are displayed as vertical dashed lines on all three figures in colours that match the colour of the example carbon density profiles in Figure 3.20.

When the ECRH is turned off in discharge 20181009.034, both temperatures drop immediately to the same level, then start rising during the NBI operation with a slow increase, while staying equal to each other. This suggests that the electron and main ion temperature is strongly coupled during the pure NBI phase, considering that the NBI heats both the electrons and the main ions.  $n_e$  is constantly rising during the phase heated only with ECRH, the edge density stagnates after the heating power switch, while the core density continues to rise. Thus, the  $n_e$  profile becomes more and more peaked in the core as the NBI is heating the plasma, as shown in Figure 3.19. The  $n_c$  profile is not measured during the first phase, although it can be assumed to be similar to the first time point of the NBI phase. This is a safe assumption, because by that time, not more than a typical blip length has passed since the ECRH was turned off, and it has been established in previous investigations that  $n_C$  does not change significantly within 30 ms of NBI operation (length of a blip). At this time point, the  $n_C$  profile is flat as seen in Figure 3.20. After the NBI is turned on, the core  $n_C$  starts rising at a slightly slower rate than the core electron density.

After around one second of pure NBI heating ( $t \approx 2$  s), the behaviour of all the presented plasma parameters change to some extent. The rise in  $T_e$  and  $T_i$  stops,  $T_i$  stagnates and  $T_e$  decreases slightly. There seems to be a change in the electron and main ion particle and heat transport. This transport change seem to be causing the change in the development of  $T_e$  and  $T_i$ . The core  $n_e$  peaking rate becomes marginally higher at  $t \approx 2$  s (due to changed electron particle transport), while the core  $n_C$  peaking rate strongly increases, making the core  $n_C$  rise significantly faster than the core  $n_e$ . This difference in peaking rate is visible in the carbon concentration profiles. These profiles remain nearly flat for  $t < 2$  s, as  $n_C$  and  $n_e$  peak at similar rates, then at  $t \approx 2$  s, the carbon concentration profiles also start peaking significantly in the core. This change in behaviour after a given time period of pure NBI operation ( $t_{onset}$ ) is seen in other pure NBI discharges as well. While in discharge 20181009.034  $t_{onset} \approx 1$  s, in other pure NBI discharges this can range from 0.8s to typically 1.6 s, with one case having  $t_{onset} = 3.8$  s. Neither are changes observed at the plasma edge, nor any additional plasma events can be seen that would induce those changes in the  $n_c$  and  $n_e$  time evolution. The processes behind why the plasma behaviour changes after  $t_{onset}$  and the  $t_{onset}$  variations between discharges is not yet understood [98].

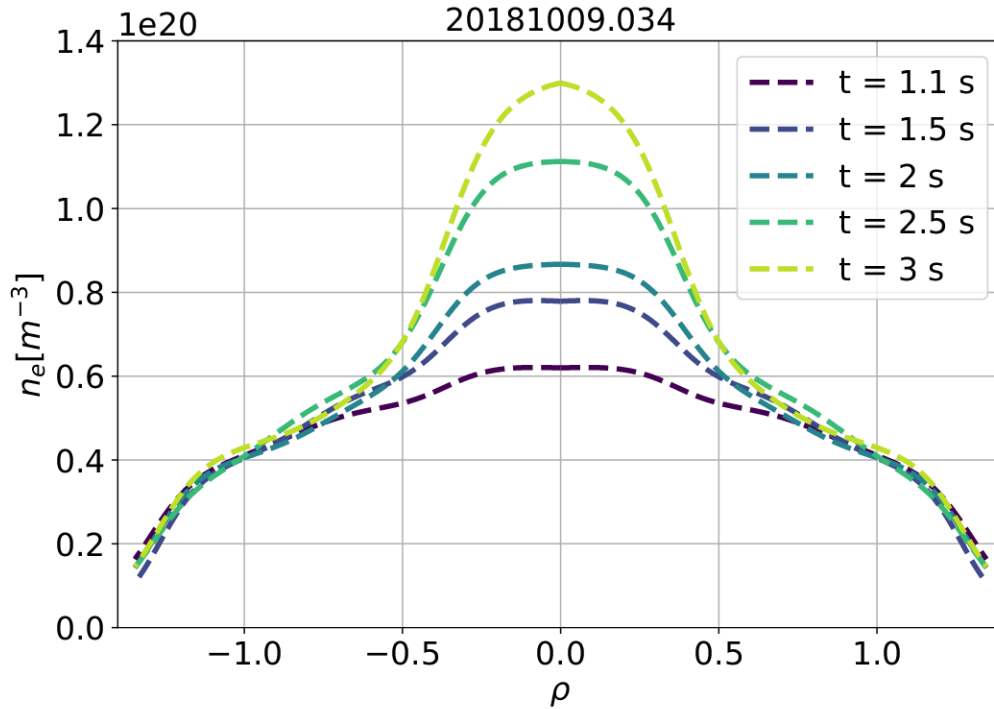


**Figure 3.19.:** Example electron density profiles at the times highlighted in Figure 3.18. The  $n_e$  profile is marginally peaked during the only ECRH phase as seen also in other ECRH dominated plasmas. It starts peaking in the core more and more as the plasma is heated by only NBI.

The plasma conditions change drastically when an additional low power ECRH is turned on at  $t = 3$  s. These changes are investigated in Section 3.2.5 as the ECRH and NBI heating is combined in this plasma phase.

### 3.2.4. Carbon transport evolution in NBI heated plasma scenarios

Five example time points are chosen to demonstrate the changes in the carbon density profiles in a purely NBI heated plasma. At every half second of the NBI operation lies a chosen time point, as well as at  $t = 1.1$  s, treated as a reference representing the ECRH dominated plasma phase, as the  $n_C$  profile does not show any significant change between  $t = 1$  s and  $t = 1.1$  s.

The  $n_C$  profiles from these time points are shown in Figure 3.20. They correspond to the highlighted time points in Figure 3.18. As seen from the time trace of the core  $n_C$  in Figure 3.18, the carbon density profiles stay flat in the beginning of the NBI phase. Then the density starts continuously rising for  $\rho < 0.5$ . At  $t \approx 2$  s ( $t_{onset} \approx 1$  s), the rising rate increases and a more defined peak becomes visible in the core. The density stays the same for  $\rho > 0.5$  during the NBI phase. It is important to note that the spatial points at  $\rho > 0.7$  in the density profile are less reliable than the rest of the profile, as the temperature of the  $C^{6+}$  ions (active component) is comparable with the temperature of the  $C^{5+}$  ions present at the plasma edge (passive component). Thus, the separation of the two components becomes less reliable.

Rising  $n_C$  peaking in the core means that the carbon accumulates within  $\rho = 0.5$  during pure NBI heating. This is a similar behaviour as predicted by models considering purely neoclassical impurity transport for W7-X (see Section 1.4). The aim of the following analysis is to determine dominant factors governing the carbon transport during pure NBI heating. It is investigated, whether neoclassical carbon transport can explain the observed accumulation, and if not, what additional transport needs to be added to simulate the measured carbon profiles.

Carbon transport simulations are performed with the 1D impurity transport code pySTRAHL (see Section 1.3), where the transport coefficients, diffusion and convection velocity, are input parameters. The convection velocity is kept at neoclassical levels, as no strong anomalous convection was found even in highly anomalous plasmas [89]. If purely neoclassical diffusion does not suffice to describe the measured  $n_C$  profile, an anomalous diffusion is added based on the knowledge of the turbulent diffusion profile obtained in [89]. The diffusion profile is scaled to match the simulated  $n_C$  profiles with the experimentally obtained  $n_C$  profiles with the corresponding time evolution.

One comprehensive simulation is constructed by pySTRAHL which models the investigated pure NBI discharges and their impurity transport regime. The radial range of the simulation is set to  $0 < \rho < 1.2$  including the edge processes which bring the carbon inside the confined plasma region. Profiles of experimental background parameters are used from the given discharge in 100 ms steps of the investigated time range. Electron temperature and density profiles are taken from the Thomson Scattering diagnostic, ion tem-

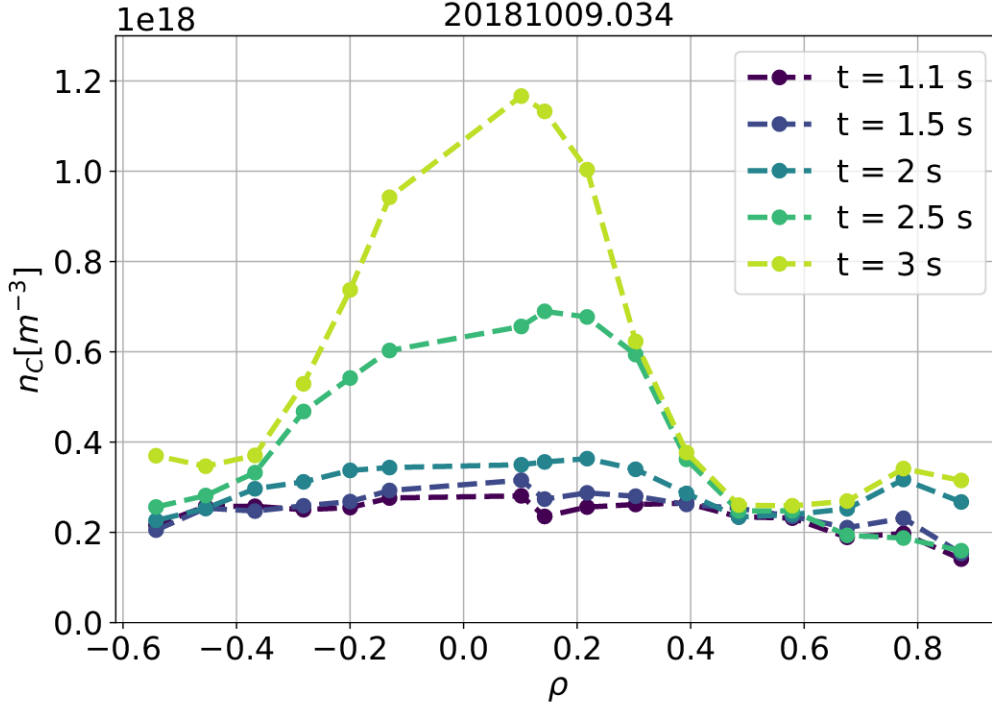


**Figure 3.20.:** Carbon density profiles from the selected time points. The colour of the profiles match the time points highlighted in Figure 3.18. The profile is flat during the only ECRH heated phase ( $t < 1$  s), then becomes more and more peaked as the plasma is heated by solely NBI ( $1 \text{ s} < t < 3 \text{ s}$ ).

perature profiles are taken from CXRS measurements. A neutral density profile is taken from the modelling code KN1D [99], as there is no spatially resolved measurement for thermal neutrals inside the LCFS. KN1D provides a one dimensional simulation of the neutral density profile based on the measured particle pressure at the plasma facing components. However, the effect of the shape and level of the neutral density on the simulated carbon density profiles is negligible. It mostly affects the edge of the plasma, as there is no significant thermal neutral population in the plasma core given the high temperatures.

The initial carbon density is set to zero, as it is at the start of the experiment. The carbon source (which is the wall facing the plasma) is set

to be at  $\rho = 1.2$ . The carbon is modelled to be brought into the confined plasma region by diffusion influenced by simulated SOL conditions. The input pySTRAHL parameters that define the SOL and its processes, like the carbon source rate, are only crudely modelled in this simulation. Given the 1-dimensional nature of the code, the modelling of the SOL processes cannot account for 3-dimensional effects that occur in the SOL. However, this does not affect the analysis, as it focuses on the core carbon density profile, the shape of which is assumed not to be influenced by the SOL and edge processes. This assumption is made based on the estimation of the number of carbon particles accumulating in the core per second by integrating the carbon density over the surface area of the core flux surfaces. The number of accumulating particles was compared to the carbon source rate at the divertor. The carbon source rate was preliminarily estimated for the investigated discharge [100] and it is found to be several orders of magnitude higher ( $N_{source} \approx 10^{22-24} \text{ s}^{-1}$ ) than the estimated number of accumulating carbon particles ( $N_{acc} \approx 10^{18} \text{ s}^{-1}$ ). Additionally, no significant changes are observed throughout the pure NBI phase in the carbon source rate at the divertor. The observed carbon density stays at the same level outside of half radius throughout the pure NBI phase, which agrees with the constant source rate. The plasma volume is larger at the edge than at the core, thus even minor changes in the edge density could result in major changes in the core density, when observed in a flux surface based profile. Therefore, even though the amount of carbon that accumulates in the core is negligible compared to the source rate, it appears as a significant amount in the observed carbon density profile compared to the edge carbon density. Consequently, only the level of the edge carbon density is assumed to depend on the source rate from the divertor and the impurity retention ability of the SOL and the magnetic island structure. Therefore, the input parameters regarding the edge are set so that the simulated carbon density at  $\rho = 1$  is equal to the experimental carbon density at  $\rho = 1$ , assuming that this makes all the effects of the SOL on the confined carbon density profile irrelevant.

Neoclassical diffusion and convection profiles for carbon are calculated by the neoclassical transport simulation code Neotransp (see description in Section 3.2.1). For the Neotransp calculations, the same  $n_e$ ,  $T_e$  and  $T_i$  input profiles are used as for the pySTRAHL simulation, resulting in a neoclassical carbon diffusion and convection velocity profile corresponding

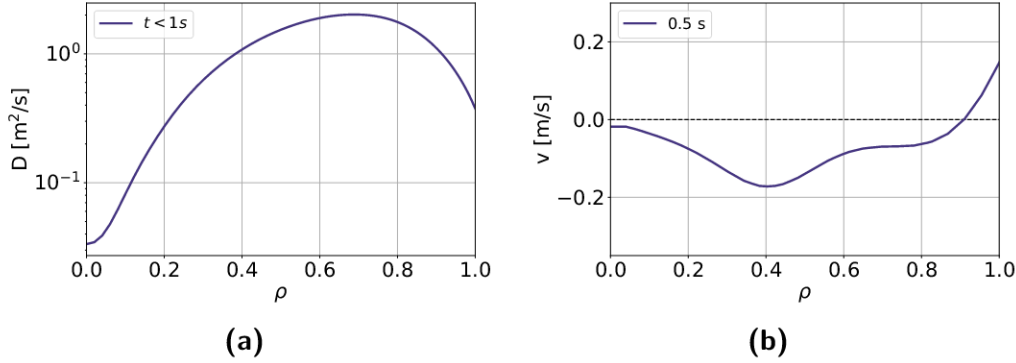


**Figure 3.21.:** Diffusion (a) and convection velocity (b) profiles used in the pySTRAHL simulation of the ECRH phase of discharge 20181009.034. The diffusion profile is dominated by the anomalous component that is obtained from [89] and scaled according to the given ECRH power level. The used convection velocity is assumed to be completely neoclassical.

to every 100 ms of discharge 20181009.034. Anomalous diffusion is added to the neoclassical diffusion profiles as required to match the experimental profiles. The diffusion is set to a fixed level outside of the LCFS. The diffusion outside of the LCFS needs to be high enough so that it transports the carbon to the confined region via density gradient difference from the source (wall).

For  $0 < t < 1$  s, in the ECRH phase, the diffusion was set as seen in Figure 3.11, based on the anomalous diffusion obtained in [89]. The resulting simulated carbon profiles are shown in Figure 3.12. The used diffusion profile is displayed again in Figure 3.21a, while the neoclassical convection velocity based on the given background plasma conditions of the ECRH phase is shown in Figure 3.21b. The sign of the convection is chosen in a way so that the positive values correspond to outward convection, while the negative values correspond to inward convection. The resulting carbon density profile is flattened out, as seen in Figure 3.23a (purple line). This matches the experimental profile, shown in Figure 3.23b (purple line). The direction of the convection velocity is inwards from  $\rho \approx 0.9$ , transporting the carbon particles towards the core. The diffusion always drives particles down the density gradient, thus, it points inwards outside of the LCFS bringing the carbon particles inside the separatrix, as well as at

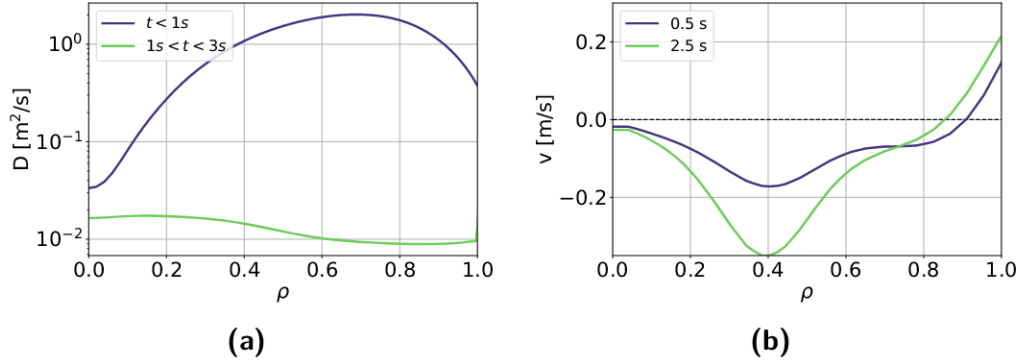


**Figure 3.22.:** Neoclassical diffusion (a) and convection velocity (b) profiles calculated by Neotransp for the given background plasma conditions at  $t = 2.5$  s of discharge 20181009.034, as an example time point from the NBI phase (green). The diffusion and convection velocity profiles used in the ECRH phase ((as shown in Figure 3.21)) are also displayed for comparison (purple).

the edge of the confined plasma where the convection is negative, or positive but close to zero, therefore not as strong. The diffusion points outwards as the neoclassical convection becomes strong enough to create a carbon density gradient towards the core. It counteracts the force of the convection, flattening the carbon density profile.

For the NBI phase of 20181009.034, at  $1 \text{ s} < t < 3 \text{ s}$ , carbon density profiles are first simulated assuming that the carbon transport is fully neoclassical, without any anomalous component. This is done to see whether the carbon accumulation is caused by the changing background plasma parameters and the neoclassical transport alone, or whether the difference between the neoclassical and experimental carbon density profiles would be caused by additional anomalous, presumably turbulent effects. Figure 3.22 shows the neoclassical diffusion and convection velocity profiles from an example time point of the NBI phase in relation to the diffusion and convection profiles from the ECRH phase. The neoclassical diffusion is  $\approx 1 - 2$  orders of magnitude lower than the average anomalous diffusion from the ECRH phase.

To investigate whether the flux related to the neoclassical diffusion ( $D_{NC}$ ) is comparable to the flux related to the neoclassical convection ( $v_{NC}$ ) in the

observed experimental case, or whether the neoclassical convection becomes dominant, Equation 1.12 is considered. The diffusion and the convection term is estimated from the experimental carbon density gradient driving the discussed time range. At  $t = 2.5$  s, the diffusion term is found to be about two orders of magnitude lower than the convection term (left and right side of Equation 3.29, respectively). This weaker diffusive flux is not enough to counteract the flux of the inward pointing convection, which allows the core density to rise, making the density profile peaked.

$$D_{NC} \frac{\partial n_C}{\partial r} \ll v_{NC} n_C \quad (3.29)$$

The simulated neoclassical carbon density profiles are shown in Figure 3.23a, the carbon density profiles calculated from the CXRS signal are shown in Figure 3.23b for comparison. The neoclassical profiles show accumulation in the core as expected from the neoclassical predictions for W7-X. The peaking starts at  $\rho = 0.5$ , which agrees well with the experimental profile shape and peaking location. The growth rate of the peak is also comparable, being only slightly larger in the simulation. The most significant difference between the neoclassical and the experimental  $n_c$  profiles is that the simulated density slowly decreases for  $\rho > 0.5$ , while it stays the same during the experiment. This indicates that the neoclassical  $D$  and  $v$  are not sufficient in this region.

As the radial location, where the peaking starts, is the same in the neoclassical simulation as in the experiment, this radial location is presumably determined by a quantity that is taken into account in the simulation. The neoclassical convection velocity has a relatively high absolute value in the core, then becomes weaker and approaches zero at around  $\rho = 0.6$  and then switches sign at approximately  $\rho = 0.8$ . The observed shape of the neoclassical carbon density is determined by this, thus it presumably originates from a plasma property the convection depends on. This property could be the electron density, as its peaking also starts around this radial location, the development of which might be related to the heating scheme of the NBI. The radial region where the density starts slowly increasing is where the level of inward convection is closer to zero, then the density starts peaking strongly as the inward convection becomes stronger for  $\rho < 0.6$ . Since the convection points outwards for  $\rho > 0.8$ , a valley is created between  $\rho = 0.6$  and  $\rho = 0.9$ , as carbon particles are transported towards the edge on the

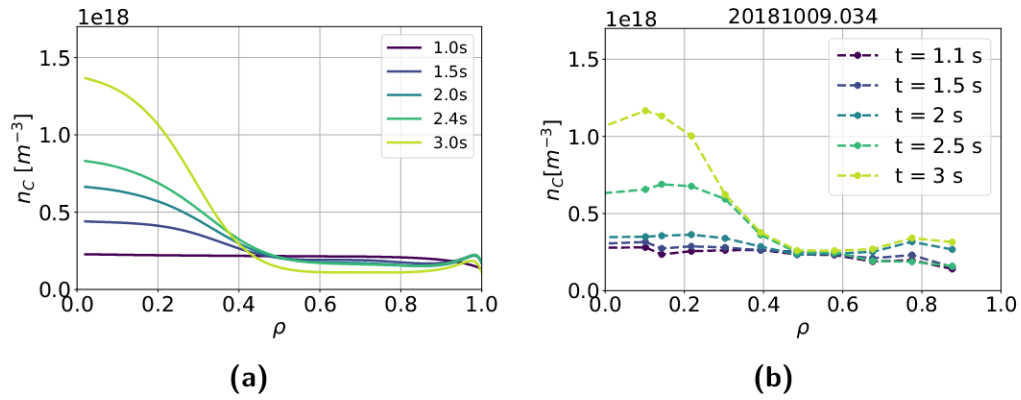


**Figure 3.23.:** Simulated carbon density profiles assuming neoclassical transport only (a) and experimentally obtained carbon density profiles (b) from the example time points during the NBI phase of discharge 20181009.034. The peaking behaviour agrees for  $\rho < 0.5$ . However, the neoclassical profiles decrease for  $\rho > 0.5$  during NBI operation, creating a small valley, which is not consistent with the experimental profiles.

right side and towards the core on the left side. This behaviour is not seen in the experiment. This valley is less pronounced than the peak in the core, as the acting convection velocity is weaker on both sides of the valley than in the plasma core.

The neoclassical convection becomes stronger with time during the NBI operation as the background plasma properties change. Therefore the valley becomes more defined for later time points. Figure 3.24a shows the time evolution of the simulated neoclassical carbon density from three different relevant radial ranges, one from the core, one from the range where the peaking becomes prominent, and one from the middle of the valley. This valley is not observable in the experimental carbon density profiles. The time evolution of the experimental density from the same three radial ranges can be seen in Figure 3.24b. The experimental density level does not change for  $\rho > 0.6$  throughout the whole NBI operation. The noisiness of the time trace for this region is higher than for the other two more inner regions, because the separation of the active and passive component is less trivial for lower temperatures, as discussed in Section 3.1.2.

Considering the difference between the neoclassical and experimental  $n_c$  profiles, it is evident that the experimental transport has an anomalous

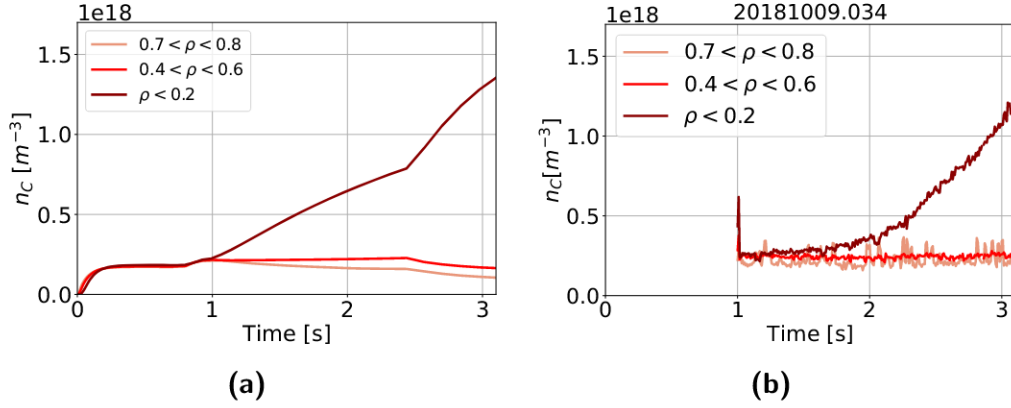


**Figure 3.24.:** Time evolution of the simulated carbon density with purely neoclassical transport (a) and of the experimentally obtained carbon density (b) during the investigated phase of discharge 20181009.034. The simulated constant time trace during the ECRH phase is also displayed. The time evolution of the simulated and experimental profiles is displayed for three radial regions:  $\rho < 0.2$ ,  $0.4 < \rho < 0.6$  and  $0.7 < \rho < 0.8$ . The neoclassical density decreases outside of half radius, while the neoclassical and experimental core densities increase to a similar level, although with different growth rate throughout the investigated time range.

component that keeps the profile flat at  $\rho > 0.5$ . While an anomalous convection could theoretically counteract the neoclassical convection, this would have to be carefully tailored to produce a flat carbon density profile in this region. A far simpler solution is the presence of anomalous diffusion, based on the strong turbulent diffusion seen in ECRH dominated plasmas [89], that counteracts the effects of the neoclassical convection in this region. Additionally, no such anomalous convection was observed in the previous ECRH studies. Therefore, anomalous diffusion is added to the outer half of the confined region in the simulation of the NBI phase. The diffusion at  $\rho < 0.5$  stays neoclassical to keep the accumulation observed with the neoclassical values, as this already agreed relatively well with the measured profiles. At  $\rho = 0.5$ , smoothing is used to make the transition of the two different assumed regimes more realistic. The convection velocity was kept at the neoclassical value for the whole radius, in accordance with previous studies on W7-X in anomalous transport regimes [89]. The profiles of the

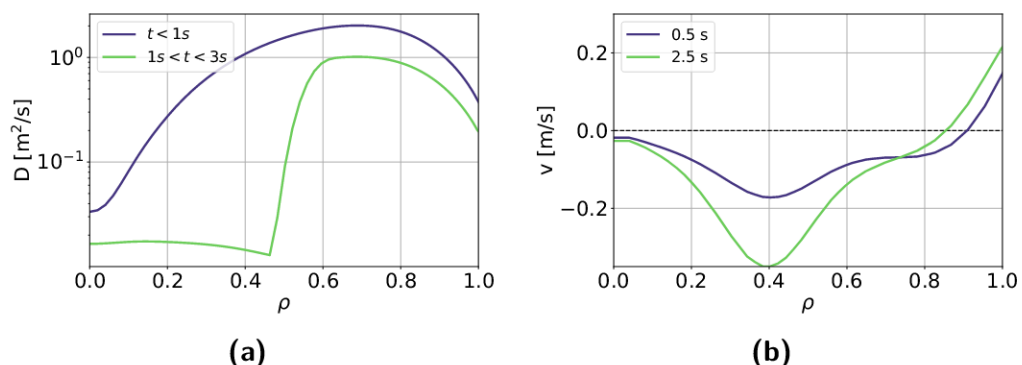


**Figure 3.25.:** Anomalous diffusion (a) and neoclassical convection velocity (b) as used in the simulation of the NBI phase assuming two different transport regions (green). The diffusion is kept at neoclassical levels at  $\rho < 0.5$ , as in the fully neoclassical simulation, and has a strong anomalous component at  $\rho > 0.5$ . The anomalous diffusion and neoclassical convection velocity profiles used in the ECRH phase (as shown in Figure 3.21) are displayed for comparison (purple).

chosen transport coefficients are shown in Figure 3.25 together with the transport coefficients of the ECRH phase.

Figure 3.26a shows the carbon density profiles resulting from this simulation, with the experimental profiles displayed in Figure 3.26b as comparison. The newly obtained simulated density profiles do not have a valley-like shape at  $\rho > 0.5$ , as the strong diffusion there flattens out any density gradient created by the convection. As a result, the carbon density stays the same for the investigated length of the NBI phase, which agrees with the experiment. The diffusion is insignificantly low at  $\rho < 0.5$  compared to the convection, as in the purely neoclassical simulation, therefore the convection continues to dominate this region, and the carbon density rises, creating a peak. This also agrees with the experiment. In the presented case, the anomalous diffusion outside of half radius is half the level of the anomalous diffusion of the ECRH phase. A range of anomalous diffusion levels are investigated to determine the range which makes the simulated profiles match the experimental ones the best. The valley seen in the neoclassical  $n_C$  profiles stays visible, if the diffusion is lower than presented. In the case of higher diffusion, more comparable with the level seen in the ECRH phase,

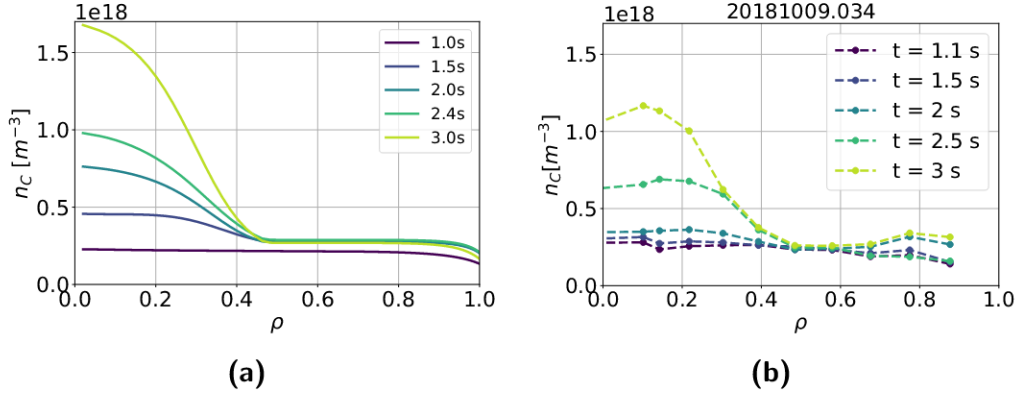


**Figure 3.26.:** Simulated carbon density profiles with neoclassical diffusion at  $\rho < 0.5$ , and anomalous diffusion at  $\rho > 0.5$  (a) from the example time points of discharge 20181009.034 with the experimental profiles from the same time points for comparison (b). There is no valley appearing outside of half radius, while the peaking in the core is still observable, which agrees with the experimental profiles better than the purely neoclassical simulation.

the start of the peak at  $\rho \approx 0.5$  is more defined, it takes an inflection point like shape. The transition from the flat carbon density outside of half radius to the peak inside half radius is smoother than that in the experimental profiles. Thus, the anomalous diffusion outside half radius was determined having to be  $50 \pm 10\%$  of the anomalous diffusion of the ECRH phase to produce the best fitting to the  $n_c$  profiles. It is important to note that the exact value of the simulated anomalous diffusion outside of half radius is not significant, as long as it is dominant over the neoclassical diffusion level (orders of magnitude higher).

The time evolution of the simulated carbon density profiles using these parameters discussed above, as shown in Figure 3.27a, is comparable to the time evolution of the experimentally obtained profiles shown in Figure 3.27b. The simulated and experimental time traces match well in the outer and middle region, as the density does not change in the outer region, and only marginally increases in the middle region as the peaking starts there radially smoothly. However, the growth rate in the core, and thus the shape of the two time traces does not fully match and the simulated carbon density begins rising earlier. The difference between the level of the

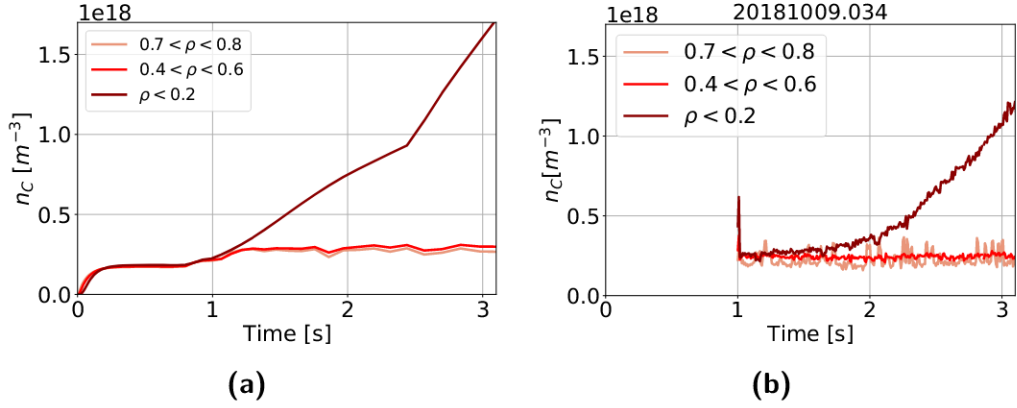


**Figure 3.27.:** Time evolution of the simulated carbon density with neo-classical diffusion at  $\rho < 0.5$ , and anomalous diffusion at  $\rho > 0.5$  (a) of the investigated phase of discharge 20181009.034 with the experimental time evolution displayed for comparison. Three radial regions are shown:  $\rho < 0.2$ ,  $0.4 < \rho < 0.6$  and  $0.7 < \rho < 0.8$ . The growth rate and the shape of the time trace for the simulated and experimental carbon densities does not fully agree in the core, the simulated density rises higher within the given time range. The time traces agree well for the other radial regions.

density peak at the start of the NBI operation ( $t = 1$  s) and at the end of the NBI operation ( $t = 3$  s) is in the same order of magnitude for the simulated and experimental profiles, but differences are observable. The experimental density peaking starts rather slowly after the NBI is switched on, as shown earlier (see  $t_{onset}$  in Section 3.2.3). This behaviour does not appear in the simulated density. This suggests that the diffusion profile is not purely neoclassical inside half radius throughout the whole NBI operation, especially immediately after  $t = 1$  s.

The growth rate of the simulated density matches the growth rate of the experimental density after  $t_{onset}$ , thus at  $t > 2$  s. In the two presented simulations, the anomalous diffusion in the core, as observed in the ECRH phase, is set to drop to neoclassical levels immediately after the NBI heating is turned on. Considering that this drop in the core diffusion happens on a slower time scale in reality, the rate of the density peaking at the beginning of the NBI phase could be slower. It is assumed that the time scale the

### 3.2. Investigation of carbon transport in the plasma core

---

core diffusion needs to reach neoclassical levels is correlated with  $t_{onset}$ , and therefore happens within  $t = t_{onset} \approx 1$  s. To investigate which physical process or quantity determines the rate with which the anomalous diffusion decreases in the core after the NBI is turned on, the changes in the background plasma parameters are considered when the heating switch happens. Changing from ECRH to NBI heating has a close to immediate effect on both the electron and ion temperature, as they drop  $\approx 10 - 100$  ms after the NBI is turned on, in accordance with the energy confinement time that determines the heat transport. The core electron density is affected on a longer time scale, as the particle confinement time is longer than the energy confinement time, resulting in a slower particle transport. The peaking rate of the core  $n_e$  does not change significantly until  $\approx t_{onset}$ . This suggests that the changes in the anomalous diffusion, and thus the reduction of turbulence in the plasma core is correlated to the electron density, and not to the temperatures. This would be conceptually consistent with observations of reduced turbulent heat transport in the presence of strong density gradients [101]. Investigations of the turbulence theory and mechanisms is beyond the scope of this work.

To validate the assumed neoclassical nature of the core transport, an anomalous diffusion scan is done. The core anomalous diffusion is set to 100 different values within  $S = 0 - 1$ , where  $S$  is a scaling factor that is used for the core anomalous diffusion seen in the ECRH phase.  $S = 1$  means 100% of the anomalous diffusion required to explain the carbon density profiles in the ECRH phase, and  $S = 0$  means no anomalous diffusion, thus fully neoclassical transport. The time evolution of each simulated core carbon density (for  $\rho < 0.2$ ) with different  $S$  values is shown in Figure 3.28a. A gradient of the  $C^{6+}$  density is calculated to be compared in the different core diffusion scenarios. The average density is calculated for  $\rho < 0.2$  ( $n_C^{av}(\rho = 0.1)$ ) and for  $0.7 < \rho < 0.8$  ( $n_C^{av}(\rho = 0.75)$ ) and the gradient is defined according to Equation 3.30.

$$\nabla(n_C) = \left| \frac{n_C^{av}(\rho = 0.1) - n_C^{av}(\rho = 0.75)}{0.1 - 0.75} \right| \quad (3.30)$$

$\nabla(n_C)$  at  $t = 2.5$  s is displayed against the scaling factor in Figure 3.28b. No significant peaking can be observed for core diffusion coefficients higher than  $\approx 5\%$  of the original anomalous diffusion. If the core diffusion is between  $0 < S < 0.05$  (set not to reach neoclassical levels), then there

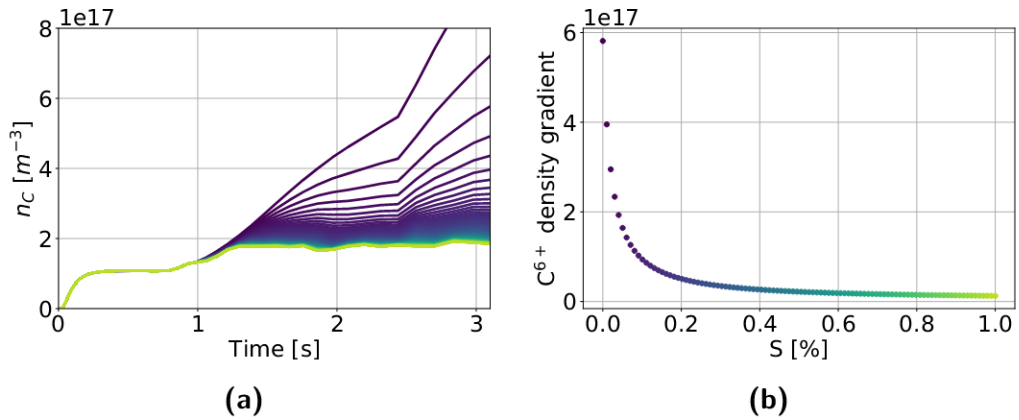


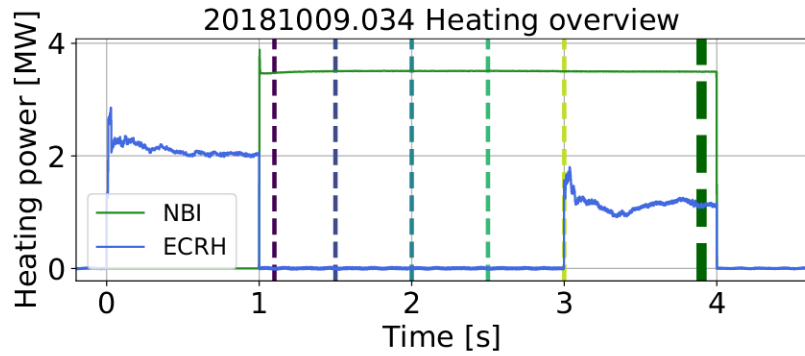
**Figure 3.28.:** Core carbon density time evolution with different core anomalous diffusion level (a). Carbon density gradient as a function of the scaling factor for the core anomalous diffusion (b), showing no significant peaking with high core anomalous diffusion.

is an observable peak in the core, but not as pronounced as seen in the experiments and not producing the increase in core carbon density seen throughout the pure NBI phase. Thus, it is concluded that without the core diffusion dropping to neoclassical levels within a certain time after the NBI is turned on, the core carbon density cannot reach the high values seen in the experiments.

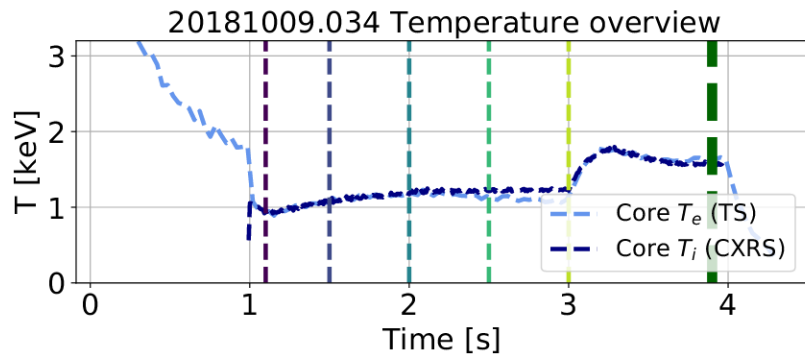
### 3.2.5. Carbon density in plasmas with combined ECRH and NBI heating

In the last phase of discharge 20181009.034, at  $3 \text{ s} < t < 4 \text{ s}$ , a relatively low O2 ECRH power was turned on in addition to the previously pure NBI heating. The behaviour of the plasma and specifically of the carbon is discussed in this section.

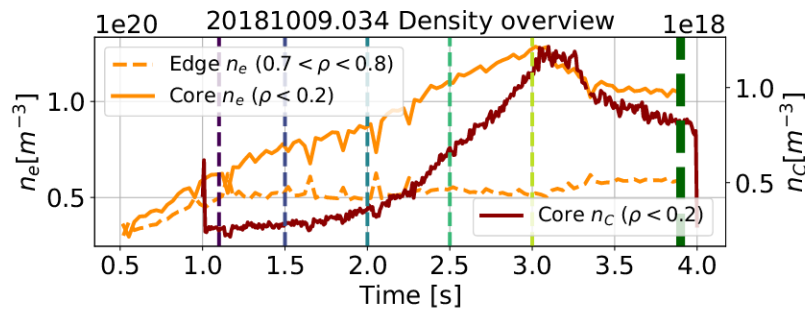
The addition of the ECRH power has a significant effect on all investigated quantities. The time evolution of the global parameters as well as of the carbon density is displayed in Figure 3.29 for the whole discharge as in Figure 3.18, with an additional example time point indicated in the mixed heating phase. The time evolution of the heating power corresponding to both heating systems can be seen in Figure 3.29a. The electron and ion



(a)



(b)



(c)

**Figure 3.29.:** Global parameters of discharge 20181009.034 with an example time point highlighted in the last, NBI dominated phase with low level ECRH. Time trace of the ECRH power in blue and the NBI heating power in green (a). Time trace of the core electron temperature in light blue and the core ion temperature in dark blue (b). Time trace of the core electron density in orange with solid line, the electron density outside of half radius in orange with dashed line and the core carbon density obtained from the CXRS signal in red (c).

temperature shown in Figure 3.29b start rapidly rising as soon as the ECRH is added again. After reaching a maximum at  $T_i = T_e = 1.8$  keV, 200 – 250 ms into the mixed heating phase, they both decrease marginally, keeping their level afterwards for  $\approx 600$  ms until the end of the discharge. This makes this plasma phase a higher performance scenario in terms of the ion temperature than the pure NBI or standard ECRH dominated phase.  $T_i$  rises above its limit (1.6 keV) observed in standard gas-fuelled ECRH discharges with high heating power. The  $T_i$  limit is presumably not present in pure NBI cases, but  $T_i$  is still observed to be around 1 keV, due to the combination of high  $n_e$  and low heating power. Apart from the presented mixed heating scenario (low ECRH power and higher NBI heating power),  $T_i > 1.6$  keV was achieved in pellet-fuelled ECRH dominated plasmas (see Section 3.2.6) and gas fuelled ECRH dominated plasmas with very low heating power. The electron density shown in Figure 3.29c also reacts immediately to the added ECRH. The core density starts decreasing while the edge density increases, making the  $n_e$  profile less peaked. Both the core and edge  $n_e$  changes are small. The core density is still at relatively high level ( $\approx 10^{20}$  m<sup>-3</sup>) by the end of the discharge.

The typical carbon density is shown in Figure 3.30 for the example time point of this phase indicated in Figure 3.29, along with the example carbon density profiles from the ECRH and NBI phase earlier in the discharge, as a comparison. The carbon density stops increasing in the core after  $t = 3$  s, but it keeps its maximum peak for around 250 ms. After this period, the core carbon density flattens out, while a high gradient remains at  $0.4 < \rho < 0.5$ . The density outside of half radius stays the same, as it did throughout the whole discharge. The profile shape with the flat core and the high gradient at half radius remains for 500 – 600 ms. Only the core density level decreases marginally. The plasma is terminated at  $t = 4$  s for technical reasons. There is no indicator to determine how long this density state and the corresponding transport conditions would remain.

If the core of the plasma would remain dominated by neoclassical effects, as during the pure NBI phase, the carbon density peaking in the core would remain and would continue to rise. The disappearance of the peak suggests that an anomalous component appears that flushes out the carbon from the plasma core. It is likely that turbulence becomes dominant again in the core. However, the carbon transport still seems to be dominated by neoclassical effects in the region around half radius, without significant

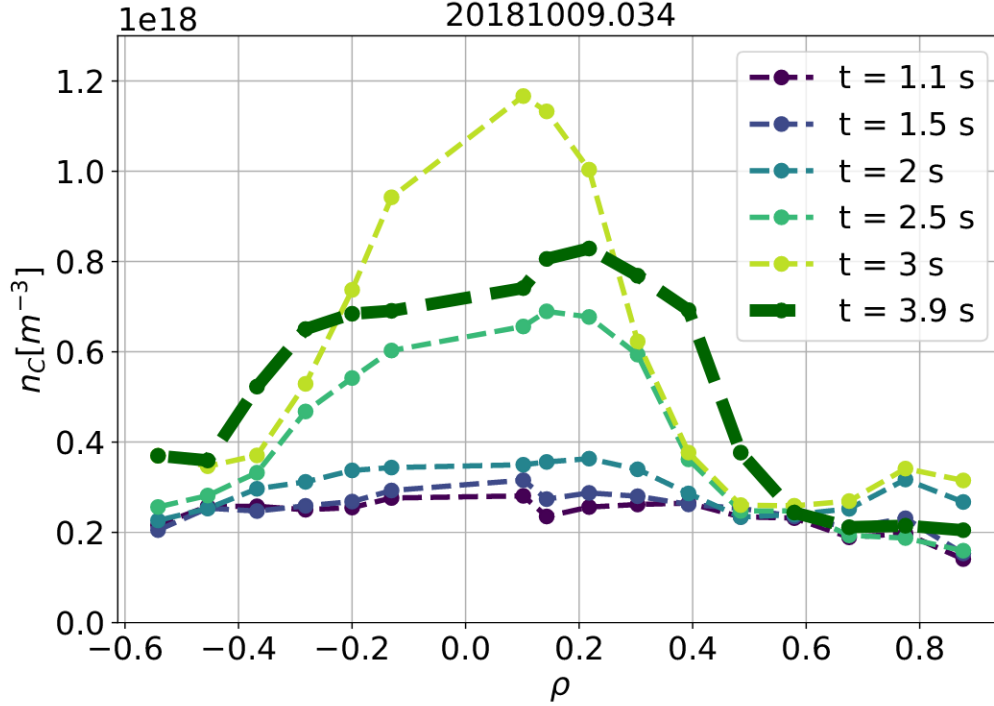


**Figure 3.30.:** Carbon density profiles from the selected time points of discharge 20181009.034. The colour of the profiles match the time points highlighted in Figure 3.29 with the time point in the mixed heated plasma phase highlighted.

enough anomalous diffusion to remove the gradient maintained by inward neoclassical convection.

The causalities of the changes induced by the additional ECRH are not yet established and need further investigation. The core carbon density does not drop in the first 200 – 250 ms of the phase with NBI and ECRH, unlike the global parameters, which suggests that the changes in the carbon transport might be caused by the behaviour of the temperatures or the electron density.

The combined application of ECRH and NBI shows some advantages to the pure NBI heated phase in terms of impurity accumulation. The reduced carbon density peak in the core does not affect the plasma power balance as negatively as the observed strong accumulation during the pure NBI

phase. No data was recorded in a scenario like this for longer than 1 s, so it is unknown how long the shape of the carbon density profile, as well as the corresponding transport properties, can be maintained. However, as the scenario has some clear benefits, the energy, particle and impurity confinement will be explored in detail for longer time periods in future measurement campaigns.

### 3.2.6. Carbon density in pellet induced high performance plasma scenarios

The criteria for self heating fusion operation states that the triple product (see Section 1.1) should be above a critical value. The triple product is therefore calculated for experimental fusion devices in order to assess how efficient different plasma and heating scenarios are regarding plasma performance. Up to now, the achieved triple product in all current and past experimental fusion devices is below the required threshold. Nonetheless, as research gains more and more understanding of fusion plasma physics, the highest achieved triple product is generally increasing in newer devices compared to older ones.

The highest achieved triple product of a stellarator is reported to be achieved in W7-X during the measurement campaign OP1.2a in the pellet induced high performance phase of discharge 20171207.006 [67]. The reported triple product value is  $\approx 6.1 * 10^{19} \text{ m}^{-3} \text{ keV s}$ . The previously established record for stellarators was achieved at the LHD stellarator in Japan at  $5.2 * 10^{19} \text{ m}^{-3} \text{ keV s}$  [102]. The record triple product value of LHD was achieved in a significantly different plasma scenario than in W7-X, at lower ion temperature that is not relevant for future fusion reactors.

The concentration of impurities in the plasma affects the plasma performance and therefore the triple product. The ion density is needed to calculate the triple product, however, it is not directly measured. It is possible to revise the definition of the triple product in a way, that electron density, which is directly measured by the Thomson Scattering diagnostic, is used instead of the ion density, as shown in Equation 3.31. In Equation 3.31, the energy confinement time is also expressed by quantities that are directly measured at W7-X, namely the diamagnetic energy ( $W_{dia}$ ) and heating power ( $P_{heating}$ ).

$$n_i T_i \tau_E = \frac{n_i}{n_e} T_i \frac{W_{dia}}{P_{heating}} \quad (3.31)$$

If no impurities were present in the plasma, the electron and ion density would be the same, as all the electrons would originate from hydrogen isotopes. This maximises the triple product value for a given plasma, as equal electron and ion densities mean that their fraction is exactly one. However, with impurities present, electrons from impurity ions are added to the electron population of the plasma, which results in  $n_i < n_e$  and a lower triple product. Therefore, the impurity content is needed for the calculation of the triple product.

The amount of different impurities is taken into account in the effective ion charge as described in Section 1.4 and again in Equation 3.32.

$$Z_{eff} = \frac{\sum_j n_j Z_j^2}{\sum_j n_j Z_j} \quad (3.32)$$

The record triple product reported at W7-X was calculated with an estimation of  $Z_{eff} = 1.5$ . However, the density of intrinsic impurities was not directly measured in the confined plasma during the reported measurement campaign due to the lack of suitable diagnostics. Core impurity density measurements were provided in the next campaign, OP1.2b, by the CXRS diagnostic. In this section, a simple triple product estimation is provided by taking the measured carbon concentration levels into account for the high performance plasma scenarios.

Plasma phases that provide sufficient conditions for higher performance, including higher  $n_e$  and  $T_i$ , as well as  $W_{dia}$ , can be achieved by continuous hydrogen pellet injections into the plasma core [101] [40]. During the pellet injection phase, the core electron density is heavily peaking and increasing to sometimes ten times higher values than before the pellet injection phase. Immediately after the pellet injection stops, a reduction in turbulence [103] [104] and a rise in the ion temperature and the diamagnetic energy is observed [105]. These properties provide the highest triple product value obtained at W7-X. The high performance phase is usually maintained for  $\approx 0.5$  s.

Two successful high performance discharges are chosen for the analysis of the impurity content, 20181016.037 and 20180918.045. Both have a plasma

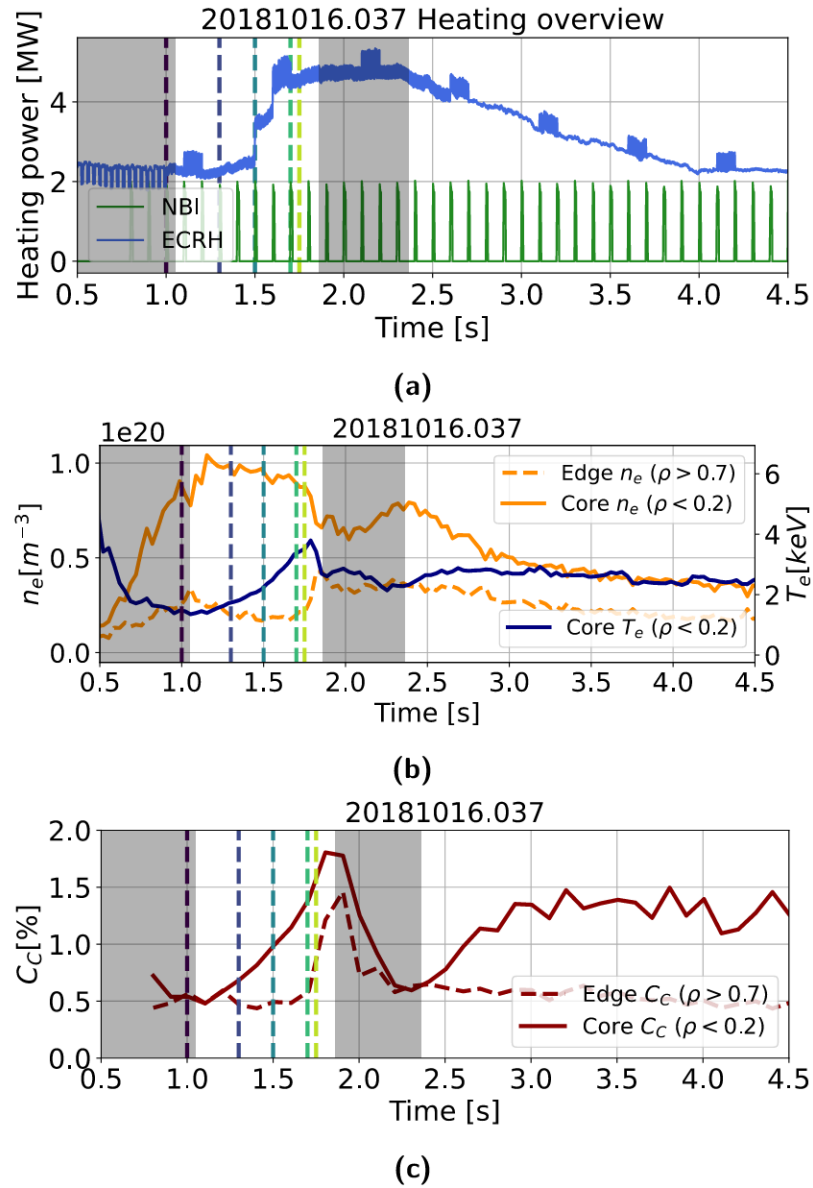


**Figure 3.31.:** Time evolution of relevant parameters for discharge 20181016.037. Time trace of the ECRH power (blue) and NBI heating power (green) (a). Time trace of the electron density (b) and the  $C^{6+}$  concentration (c). The latter two quantities are displayed for the plasma core ( $\rho < 0.2$ ) with solid orange and dark red lines and for the plasma edge ( $\rho > 0.8$ ) with dashed orange and dark red lines, respectively. The two continuous pellet injection phases are indicated with grey areas in the figures. The high performance phase takes place around  $t = 1.7$  s.

parameter evolution similar to the reported record discharge from OP1.2a. Therefore, both achieved similar triple products as the reported record discharge. The time evolution of the electron density of discharge 20181016.037 is displayed in Figure 3.31b. In this discharge, two continuous pellet phases were carried out, as indicated in the corresponding figures. However, only the first pellet phase was followed by a high performance phase. Fifty-one 10 ms long NBI blips were carried out during discharge 20181016.037 with  $\approx 90$  ms between them to ensure that the NBI heating does not contribute significantly to any plasma parameter evolution as that was not the intention of the investigated plasma experiment. The time between the NBI blips acts as a limit of the time resolution of the impurity analysis, as only one impurity density profile can be calculated for each blip.

Measurements were done with the CXRS diagnostic during these high performance plasma phases on several impurities with the available range of spectrometers. The measurements of impurities, apart from carbon measurements by the *ILS* spectrometer, were not yet fully analysed by the time of this analysis, therefore no absolute density or concentration value is available for impurities apart from carbon. Simple investigations were done on the intensity of oxygen measured by the *AUG - 2* spectrometer, to obtain information of the general behaviour of its density during the plasma phases in question.

Both carbon and oxygen show the same temporal behaviour during and after the pellet injection phase. The time evolution of the carbon concentration at the plasma core and at the plasma edge is shown in Figure 3.31c. It marginally decreases ( $\approx 20\%$ ) during the continuous pellet injection, which is consistent with the expectation that pellets introduce additional hydrogen into the plasma, making it less diluted assuming that the absolute amount of impurities does not increase. After the pellet injection stops, the carbon concentration strongly increases in the core, which means a lower achieved triple product, providing an additional motivation to look deeper into the behaviour of this discharge.

Due to a specific setting of the  $C^{5+}$  camera, the signal to noise ratio of the carbon intensity is lower for the investigated high performance discharges than for other standard ECRH or NBI heated plasmas. As a result, the obtained carbon density profiles are noisier, especially for the data from the High Field Side (HFS) where the beam attenuation leads to a further decrease of the signal, making the separation of the active and passive com-

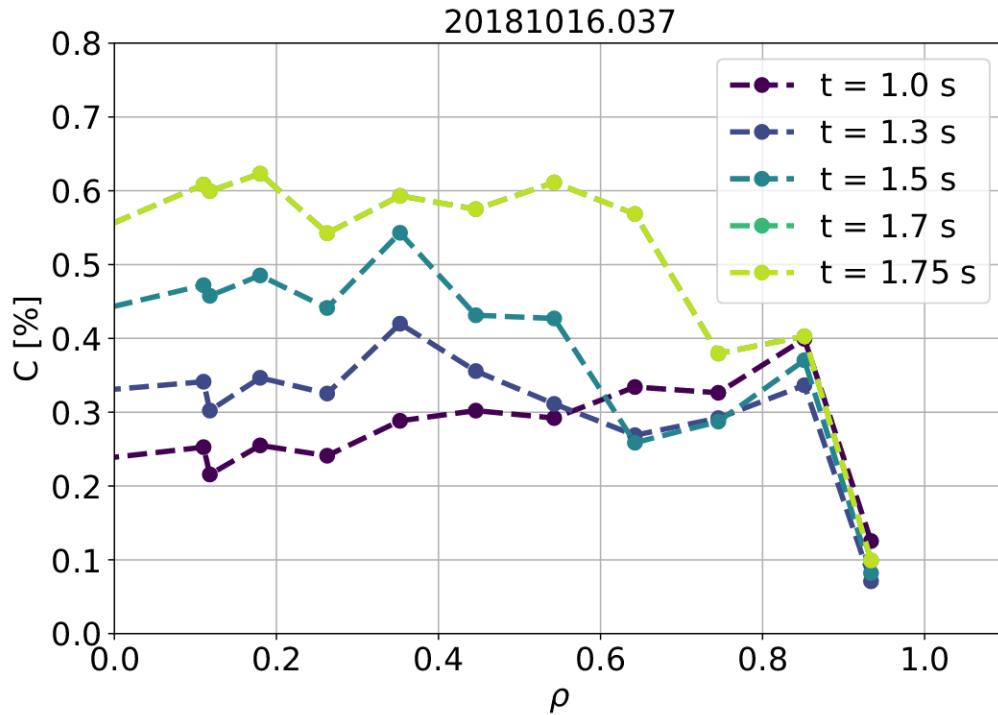


**Figure 3.32.:**  $C^{6+}$  concentration profiles of discharge 20181016.037 for selected example time points. The first time point is taken at the end of the first pellet phase, before the high performance phase. The rest of the time points are taken every 0.2 s of the the high performance phase where the core concentration increases, until the time point with the highest core concentration.

ponents more difficult. The calculated carbon density profiles for discharge 20181016.037 can be seen in Figure 3.32.

Neutral beam and halo density simulations by the FIDASIM code are not available for pellet induced high performance discharges at W7-X by the time of this analysis, therefore the halo contribution to the CXRS signal cannot be precisely calculated for these discharges. Instead, a halo contribution of 40% to the full intensity is assumed for the given plasma and beam parameters according to [79]. This is applied for the carbon density profiles shown in Figure 3.32.

Before and during the pellet injection phase, the carbon density profile is

### 3.2. Investigation of carbon transport in the plasma core

---

flat throughout the whole plasma radius within  $\rho < 0.9$ , as seen earlier in the standard ECRH discharges. Immediately after the pellet injection phase, as  $T_i$  and  $W_{dia}$  are rising, the core carbon density starts rising as well. In the next about 0.5 s, a gradient appears at  $\rho \approx 0.6$ , with the profile rising inside this radial location while staying flat. The shape is similar to the carbon density profile shape observed in plasmas with low levels of ECRH added to pure NBI heating (see Section 3.2.5). Although the scenario is considerably different, the mechanism for the carbon accumulation is likely the same. In this case, the steep electron density gradient is at  $\rho \approx 0.6$  and leads to suppressed turbulence as seen in the heat fluxes [103] [104], so a similar reduction of the turbulent diffusion impurity transport coefficient in this region is expected. Approximately 100 ms before the core carbon density reaches its maximum, it also rises outside of  $\rho \approx 0.6$ . This seems to suggest that the amount of carbon that is present in the plasma increases significantly. An increase in the outer flux surfaces (outside of half radius) can only be caused by a significantly larger number of carbon particles present, as the plasma volume covered by the outer flux surfaces is greater than that of the core flux surfaces.

The highest performance phase lasts about 0.6 s, starting after the pellet injection is terminated at  $t = 1.1$  s. The triple product is calculated at  $t = 1.75$  s, which marks the highest carbon concentration within the high performance phase. Table 3.3 lists the relevant plasma parameters observed at this time point.

The effective charge, first assuming that carbon is the only impurity in the hydrogen plasma, is  $Z_{eff} = 1.17$ , according to Equation 3.32. In this case, the electron density is higher than in a pure hydrogen plasma scenario, taking into account that fully ionised carbon ions contribute with six electron to the electron population. This results in  $n_e > n_i$  and  $n_i/n_e = 0.97$ .

Thus, the resulting triple product for the described plasma is  $n_i T_i \tau_E = 6.26 * 10^{19} \text{ m}^{-3} \text{ keV s}$ , compared to  $n_i T_i \tau_E = 6.46 * 10^{19} \text{ m}^{-3} \text{ keV s}$ , which would be calculated if the impurity content was ignored.

As, in fact, carbon is not the only impurity present in the plasma, this overestimates the triple product. The analysis is extended to oxygen, the second most common intrinsic impurity in the W7-X plasma. Because of the lack of absolute oxygen density values, it is assumed that oxygen has the same concentration as carbon. As in reality the density of oxygen is likely lower than the density of carbon, this assumption underestimates the

**Table 3.3.:** Plasma parameters of discharge 20181016.037 at  $t = 1.75$  s, when the high performance phase took place.  $P_{heating}$  refers to the ECRH power,  $W_{dia}$ ,  $T_i$  and  $n_e$  are measured by the magnetic diagnostic system [5], the XICS diagnostic and the Thomson Scattering diagnostic, respectively.  $C_C$  refers to the concentration of  $C^{6+}$  ions measured by the *ILS* spectrometer of the CXRS diagnostic.

<b>Heating power (<math>P_{heating}</math>)</b>	4.65 MW
<b>Diamagnetic energy (<math>W_{dia}</math>)</b>	1.14 MJ
<b>Ion temperature (<math>T_i</math>)</b>	3.08 keV
<b>Electron density (<math>n_e</math>)</b>	$8.55 * 10^{19} \text{ m}^{-3}$
<b>Carbon concentration (<math>C_C</math>)</b>	0.60%

calculated triple product so much that this presumably compensates for any other impurity present in the plasma. With 0.6% carbon concentration and 0.6% oxygen concentration, the effective atomic number is  $Z_{eff} = 1.48$ . The change in the electron density results in  $n_i/n_e = 0.93$ .

As a result, the triple product is  $n_i T_i \tau_E = 6.00 * 10^{19} \text{ m}^{-3} \text{ keV s}$ .

It can be concluded that core impurity density measurements support the previously reported record triple product for stellarators in [67] that assumed  $Z_{eff} = 1.5$  in the lack of such measurements at the time. The calculated triple products for high performance plasma phases similar to the reported record discharge are all above the previous record of the LHD stellarator.

# Chapter 4.

## Conclusions

Properties of carbon were investigated with two measurement systems at the Wendelstein 7-X (W7-X) stellarator. The installation and calibration of both systems, as well as the measurements themselves were carried out during the scope of this work. The Passive Spectroscopy system measures line integrated intensity of carbon ions and therefore, an inversion was needed to obtain spatial information on the carbon density distribution. The inversion process requires strong assumptions about the radial form of the emission which may not be valid in all cases. The Active Spectroscopy system (Charge Exchange Recombination Spectroscopy, CXRS) is able to measure the carbon density profiles directly with the help of the NBI as a local source of neutral particles for the charge exchange process. Without the need for an inversion, the carbon density profiles can be derived with more reliable assumptions. The need for absolute calibration to obtain real carbon density values can be eliminated by cross calibration with a carbon and a  $H_\alpha$  camera in the same spectrometer, which is the case in the Active Spectroscopy diagnostic at W7-X. The calculation of carbon densities with the cross calibration method has been established and validated for the CXRS system at W7-X.

Both diagnostic systems measured the radiation of the  $C^{5+}$  spectral line at 529.06 nm.  $C^{5+}$  ions are usually present in the confined plasma towards the plasma edge, this is where the radiation measured by the Passive Spectroscopy system comes from. When the NBI neutrals penetrate the plasma,  $C^{6+}$  ions become  $C^{5+}$  via charge exchange and their radiation is additionally detected by the Active Spectroscopy system, besides the passive emission. As in the plasma core and over most of the plasma radius  $C^{6+}$  is the only form of carbon that is present without NBI operation due to the high tem-

peratures, only the Active Spectroscopy system is able to measure what the Passive Spectroscopy and other diagnostic systems cannot. Hence this system can be used to study carbon transport over a large fraction of the plasma cross-section. Investigating the impurity transport in the plasma core is crucial for understanding the impurity behaviour and for finding conditions optimal for high plasma performance.

Through the analysis of the Passive Spectroscopy system, it has been shown that a flux surface based one dimensional radial profile of the  $C^{5+}$  emission intensity can be obtained through inversion from the measured two dimensional signal (neglecting the width of the lines of sight). Investigations of the radial distribution of  $C^{5+}$  showed that these ions have two main sources with distinct, separable radial locations ( $\rho_1 = 0.7 - 0.8$  and  $\rho_2 = 0.9 - 1$ ). The two physical processes involved are charge exchange of  $C^{6+}$  ions with thermal neutrals and electron impact excitation of  $C^{5+}$  ions. Neither of these processes would be expected to produce emission at the observed inner source position under local corona equilibrium assumptions. However, radiation calculations by the STRAHL transport simulation code shows that the inner source can be explained by electron impact excitation, if the  $C^{5+}$  ions are transported into the plasma more rapidly than the life time of this ionisation stage at the observed temperatures. Such rapid transport is consistent with high turbulent diffusion seen outside of half radius in the analysis on carbon density from the Active Spectroscopy system in this work as well as in other work [89]. This supports the conclusion that the inner source of  $C^{5+}$  ions measured by the Passive Spectroscopy system is electron impact excitation. The Passive Spectroscopy system remains important in the future for following the behaviour of  $C^{5+}$  ions. It was also discussed how the thermal neutral density might be derived from the  $C^{5+}$  results of the Passive Spectroscopy.

The spatially resolved carbon density profiles measured by the Active Spectroscopy system and the corresponding carbon transport properties were analysed for different heating scenarios: standard ECRH dominated and pure NBI heated plasma phases. Mixed heated scenarios with low level ECRH power, as well as ECRH dominated plasmas with continuous hydrogen pellet injection were investigated in addition without a transport simulation. The aim of the analysis was to investigate which physical processes dominate the carbon transport in different plasma scenarios and to understand the optimal conditions for favourable carbon, or more broadly,

---

low-Z impurity transport.

Strong turbulent carbon transport is found in gas fuelled ECRH dominated discharges with high diffusion levels. This work presented the first evidence that in pure NBI heated plasma phases, the carbon transport is dominated by neoclassical diffusion and convection in the plasma core, creating strong and growing carbon accumulation. This accumulation can negatively affect plasma performance, depending on the amount of accumulated impurity particles. It was found that while turbulence is strongly suppressed in the core, strong anomalous diffusion must still be present outside of half radius in order to explain the observed profiles.

In plasmas heated with NBI and low levels of ECRH, the carbon transport in the very core is observed to be turbulence dominated without strongly peaked carbon density profiles. However, the turbulent transport seems to remain reduced at radial regions around half radius. Similar carbon profile shapes were found in pellet fuelled ECRH plasmas during the high performance phase with ion temperatures and electron densities which provide the highest achieved triple product values at W7-X. While turbulence is suppressed in some radial regions, which seems to be favourable in achieving higher performance plasmas, the carbon density profile is flat in the core presumably due to core turbulent carbon transport. This is also favourable for reactor-like plasmas, as it reduces dilution and radiation losses due to impurities in the core.



# Chapter 5.

## Outlook

The  $C^{5+}$  signal measured by the Passive Spectroscopy system could be additionally important in a future diagnostic setup for measuring the passive background component during NBI operation as a support for the CXRS system. This would allow direct subtraction of the passive component from the spectra measured by the CXRS, providing more accurate active and passive component separation than the method used for the analysis presented here.

The estimation of thermal neutral density from Passive Spectroscopy data presented in this work relies on neoclassical assumptions that may not be valid, especially in ECRH dominated plasmas, but it demonstrates that the neutral density could be determined with an absolute calibration, a full STRAHL analysis and combination with the Active Spectroscopy. This is particularly encouraging given that the neutral density is a critical quantity that is not directly measured by any other diagnostic in the confined plasma region at W7-X.

The carbon transport analysis based on the CXRS measurements could be improved and extended in a few ways. To increase the flexibility of the determination of anomalous diffusion profiles for carbon, a detailed fitting could be done, where the anomalous diffusion profile is systematically changed to fit the thus-calculated carbon density profiles to the experimental profiles. Additionally, the transport simulation could be carried out for experimental plasma phases with mixed heating to investigate the radial transport ranges of the carbon density profiles with a flat core and a gradient at half radius. Investigation of plasma experiments with carbon injection into pure NBI heating ([57] [56]) are also of interest. The time scale of their effects on the carbon density is short enough to enable a time dependent transport analysis without the need for assumptions on the temporal evolution of the

anomalous diffusion as seen in this presented work.

The presented mixed heating scenario is promising for achieving a stable high performance plasma phase without strong impurity accumulation in the plasma core. A mapping of different ECRH power levels added after a few seconds long pure NBI phase with different NBI heating power levels could determine the most favourable heating ratio for W7-X considering core impurity transport (flat core density) and plasma performance (ion temperature that is well above the ECRH induced  $T_i$  limit).

# Appendix A.

## Acknowledgements

This work has been carried out within the framework of the EUROfusion Consortium, funded by the European Union via the Euratom Research and Training Programme (Grant Agreement No 101052200 — EUROfusion). Views and opinions expressed are however those of the author(s) only and do not necessarily reflect those of the European Union or the European Commission. Neither the European Union nor the European Commission can be held responsible for them.

This PhD work would not have been possible without the support and help of many people. I would like to thank Prof. Robert Wolf for the opportunity for this PhD in Greifswald at W7-X and for guiding me through the years. I could not have asked for a better work environment or a more interesting topic. A huge gratitude goes to Dr. Oliver Ford for all the guidance, easily understandable explanations and never-ending kindness he showed me. Thank you for your deep enthusiasm towards fusion plasma physics and for the good company in the meantime. Thank you to Dr. Benedikt Geiger and Colin Schwee for sharing your knowledge on the impurity transport code pySTRAHL, providing detailed instructions and help to work with it. I would like to thank all colleagues who helped me with fruitful conversations and ideas, providing a broader view on the topics we are working on. Including, but not limited to, these colleagues are Dr. Victoria Winters, Frederick Henke, Thilo Romba, Dr. Valeria Perseo, Dr. Felix Reimold and Dr. Håkan Smith.

I have made many friends in and outside of work during my PhD years, who I could always rely on for being a great company and having a fun time. This stable background helped me having a balanced life during these years, which I am grateful for. I would not be able to list every one of you, you all

know how forgetful I can be, so please forgive me for not listing all of your names here. But know that I am thinking of you. A special thanks goes to Neha, thanks for the coffee breaks and for everything else.

At last, my greatest gratitude goes to my family, thank you for the tremendous support you provided always, since I can remember. I am lucky to have you all. My family in Hungary, thank you for believing in me throughout the years and for accepting me for who I am. I'm never afraid because I know I have you. And my little family here in Greifswald. I would not have been able to do it without you. Timo, Maya, your hugs helped me through the hardest parts. I could not be happier with you two by my side.

# Statutory declaration

I hereby declare in accordance with the examination regulations that I myself have written this document, that no other sources as those indicated were used and all direct and indirect citations are properly designated, that the document handed in was neither fully nor partly subject to another examination procedure or published and that the content of the electronic exemplar is identical to the printing copy.

Greifswald, 24th October 2022

---

VANÓ



# List of Figures

1.1.	Outline of the Wendelstein 7-X stellarator. The plasma (pink) located in a vacuum vessel is confined by the non-planar coils (grey). The magnetic field is adjusted by the planar coils (orange) to for example modify the radial position of the plasma. The external superconducting coils are surrounded by the cryostat (grey). Source: [13] . . . . .	14
1.2.	The divertor plates (black) arranged in five bundles around the confined plasma (orange). The special carbon tiles of the divertor system are used to safely take up the heat and particle load coming from the plasma. Source: [18] . . . . .	15
1.3.	Magnetic flux surfaces of a standard configuration plasma. Outside of the confined region of closed magnetic surfaces, there are 5 magnetic island (with color) in the SOL region. The divertor is displayed with black lines. Source: [24] . . . . .	17
1.4.	Cross section for the main processes, charge exchange and ionisation, between a neutral beam atom and a thermal plasma ion, as well as effective cross section for ionisation of neutral beam atoms by electrons. All cross sections are shown as a function of the neutral beam energy. Source: [32] Fig. 5.3.1 . . . . .	19
1.5.	Radial diffusion (perpendicular to the magnetic field lines) as a function of collisionality ( $\nu_a^*$ ), with solid black line for a W7-X standard configuration example and dashed black line for a tokamak as a comparison. A number of transport regimes can be defined, indicated by dashed blue lines: trapped ( $\sqrt{\nu_a^*}$ and $\frac{1}{\nu_a^*}$ ), plateau and Pfirsch-Schütler regime. Source: [50] Fig. 4 . . . . .	25

1.6.	Relative intensity of the radiation of carbon in different ionisation stages according to the coronal equilibrium (dashed lines) and the local thermodynamic equilibrium, which is described by the Saha equation (solid lines). Source: [61] Fig. 2, rescaled x-axis . . . . .	30
2.1.	Schematic structure of a typical Czerny-Turner spectrometer. The spectrometer used for measuring the line-integrated radiation coming from the plasma is arranged according to this setup. . . . .	34
2.2.	All lines of sight of the Passive Spectroscopy system shown for standard equilibrium flux surfaces as a function of the radial (major radius, $R$ ) and vertical ( $Z$ ) coordinates. The numbers are given from the full set of 80 channels available. . . . .	36
2.3.	Example image of radiation from the plasma as detected by the CCD camera. The horizontal axis is the wavelength, the vertical axis represents the different channels. The colour scale shows the photon count of a given channel at a given wavelength. One channel was used as a calibration channel, and thus it does not detect any light from the plasma. . . . .	37
2.4.	Example spectrum of one channel with the $C^{5+}$ line as measured by the CCD camera. It can be seen that the baseline of the spectrum is changing gradually throughout the detected wavelength range. The background can be approximated as a constant in the vicinity of the spectral line of interest. . . . .	38
2.5.	Measured $C^{5+}$ spectral line in black with the fitted Gaussian and its baseline in orange. The no-plasma background is also displayed in black with a fitted constant in orange. The difference between the no-plasma background level and the baseline of the Gaussian is the bremsstrahlung level. The intensity derived from the spectrum is the area under the Gaussian, displayed as the enclosed orange area. . . . .	39
2.6.	Arrays of $\rho$ representing the flux surfaces each LOS is looking through and thus, detecting radiation from. They are shown as a function of major radius ( $R$ ). The colour of curves of each LOS corresponds to the colours shown in Figure 2.2. . . . .	42

2.7. Electron temperature measured by the Thomson Scattering diagnostic at $t = 3$ s during discharge 20171207.006. . . . .	44
2.8. Time evolution of plasma parameters during discharge 20171207.006. ECRH power is shown in green and diamagnetic energy shown in black (a). Line integrated electron density measured by the Interferometer shown in dark red and core electron temperature measured by the Thomson Scattering diagnostic in blue (b). . . . .	47
2.9. Time evolution of the measured line integrated intensity during discharge 20171207.006. The coloured curves refer to the LOSs shown in Figure 2.2. The black curve is the line integrated density from the interferometer The time range of interest is $2.6 \text{ s} < t < 3.5 \text{ s}$ when the plasma was in a stable phase. . . . .	48
2.10. Measured line integrated intensity curve as a function of channels at $t = 2.14$ s in black with the fitted intensities from the inversion process in red. The light and dark green curves are the intensities derived from the two Gaussian of the emissivity separately, representing the electron excitation and the thermal neutral contributions. It seems to be clear that the two bump-like structure in the detected line integrated intensity curve can be traced back to the two sources individually. . . . .	49
2.11. Fitted profile of the $C^{5+}$ emission intensity as a function of $\rho$ at $t = 2.7$ s of discharge 20171207.006. The light and dark green curves are the two Gaussian that summed up construct the full emission intensity in dark red. . . . .	50
2.12. Time evolution of the middle position (a), intensity (b) and FWHM (c) of the electron excitation and charge exchange peak as a result of the inversion. . . . .	51
2.13. $C^{5+}$ emissivity with electron impact excitation and charge exchange as sources, calculated by the STRAHL impurity transport code for typical ECRH plasma parameters at W7-X. The emissivity was calculated assuming transport dominated by neoclassical effects (a) and assuming high anomalous diffusion (b). Source: [69] . . . . .	53

2.14.	Thermal neutral density estimated from the ratio of electron excitation and charge exchange peak in the emission intensity.	55
2.15.	Neutral pressure calculated from the estimated neutral density. The pressure level is marginally lower than that measured by the Neutral Pressure Gauges in front of the divertor, as expected. . . . .	56
3.1.	The LOSs of the three viewing ports of the CXRS system, <i>AEA21</i> (toroidal, blue), <i>AEM21</i> (partially poloidal, green and grey) and <i>AET21</i> (yellow), in relation to the two operating neutral beams, <i>S7</i> (pink) and <i>S8</i> (red). The carbon divertor and wall tiles are displayed in the background. Source: [74] Fig. 1. (a) . . . . .	61
3.2.	Intersection points of each LOS of the CXRS system with the neutral beams displayed over standard equilibrium flux surfaces shown in relation to the two neutral beams, <i>S7</i> and <i>S8</i> . A red cross indicates the magnetic axis in the centre of the cross section. Source: [74] Fig. 2. . . . .	62
3.3.	Schematic structure of the <i>ILS</i> showing how the light rays are directed and then filtered within the spectrometer. The green, red and blue light rays refer to radiation from the wavelength range around the $C^{5+}$ line at 529.06 nm, the $H^{\alpha}$ line at 656.028 nm and the $He^{+}$ line at 468.58 nm, respectively. Source: [76] Fig. 1. . . . .	65
3.4.	Spectrum measured by the <i>ILS</i> $C^{5+}$ camera in black with the no-plasma background level displayed below it. The difference is the bremsstrahlung level. Both underlying backgrounds are subtracted before further processing. . . . .	66
3.5.	Separation of the active (red) and passive (blue) component of an example measured $C^{5+}$ spectra (black dots). Both components are fitted with a Gaussian, with their addition (green, upper plot) matching the measurement. The lower plot (green) shows the difference of the measured data (points and error bars, top plot). Source: [74] Fig. 7. (a) . . . . .	67

3.6. Time trace of the fitted active (solid red) and passive (solid blue) component in relation to the linear interpolation of the passive component between the measured passive frames before and after the NBI operation (dashed blue). Source: [74] Fig. 7. (b) . . . . .	69
3.7. Example measured $H_\alpha$ spectrum (black dots) and its fitted components during NBI operation: cold $H_\alpha$ (brown); 1st (red), 2nd (green) and 3rd (blue) energy components; halo (yellow); and nearby impurity lines (pink). The result of adding up the fits of all components (blue line) matches the measured spectrum sufficiently. Additionally, the $H_\alpha$ spectrum measured when the NBI is turned off is displayed in grey. Source: [74] Fig. 10. (a) . . . . .	70
3.8. Dependencies of the charge exchange emission coefficient ( $Q_{CX}$ ) in relevant plasma parameter ranges based on data from the OPEN-ADAS database [82]. $Q_{CX}$ is shown as a function of the neutral beam energy (upper left), $Z_{eff}$ (upper right), ion density (lower left) and ion temperature (lower right). . . . .	72
3.9. Examples for the relation between an NBI blip (green) and the radiation detection by the spectrometer cameras (red) as a function of time. . . . .	80
3.10. Comparison of carbon density profiles from an example time point of discharge 20181009.034. The density was calculated with the cross calibration method described in Section 3.1.3 (green dashed line) and with the use of absolute intensity calibration and modelled beam densities (red dots). . . . .	82
3.11. Neoclassical diffusion (green) and the sum of the neoclassical and anomalous diffusion (purple) for the ECRH dominated time range of discharge 20181009.034. The anomalous diffusion is derived from time dependent analysis of impurities injected by Laser Blow-Off [89] [56] and was scaled with the ECRH power used, in accordance with the scaling found in that study. . . . .	86

3.12. Density profile of all ionisation stages of carbon in a standard ECRH dominated plasma. $\rho = 1$ marks the LCFS. The carbon is fully ionised for most of the confined plasma and the profile of this ionisation stage is flat throughout the plasma radius. . . . .	87
3.13. Global parameters of discharge 20180920.009. Time evolution of the ECRH power (blue) and NBI heating power (green) (a). Time trace of the core electron density ( $n_e$ , orange) and core electron temperature ( $T_e$ , dark blue) measured by the Thomson Scattering diagnostic (b). . . . .	88
3.14. Average carbon density profile of discharges 20180920.009, 013, 017, 033. These otherwise identical discharges had electron densities of $4, 6, 8, 9 * 10^{19} \text{ m}^{-3}$ . This allows the investigation of the dependence of the carbon content on the plasma density. . .	89
3.15. Average core carbon density of discharges 20180920.009, 013, 017, 033 as a function of the corresponding background electron densities. With higher the electron density, lower the carbon density levels are observed. . . . .	90
3.16. Global parameters of discharge 20180927.042. Overview on the heating methods (a) with the time trace of the ECRH power (blue) and NBI heating power (green). Time evolution of the core electron density ( $n_e$ , orange) and core electron temperature ( $T_e$ , dark blue) measured by the Thomson Scattering diagnostic (b). . . . .	91
3.17. Average carbon density level of each NBI blip in discharge 20180927.042 as a function of ECRH power. The two quantities are proportional, the carbon density is increased with higher ECRH power. . . . .	93

<p>3.18. Global parameters of discharge 20181009.034. Time trace of the ECRH power (blue) and the NBI heating power (green) (a). Time trace of the core electron temperature (light blue) and the core ion temperature (dark blue) (b). Time trace of the core electron density (orange, solid line), the electron density outside of half radius (orange, dashed line) and the core carbon density (red) (c). The chosen example time points are displayed as vertical dashed lines on all three figures in colours that match the colour of the example carbon density profiles in Figure 3.20. . . . .</p>	95
<p>3.19. Example electron density profiles at the times highlighted in Figure 3.18. The <math>n_e</math> profile is marginally peaked during the only ECRH phase as seen also in other ECRH dominated plasmas. It starts peaking in the core more and more as the plasma is heated by only NBI. . . . .</p>	97
<p>3.20. Carbon density profiles from the selected time points. The colour of the profiles match the time points highlighted in Figure 3.18. The profile is flat during the only ECRH heated phase (<math>t &lt; 1</math> s), then becomes more and more peaked as the plasma is heated by solely NBI (<math>1 \text{ s} &lt; t &lt; 3 \text{ s}</math>). . . . .</p>	99
<p>3.21. Diffusion (a) and convection velocity (b) profiles used in the pySTRAHL simulation of the ECRH phase of discharge 20181009.034. The diffusion profile is dominated by the anomalous component that is obtained from [89] and scaled according to the given ECRH power level. The used convection velocity is assumed to be completely neoclassical. . . . .</p>	101
<p>3.22. Neoclassical diffusion (a) and convection velocity (b) profiles calculated by Neotransp for the given background plasma conditions at <math>t = 2.5</math> s of discharge 20181009.034, as an example time point from the NBI phase (green). The diffusion and convection velocity profiles used in the ECRH phase ((as shown in Figure 3.21)) are also displayed for comparison (purple). . . . .</p>	102

3.23. Simulated carbon density profiles assuming neoclassical transport only (a) and experimentally obtained carbon density profiles (b) from the example time points during the NBI phase of discharge 20181009.034. The peaking behaviour agrees for  $\rho < 0.5$ . However, the neoclassical profiles decrease for  $\rho > 0.5$  during NBI operation, creating a small valley, which is not consistent with the experimental profiles. 104

3.24. Time evolution of the simulated carbon density with purely neoclassical transport (a) and of the experimentally obtained carbon density (b) during the investigated phase of discharge 20181009.034. The simulated constant time trace during the ECRH phase is also displayed. The time evolution of the simulated and experimental profiles is displayed for three radial regions:  $\rho < 0.2$ ,  $0.4 < \rho < 0.6$  and  $0.7 < \rho < 0.8$ . The neoclassical density decreases outside of half radius, while the neoclassical and experimental core densities increase to a similar level, although with different growth rate throughout the investigated time range. . . . . 105

3.25. Anomalous diffusion (a) and neoclassical convection velocity (b) as used in the simulation of the NBI phase assuming two different transport regions (green). The diffusion is kept at neoclassical levels at  $\rho < 0.5$ , as in the fully neoclassical simulation, and has a strong anomalous component at  $\rho > 0.5$ . The anomalous diffusion and neoclassical convection velocity profiles used in the ECRH phase (as shown in Figure 3.21) are displayed for comparison (purple). . . . . 106

3.26. Simulated carbon density profiles with neoclassical diffusion at  $\rho < 0.5$ , and anomalous diffusion at  $\rho > 0.5$  (a) from the example time points of discharge 20181009.034 with the experimental profiles from the same time points for comparison (b). There is no valley appearing outside of half radius, while the peaking in the core is still observable, which agrees with the experimental profiles better than the purely neoclassical simulation. . . . . 107

3.27. Time evolution of the simulated carbon density with neoclassical diffusion at  $\rho < 0.5$ , and anomalous diffusion at  $\rho > 0.5$  (a) of the investigated phase of discharge 20181009.034 with the experimental time evolution displayed for comparison. Three radial regions are shown:  $\rho < 0.2$ ,  $0.4 < \rho < 0.6$  and  $0.7 < \rho < 0.8$ . The growth rate and the shape of the time trace for the simulated and experimental carbon densities does not fully agree in the core, the simulated density rises higher within the given time range. The time traces agree well for the other radial regions. . . . . 108

3.28. Core carbon density time evolution with different core anomalous diffusion level (a). Carbon density gradient as a function of the scaling factor for the core anomalous diffusion (b), showing no significant peaking with high core anomalous diffusion. . . . . 110

3.29. Global parameters of discharge 20181009.034 with an example time point highlighted in the last, NBI dominated phase with low level ECRH. Time trace of the ECRH power in blue and the NBI heating power in green (a). Time trace of the core electron temperature in light blue and the core ion temperature in dark blue (b). Time trace of the core electron density in orange with solid line, the electron density outside of half radius in orange with dashed line and the core carbon density obtained from the CXRS signal in red (c). . . . . 111

3.30. Carbon density profiles from the selected time points of discharge 20181009.034. The colour of the profiles match the time points highlighted in Figure 3.29 with the time point in the mixed heated plasma phase highlighted. . . . . 113

3.31.	Time evolution of relevant parameters for discharge 20181016.037. Time trace of the ECRH power (blue) and NBI heating power (green) (a). Time trace of the electron density (b) and the $C^{6+}$ concentration (c). The latter two quantities are displayed for the plasma core ( $\rho < 0.2$ ) with solid orange and dark red lines and for the plasma edge ( $\rho > 0.8$ ) with dashed orange and dark red lines, respectively. The two continuous pellet injection phases are indicated with grey areas in the figures. The high performance phase takes place around $t = 1.7$ s. . . . .	116
3.32.	$C^{6+}$ concentration profiles of discharge 20181016.037 for selected example time points. The first time point is taken at the end of the first pellet phase, before the high performance phase. The rest of the time points are taken every 0.2 s of the the high performance phase where the core concentration increases, until the time point with the highest core concentration. . . . .	118

# List of Tables

2.1.	Parameters of the Czerny Turner mirror spectrometer that were used for the Passive Spectroscopy system during OP1.2a.	35
3.1.	Parameters of the ITER-like Spectrometer ( <i>ILS</i> ) spectrometer as were used for the Active Spectroscopy system during OP1.2b. [76] [77] . . . . .	64
3.2.	Dimension of the theoretical and measured intensity of the $C^{5+}$ ion ( $I^{CX}$ and $I_m^{CX}$ ) and the beam energy components ( $I_E^{BES}$ and $I_{E,m}^{BES}$ ), as well as the dimension of the bremsstrahlung background, theoretical and measured by the $C^{5+}$ camera ( $B^{CX}$ and $B_m^{CX}$ ) and the $H_\alpha$ camera ( $B^{BES}$ and $B_m^{BES}$ ). The dimension of the dispersion of the two cameras ( $\omega^{CX}$ and $\omega^{BES}$ ) is also displayed. $\gamma$ refers to the number of photons emitted, while $e^-$ refers to the photoelectron count recorded by the cameras. $t_{frame}^{CX}$ and $t_{frame}^{BES}$ refer to the time length of one frame of the respective cameras. . . . .	78
3.3.	Plasma parameters of discharge 20181016.037 at $t = 1.75$ s, when the high performance phase took place. $P_{heating}$ refers to the ECRH power, $W_{dia}$ , $T_i$ and $n_e$ are measured by the magnetic diagnostic system [5], the XICS diagnostic and the Thomson Scattering diagnostic, respectively. $C_C$ refers to the concentration of $C^{6+}$ ions measured by the <i>ILS</i> spectrometer of the CXRS diagnostic. . . . .	120



# Bibliography

- [1] J. WESSON. *Tokamaks*. In: Oxford Science Publications, 1997. Chapter 1.4 Fusion - Power balance, 1.5 Fusion - Ignition, pages 8–15.
- [2] J. D. LAWSON. »Some criteria for a useful thermonuclear reactor«. In: *Atomic Energy Research Establishment*, (1955).
- [3] J. D. LAWSON. »Some Criteria for a Power Producing Thermonuclear Reactor«. In: *Proc. Phys. Soc. Section B*, Vol. 70.6 (1957).
- [4] L. M. KOVRIZHNYKH. »The energy confinement time in stellarators«. In: *Nucl. Fusion*, Vol. 24.435 (1984).
- [5] K. RAHBARNIA. »Diamagnetic energy measurement during the first operational phase at the Wendelstein 7-X stellarator«. In: *Nucl. Fusion*, Vol. 58.096010 (2018). DOI: 10.1088/1741-4326/aacab0.
- [6] S. SUDO. »Scalings of energy confinement and density limit in stellarator/heliotron devices«. In: *Nucl. Fusion*, Vol. 30.11 (1990).
- [7] U. STROTH. »Stellarator-tokamak energy confinement comparison based on ASDEX Upgrade and Wendelstein 7-X hydrogen plasmas«. In: *Nucl. Fusion*, Vol. 61.016003 (2021). DOI: 10.1088/1741-4326/abbc4a.
- [8] H. J. DE BLANK. »Guiding Center Motion«. In: *Fusion Science and Technology*, Vol. 45:2T.47 (2004). DOI: 10.13182/FST04-A468.
- [9] L. ARTSIMOVICH. »Tokamak devices«. In: *Nucl. Fusion*, Vol. 12.215 (1972).
- [10] L. SPITZER. »The Stellarator Concept«. In: *The Physics of Fluids*, Vol. 1.253 (1958). DOI: 10.1063/1.1705883.
- [11] M. WANNER. »Design goals and status of the WENDELSTEIN 7-X project«. In: *Plasma Phys. Control. Fusion*, Vol. 42.1179 (2000). DOI: S0741-3335(00)13080-5.

- [12] J. NÜHRENBERG. »Overview on Wendelstein 7-X Theory«. In: *Fusion Technology*, Vol. 27.71 (1995). DOI: 10.13182/FST95-A11947048.
- [13] »IPP Internal Image Repository«. URL: <https://svcumulus.ipp.mpg.de/>.
- [14] V. ERCKMANN. »The W7-X Project: Scientific Basis and Technical Realization«. In: *17th IEEE/NPSS Symposium Fusion Engineering*. Vol. 1. 40. 1997.
- [15] A. DINKLAGE. »Magnetic configuration effects on the Wendelstein 7-X stellarator«. In: *Nature Physics*, Vol. 14.855 (2018). DOI: 10.1038/s41567-018-0141-9.
- [16] M. DREVLAK. »Fast particle confinement with optimized coil currents in the W7-X stellarator«. In: *Nucl. Fusio*, Vol. 54.073002 (2014). DOI: 10.1088/0029-5515/54/7/073002.
- [17] R. KÖNIG. »The divertor program in stellarators«. In: *Plasma Phys. Control. Fusion*, Vol. 44.2365 (2002). DOI: 10.1088/0741-3335/44/11/306.
- [18] V. PERSEO. »Provided from private communication«. 2021.
- [19] R. C. WOLF. »Major results from the first plasma campaign of the Wendelstein 7-X stellarator«. In: *Nucl. Fusion*, Vol. 57.102020 (2017). DOI: 10.1088/1741-4326/aa770d.
- [20] T. KLINGER. »Overview of first Wendelstein 7-X highperformance operation«. In: *Nucl. Fusion*, Vol. 59.112004 (2019). DOI: 10.1088/1741-4326/ab03a7.
- [21] T. ANDREEVA. *Vacuum magnetic configurations of Wendelstein 7-X*. Technical report IPP III/270. Max-Planck-Institut für Plasmaphysik, 2002.
- [22] J. GEIGER. »Physics in the magnetic configuration space of W7-X«. In: *Plasma Phys. Control. Fusion*, Vol. 57.014004 (2015). DOI: 10.1088/0741-3335/57/1/014004.
- [23] Y. FENG. »Comparison between stellarator and tokamak divertor transport«. In: *Plasma Phys. Control. Fusion*, Vol. 53.024009 (2011). DOI: 10.1088/0741-3335/53/2/024009.

- 
- [24] C. KILLER. »Provided from private communication«. 2021.
- [25] S. P. HIRSCHMAN. »Three-dimensional free boundary calculations using a spectral Green's function method«. In: *Comput. Phys. Commun.*, Vol. 43.143 (1986). DOI: 10.1016/0010-4655(86)90058-5.
- [26] V. ERCKMANN. »Electron Cyclotron Heating for W7-X: Physics and Technology«. In: *Fusion Science and Technology*, Vol. 52.2 (2017), page 291. DOI: 10.13182/FST07-A1508.
- [27] T. STANGE. »Advanced electron cyclotron heating and current drive experiments on the stellarator Wendelstein 7-X«. In: *EPJ Web of Conferences*, Vol. 157.02008 (2017). DOI: 10.1051/epjconf/201715702008.
- [28] P. MCNEELY. »Commissioning and initial operation of the W7-X neutral beam injection heating system«. In: *Fusion Eng. Des.*, Vol. 161.111997 (2020). DOI: 10.1016/j.fusengdes.2020.111997.
- [29] S. A. LAZERSON. »First neutral beam experiments on Wendelstein 7-X«. In: *Nucl. Fusion*, Vol. 61.096008 (2021). DOI: 10.1088/1741-4326/ac121c.
- [30] H. LAQUA. »High-performance ECRH at W7-X: experience and perspectives«. In: *Nucl. Fusion*, Vol. 61.106005 (2021). DOI: 10.1088/1741-4326/ac1a1b.
- [31] R. C. WOLF. »Electron-cyclotron-resonance heating in Wendelstein 7-X: A versatile heating and current-drive method and a tool for in-depth physics studies«. In: *Plasma Phys. Control. Fusion*, Vol. 61.014037 (2019). DOI: 10.1088/1361-6587/aaeab2.
- [32] J. WESSON. *Tokamaks*. In: Oxford Science Publications, 1997. Chapter 5.3 Heating - Neutral beam injection, pages 243–246.
- [33] I. V. HERTEL. *Atoms, Molecules and Optical Physics 2*. Springer, 2015. DOI: 10.1007/978-3-642-54313-5.
- [34] S. A. LAZERSON. »Validation of the BEAMS3D neutral beam deposition model on Wendelstein 7-X«. In: *Nucl. Fusion*, Vol. 60.076020 (2020). DOI: 10.1088/1741-4326/ab8e61.

- [35] E. SPETH. »Rf ion sources for fusion applications: design, development and performance«. In: *Fusion Eng. Des.*, Vol. 46.383 (1999). DOI: 10.1016/S0920-3796(99)00030-7.
- [36] A. SPANIER. »Performance of the first neutral beam injector at the Wendelstein 7-X stellarator«. In: *Fusion Eng. Des.*, Vol. 163.112115 (2021). DOI: 10.1016/j.fusengdes.2020.112115.
- [37] E. PASCH. »Dual-laser wavelength Thomson scattering at Wendelstein 7-X«. In: *Rev. Sci. Instrum.*, Vol. 89.10C115 (2018). DOI: 10.1063/1.5038422.
- [38] K. J. BRUNNER. »Real-time dispersion interferometry for density feedback in fusion devices«. In: *J. Instrum.*, Vol. 13.P09002 (2018). DOI: 10.1088/1748-0221/13/09/P09002.
- [39] J. BALDZUHN. »Pellet fueling experiments in Wendelstein 7-X«. In: *Plasma Phys. Control. Fusion*, Vol. 61.095012 (2019). DOI: 10.1088/1361-6587/ab3567.
- [40] J. BALDZUHN. »Enhanced energy confinement after series of pellets in Wendelstein 7-X«. In: *Plasma Phys. Control. Fusion*, Vol. 62.055012 (2020). DOI: 10.1088/1361-6587/ab8112.
- [41] U. WENZEL. »Performance of new crystal cathode pressure gauges for long-pulse operation in the Wendelstein 7-X stellarator«. In: *Rev. Sci. Instrum.*, Vol. 90.123507 (2019). DOI: 10.1063/1.5121203.
- [42] J. BALDZUHN. »Measurement and calculation of the radial electric field in the stellarator W7-AS«. In: *Plasma Phys. Control. Fusion*, Vol. 40.967 (1998). DOI: 10.1088/0741-3335/40/6/006.
- [43] J. M. GARCÍA-REGAÑA. »On-surface potential and radial electric field variations in electron root stellarator plasmas«. In: *Plasma Phys. Control. Fusion*, Vol. 60.104002 (2018). DOI: 10.1088/1361-6587/aad795.
- [44] A. LANGENBERG. »Forward Modeling of X-Ray Imaging Crystal Spectrometers Within the Minerva Bayesian Analysis Framework«. In: *Fusion Sci. Technol.*, Vol. 69.560 (2016). DOI: 10.13182/FST15-181.

- 
- [45] A. LANGENBERG. »Prospects of X-ray imaging spectrometers for impurity transport: Recent results from the stellarator Wendelstein 7-X«. In: *Rev. Sci. Instrum.*, Vol. 89.10G101 (2018). DOI: 10.1063/1.5036536.
- [46] F. F. CHEN. *Introduction to plasma physics and controlled fusion*. In: Second. Volume 1: Plasma Physics. Plenum Press, 1984. Chapter 5. Diffusion and resistivity.
- [47] R. DUX. »Impurity Transport in Tokamak Plasmas«. Habilitation Thesis. 2004.
- [48] P. HELANDER. »Impurity Transport in a Mixed-Collisionality Stellarator Plasma«. In: *Physical Review Letters*, Vol. 118.155002 (2017). DOI: 10.1103/PhysRevLett.118.155002.
- [49] P. I. STRAND. »Magnetic flux evolution in highly shaped plasmas«. In: *Physics of Plasmas*, Vol. 8.2782 (2001). DOI: 10.1063/1.1366618.
- [50] P. HELANDER. »Stellarator and tokamak plasmas: a comparison«. In: *Plasma Phys. Control. Fusion*, Vol. 54.124009 (2012). DOI: 10.1088/0741-3335/54/12/124009.
- [51] P. HELANDER. »Theory of plasma confinement in non-axisymmetric magnetic fields«. In: *Rep. Prog. Phys.*, Vol. 77.087001 (2014). DOI: 10.1088/0034-4885/77/8/087001.
- [52] Y. TURKIN. »Neoclassical transport simulations for stellarators«. In: *Phys. Plasmas*, Vol. 18.022505 (2011).
- [53] C. D. BEIDLER. »Benchmarking of the mono-energetic transport coefficients—results from the International Collaboration on Neoclassical Transport in Stellarators (ICNTS)«. In: *Nucl. Fusion*, Vol. 51.076001 (2011). DOI: 10.1088/0029-5515/51/7/076001.
- [54] M. N. A. BEURSKENS. »Ion temperature clamping in Wendelstein 7-X electron cyclotron heated plasmas«. In: *Nucl. Fusion*, Vol. 61.116072 (2021). DOI: 10.1088/1741-4326/ac1653.
- [55] G. MEZEY. »Wall erosion in fusion devices«. In: *Plasma Phys. Control. Fusion*, Vol. 28.147 (1986).

- [56] T. WEGNER. »Design, capabilities, and first results of the new laser blow-off system on Wendelstein 7-X«. In: *Rev. Sci. Instrum.*, Vol. 89.073505 (2018). DOI: 10.1063/1.5037543.
- [57] R. BUSSIAHN. »Tracer-Encapsulated Solid Pellet (TESPEL) injection system for Wendelstein 7-X«. In: *Rev. Sci. Instrum.*, Vol. 89.10K112 (2018). DOI: 10.1063/1.5038844.
- [58] M. G. VON HELLERMANN. »Complex Spectra in Fusion Plasmas«. In: *Phys. Scr.*, Vol. T120 (2005), page 19. DOI: 10.1088/0031-8949/2005/t120/003.
- [59] J. COOPER. »Plasma spectroscopy«. In: *Rep. Prog. Phys.*, Vol. 29.35 (1966). DOI: 10.1088/0034-4885/29/1/302.
- [60] R. S. S. M. A. DOPITA. *Astrophysics of the Diffuse Universe*. In: edited by ASTRONOMY and A. LIBRARY. Springer, Berlin, Heidelberg, 2003. Chapter 5. Collisional Ionization Equilibrium, pages 101–123. DOI: 10.1007/978-3-662-05866-4\_5.
- [61] R. J. E. JASPERS. »Plasma Spectroscopy«. In: *Fusion Science and Technology*, Vol. 57-2T.421 (2010). DOI: 10.13182/FST10-A9433.
- [62] R. BURHENN. »On impurity handling in high performance stellarator/heliotron plasmas«. In: *Nucl. Fusion*, Vol. 49.065005 (2009). DOI: 10.1088/0029-5515/49/6/065005.
- [63] R. BURHENN. »Impurity Transport Studies in the Wendelstein 7-AS Stellarator«. In: *Fusion Sci. Technol.*, Vol. 46.1 (2004), page 115. DOI: 10.13182/FST04-A547.
- [64] C. SWEE. »Impurity Transport Studies at the HSX Stellarator Using Active and Passive CVI Spectroscopy«. In: *Plasma Phys. Control. Fusion*, (2021). Submitted.
- [65] R. DUX. *STRAHL User Manual*. Max-Planck-Institute für Plasmaphysik. 2014.
- [66] E. VIEZZER. »Investigation of passive edge emission in charge exchange spectra at the ASDEX Upgrade tokamak«. In: *Plasma Phys. Control. Fusion*, Vol. 53.035002 (2011). DOI: 10.1088/0741-3335/53/3/035002.

- 
- [67] T. S. PEDERSEN. »First results from divertor operation in Wendelstein 7-X«. In: *Plasma Phys. Control. Fusion*, Vol. 61.014035 (2019). DOI: 10.1088/1361-6587/aaec25.
- [68] A. ZOCCO. »W7-X and the sawtooth instability: towards realistic simulations of current-driven magnetic reconnection«. In: *Nucl. Fusion*, Vol. 61.086001 (2021). DOI: 10.1088/1741-4326/ac077d.
- [69] B. GEIGER. »Provided from private communication«. 2018.
- [70] »OPEN-ADAS, Atomic Data and Analysis Structure, ADF15 Photon emissivity coefficients«. <https://open.adas.ac.uk/adf15>.
- [71] J. BALDZUHN. *Description of the CX<sub>g</sub>imulroutine*. 1-QSC-T0015.0. Max-Planck-Institut für Plasmaphysik. 2012.
- [72] R. C. ISLER. »An overview of charge-exchange recombination spectroscopy as a plasma diagnostic«. In: *Plasma Phys. Control. Fusion*, Vol. 36.171 (1994). DOI: 10.2172/6209892.
- [73] M. G. VON HELLERMANN. »Active Beam Spectroscopy«. In: *AIP Conference Proceedings*, Vol. 988.165 (2008). DOI: 10.1063/1.2905060.
- [74] O. P. FORD. »Charge exchange recombination spectroscopy at Wendelstein 7-X«. In: *Rev. Sci. Instrum.*, Vol. 91.023507 (2020). DOI: 10.1063/1.5132936.
- [75] J. A. ALONSO. »Plasma flow in the Wendelstein 7-X stellarator: first measurements compared to neoclassical calculations«. In: (2022). Ready for submission.
- [76] R. J. E. JASPERS. »A high etendue spectrometer suitable for core charge eXchange recombination spectroscopy on ITER«. In: *Rev. Sci. Instrum.*, Vol. 83.10D515 (2012). DOI: 10.1063/1.4732058.
- [77] A. KAPPATOU. *Investigations of helium transport in ASDEX Upgrade plasmas with charge wxchange recombination spectroscopy*. PhD thesis. Eindhoven University of Technology, 2014.
- [78] R. M. MCDERMOTT. »Extensions to the charge exchange recombination spectroscopy diagnostic suite at ASDEX Upgrade«. In: *Rev. Sci. Instrum.*, Vol. 88.073508 (2017). DOI: 10.1063/1.4993131.

- [79] R. M. MCDERMOTT. »Evaluation of impurity densities from charge exchange recombination spectroscopy measurements at ASDEX Upgrade«. In: *Plasma Phys. Control. Fusion*, Vol. 60.095007 (2018). DOI: 10.1088/1361-6587/aad256.
- [80] A. KAPPATOU. »Method to obtain absolute impurity density profiles combining charge exchange and beam emission spectroscopy without absolute intensity calibration«. In: *Rev. Sci. Instrum.*, Vol. 83.10D519 (2012). DOI: 10.1063/1.4732847.
- [81] R. DUX. »Impurity density determination using charge exchange and beam emission spectroscopy at ASDEX Upgrade«. In: *EPS Conference on Plasma Physics*. 2011.
- [82] »OPEN-ADAS, Atomic Data and Analysis Structure, ADF12 Charge exchange effective emission coefficients«. <https://open.adas.ac.uk/adf12>.
- [83] »OPEN-ADAS, Atomic Data and Analysis Structure, ADF22 Effective beam emission/population coefficients«. <https://open.adas.ac.uk/adf22>.
- [84] T. ROMBA. *Validation of the W7-X CXRS for impurity density profiles*. Master's thesis. Eindhoven University of Technology, 2021.
- [85] P. Z. POLOSKEI. »Experimental characterization of the active and passive fast-ion H-alpha emission in W7-X using FIDASIM«. In: *Nuclear Fusion*, (2021). Submitted.
- [86] S. KWAK. »Bayesian inference of spatially resolved Zeff profiles from line integrated bremsstrahlung spectra«. In: *Rev. Sci. Instrum.*, Vol. 92.043505 (2021). DOI: 10.1063/5.0043777.
- [87] W. W. HEIDBRINK. »A Code that Simulates Fast-Ion D and Neutral Particle Measurements«. In: *Commun. Comput. Phys.*, Vol. 10.3 (2011), page 716. DOI: 10.4208/cicp.190810.080211a.
- [88] B. GEIGER. »Progress in modelling fast-ion D-alpha spectra and neutral particle analyzer fluxes using FIDASIM«. In: *Plasma Phys. Control. Fusion*, Vol. 62.105008 (2020). DOI: 10.1088/1361-6587/aba8d7.
- [89] B. GEIGER. »Observation of anomalous impurity transport during low-density experiments in W7-X with laser blow-off injections of iron«. In: *Nucl. Fusion*, Vol. 59.046009 (2019). DOI: 10.1088/1741-4326/aaff71.

- 
- [90] D. CARRALERO. »An experimental characterization of core turbulence regimes in Wendelstein 7-X«. In: *Nucl. Fusion*, Vol. 61.096015 (2021). DOI: 10.1088/1741-4326/ac112f.
- [91] J.-P. BÄHNER. »Phase contrast imaging measurements and numerical simulations of turbulent density fluctuations in gas-fuelled ECRH discharges in Wendelstein 7-X«. In: *J. Plasma Phys.*, Vol. 87.905870314 (2021). DOI: 10.1017/S0022377821000635.
- [92] P. HELANDER. »Quasilinear particle transport from gyrokinetic instabilities in general magnetic geometry«. In: *Plasma Physics and Controlled Fusion*, Vol. 60.084006 (2018). DOI: 10.1088/1361-6587/aac8b7.
- [93] S. P. HIRSCHMAN. »Plasma transport coefficients for nonsymmetric toroidal confinement systems«. In: *Phys. Fluids*, Vol. 29.2951 (1986). DOI: 10.1063/1.865495.
- [94] W. I. VAN RIJ. »Variational bounds for transport coefficients in three-dimensional toroidal plasmas«. In: *Phys. Fluids B*, Vol. 1.563 (1989). DOI: 10.1063/1.859116.
- [95] V. R. WINTERS. *Carbon Sourcing and Transport in the Island Divertor of Wendelstein 7-X*. PhD thesis. University of Wisconsin-Madison, 2019.
- [96] R. M. MCDERMOTT. »Provided from private communication«. 2021.
- [97] D. GRADIC. »Assessment of the plasma start-up in Wendelstein 7-X with neutral beam injection«. In: *Nucl. Fusion*, Vol. 55.033002 (2015). DOI: 10.1088/0029-5515/55/3/033002.
- [98] O. P. FORD. »Turbulence reduced high performance scenarios in Wendelstein 7-X, on the path to a steady state reactor«. In: *EPS Conference on Plasma Physics*. 2020.
- [99] B. LABOMBARD. *KN1D: A 1-D Sapce, 2-D Velocity, Kinetic Transport Algorithm For Atomic and Molecular Hydrogen in an Ionizing Plasma*. Technical report PSFC/RR-01-3. Plasma Science and Fusion Center Massachusetts Institute of Technology, 2001.
- [100] V. WINTERS. »Provided from private communication«. 2021.

- [101] S. A. BOZHENKOV. »High-performance plasmas after pellet injections in Wendelstein 7-X«. In: *Nucl. Fusion*, Vol. 60.066011 (2020). DOI: 10.1088/1741-4326/ab7867.
- [102] A. KOMORI. »Goal and Achievements of Large Helical Device Project«. In: *Fusion Science and Technology*, Vol. 58.1 (2009). DOI: 10.13182/FST58-1.
- [103] P. XANTHOPOULOS. »Turbulence Mechanisms of Enhanced Performance Stellarator Plasmas«. In: *Phys. Rev. Lett.*, Vol. 125.075001 (2020). DOI: 10.1103/PhysRevLett.125.075001.
- [104] A. V. STECHOW. »Suppression of core turbulence by profile shaping in Wendelstein 7-X«. In: (2021). Under revision.
- [105] R. C. WOLF. »Performance of Wendelstein 7-X stellarator plasmas during the first divertor operation phase«. In: *Phys. Plasmas*, Vol. 26.082504 (2019). DOI: 10.1063/1.2098761.